Understanding the Chemistries of Ni-rich Layered Oxide Materials for Applications in Lithium Batteries and Catalysis

Crystal Keneé Waters

Dissertation submitted to the faculty of the Virginia Polytechnic Institute and State University in partial fulfillment of the requirements for the degree of

Doctor of Philosophy
In
Chemistry

Feng Lin (Chair)
John Morris
Joseph Merola
Hongliang Xin

September 20, 2021
Blacksburg, Virginia

Keywords: lithium batteries, electrochemistry, Ni-rich layered oxide cathodes, catalysis, surface chemistry, energy storage

Understanding the Chemistries of Ni-rich Layered Oxide Materials for Applications in Lithium Batteries and Catalysis

Crystal Keneé Waters

ABSTRACT

Ni-rich layered oxide materials have gained significant attention due to the ongoing advances and demands in energy storage. The energy revolution continues to catapult the need for improved battery materials, especially for applications in portable electronic devices and electric vehicles. Lithium batteries are at the frontier of energy storage. Due to geopolitical concerns, there is a growing need to understand the chemistries of Co-free, Ni-rich layered oxide materials which are cost-efficient and possess increased practical capacity. The challenge to studying this class of materials is their inherent electronic and structural fragility. The fragility of these materials is facilitated by a cooperation of metal cation migration, lattice oxygen loss, and undesirable oxide cathode-electrolyte interfacial reactions. Each of these phenomena contribute to complex electrolyte decomposition pathways and oxide cathode structural distortions. Structural instability leads to poor battery performance metrics including specific capacity fading and decreased Coulombic efficiency.

Electrolyte decomposition occurs at the oxide cathode surface, but it can lead to bulk electronic and structural changes, chemomechanical breakdown, and irreversible phase transformations in the material. The work in this dissertation focuses on understanding some of the chemistries associated with degradation of representative Ni-rich layered oxides, specifically $LiNiO_2$ (LNO) and $LiNi_xMn_yCo_zO_2$ (NMC) (where x+y+z =1) materials. ***Chapter 1*** provides a comprehensive review of the interfacial chemistries of fragile, Ni-rich layered oxide materials with carbonate-based liquid electrolytes. These reactions are key in deducing mechanistic pathways that promote thermal runaway. Uncontrollable oxygen loss and electrolyte oxidation leads to

catastrophic battery fires and explosions. The chapter highlights the material properties that become perturbed during high states-of-charge which complicate the materials chemistry associated with Ni-rich layered oxides. Lastly, a few strategies to mitigate undesired, structurally detrimental reactions at the Ni-rich layered oxide cathode surface are provided in ***Chapter 1***. To obtain the technical data detailed in this dissertation, a variety of analytical methods are employed. ***Chapter 2*** introduces the working principles of the X-ray techniques, electron microscopy, and other quantification methods. X-ray techniques including synchrotron X-ray absorption spectroscopy (XAS), and its components XANES and EXAFS are discussed. Other X-ray techniques, including X-ray diffraction (XRD) and X-ray photoelectron spectroscopy (XPS) are additionally included. Electron microscopy techniques, including transmission electron microscopy (TEM), scanning electron microscopy (SEM), and scanning transmission electron microscopy (STEM) are provided. Quantification methods, such as gas chromatography – flame ionization detection (GC-FID) and other electrochemical testing methods are also described. Detailed experimental information obtained using the analytical methods is provided in the technical chapters.

In understanding the chemistry of Ni-rich layered oxides, exploring surface reconstruction is key. Surface reconstruction, a phenomenon caused by a collaboration between Li/Ni cation intermixing and lattice oxygen loss, is one of the major explanations for structural degradation in Ni-rich layered oxide materials. ***Chapter 3*** explores surface reconstruction and deduces a mechanism by which lattice oxygen is loss in $LiNi_{0.6}Mn_{0.2}Co_{0.2}O_2$ (NMC622). By exploiting Li^+ intercalation chemistry, the work emulates various states-of-charge to explore how delithiation impacts small, organic molecule oxidation. Benzyl alcohol serves as a good probing molecule. It is similar to an oxidizable, nonaqueous electrolytic species that undergoes oxidation at the oxide

cathode surface. Structure-reactivity trends are defined to correlate electronic and structural changes, lattice oxygen loss, and small molecule oxidation.

After studying a proxy molecule, a practical system is required to grasp the complexity of the cathode-electrolyte interfacial reactions that promote Ni-rich layered oxide degradation. In ***Chapter 4***, an electrolyte stirring experiment is described. Stirring experiments provide an accelerated testing method which helps to deduce the influences of chemical electrolyte decomposition on structural degradation of $LiNiO_2$ (LNO). X-ray techniques are used to illustrate electronic perturbations and structural distortions in the material after probing with EC/DMC w/w 3:7 $LiPF_6$. Additionally, this dissertation chapter features a novel voltage oscillation experiment that is employed to quantify Ni-rich oxide cathode degradation at the phase transition regions. LNO has three charging plateaus – H1 → M, M → H2, and H2 → H3. The latter two plateaus have been largely associated with irreversible structural fragility in Ni-rich layered oxides. Cation intermixing and oxygen loss are two phenomena that are largely associated with decreased Li^+ intercalation kinetics and increased undesired side reactions. Although researchers debate the chemical phenomenon that occur at each of the phase transitions, most agree that the H2 → H3 transition is highly influenced by irreversible lattice oxygen loss. This dissertation chapter describes the studies used to explore the electronic changes and structural distortions that accompany the voltage oscillation electrochemical testing.

While Ni-rich layered oxides are largely employed as lithium battery cathodes, this class of material is unique in that it is a reducible and electronically tunable. Electronically modifiable metal oxide materials provide a unique platform to lend information to other applications, such as catalysis. There is much debate surrounding the role of metal oxides on metal nanocatalyst performance for catalytically reductive pathways. ***Chapter 5*** discusses the method of employing

$LiNiO_2$ and other NMC materials as electronically tunable metal oxides to determine the role of the reducible metal oxide support on the gold (Au) nanocatalyst for *p*-nitrophenol reduction to *p*-aminophenol. By obtaining a continuum of nickel (Ni) oxidation states using delithiation strategies, structural-activity relationship trends are provided. Conversion rates for each of the delithiated materials was calculated using pseudo first-order kinetics. Lastly, a detailed discussion on metal oxide reducibility and its influences on key mechanistic factors, such as the induction period is included.

Chapter 6 in this dissertation provides conclusions for the technical work provided. It bridges the works together and describes the overarching findings associated with the chemistries of Ni-rich layered oxide materials. This dissertation lays the foundation for future experimentation and innovation in understanding the surface chemistry of Ni-rich layered oxides. ***Chapter 7*** provides future perspectives for each of the technical works included herein. Additionally, the final chapter includes insights toward the future of lithium batteries and other cathode chemistries. As the world navigates the energy revolution, it is important to provide global perspectives expected to catapult a sustainable future with batteries towards a greener world.

Understanding the Chemistries of Ni-rich Layered Oxide Materials for Applications in Lithium Batteries and Catalysis

Crystal Keneé Waters

GENERAL AUDIENCE ABSTRACT

Rechargeable lithium batteries have gained a significant surge of interest due to the ongoing demands for portable electronic devices, as well as the global trend towards electric vehicles to decrease the carbon footprint. Lithium batteries reside at the pinnacle of the energy transition. Layered oxide materials are typically employed as the cathode in Li-ion batteries. Ni-rich layered oxides have gained much interest due to their low cost and good charge/discharge capabilities. As consumers want increased charging rates and longer lifetimes, researchers struggle to optimize the balance between incorporating Ni-rich cathodes and increased safety concerns caused by cathode structural fragility. The lack of structural robustness is largely due to the surface reactivity of Ni-rich layered oxide materials. Bonding arrangements and electron transfer pathways intrinsic to this class of material increases the complexity in understanding the surface chemistry and the associated degradation pathways.

Oxygen loss is the major cause of the safety issues in lithium batteries such as battery fires and explosions. To mitigate the safety concerns, it is imperative to understand the chemistries that promote organic, liquid electrolyte decomposition, electronic and structural changes, chemomechanical breakdown, and irreversible phase transformations. Each of these components leads to decreased battery performance.

The work in this dissertation describes model and practical platforms to probe and understand the chemistries associated with battery performance degradation. A variety of analytical methods were utilized to determine overall structure-activity relationship trends and are

highlighted in ***Chapter 2***. ***Chapters 3-5*** is technical research providing insight on Ni-rich layered oxide degradation pathways and behaviors. The work advances the understanding of battery surface chemistry which will lead to improved cathode design. As batteries continue to grow, it is important to know other applications that benefit from the unique chemistry of Ni-rich layered oxide materials. By exploiting the lithium battery cathode chemistry, this dissertation highlights a method to utilize these materials to understand the role of metal oxides on Au nanocatalysts. Conclusions to the findings in this dissertation are provided in ***Chapter 6***. Future perspectives on the technical research provided herein this dissertation is included in ***Chapter 7***. Additionally, ***Chapter 7*** details future perspectives for lithium batteries and how they can facilitate the global transition toward a sustainable future.

DEDICATION

Obtaining a doctorate has been my lifelong dream. Intellectual challenge resided at the core of my studies and this accomplishment would be impossible without discipline, sacrifice, and the loving support of family and friends. I am ecstatic to achieve this goal and am grateful to have been blessed with this opportunity. Chemistry has evolved me into the woman I am by teaching the fundamentals of life, promoting me to excel past my limits, and solidifying that science will never know more than the Creator.

While I am thrilled to have reached this milestone, I complete it with great sorrow that my best friend and true believer in my dreams will not celebrate this moment with me. To Annie Rountree, my grandmother whom I lovingly called Babe, although you passed away roughly six months prior to me reaching this goal, words cannot express the infinite gratitude I have for the wisdom, love, support, encouragement, and guidance you provided me throughout my life. I am sorrowful that you miss this moment, but confidently know you are proud of me. To my beloved mother, Charyl Waters, thank you for being a constant voice of reason, a guide throughout my academic journey, content editor, and prayer warrior for my continued success. These last few years I have gained a greater appreciation for your strength and perseverance as not just my mom, but as an intelligent, goal-driven, unconditionally loving woman. To my father, Kenneth Waters, I thank you for the love, sacrifice, and financial support that has filled my educational journey with optimism. I hope to bravely model after your leadership and transparency as I matriculate into my career.

To my family, you have made me stronger and more determined. As the first doctor of my family I take this role with great honor, hoping to inspire the next generation towards even higher success and accomplishments. To my confidant, supportive friends, and graduate school

colleagues, I am grateful for your continued companionship, the provision of listening ears, advice towards overcoming life challenges, and the shared celebration of milestones achieved along the journey.

I dedicate this work to all the Black children dreaming of being a scientist. Although teachers may doubt your abilities, know your worth and your desire to succeed will catapult you forward. To people often overlooked and undermined by their community, know that your unique experiences set you apart from the masses. To those with seemingly oppressed voices, remember that your voice matters despite what others may want you to believe.

Lastly, to an older version of myself that may become weary of life not seeming perfect or fair, remember the lifetime of dedication you invested. Know that you are more than capable of achieving anything to which you put your mind. Sometimes the physical eyes do not see the entire picture, but true vision resides in the spirit.

While fulfilling these dreams it proved difficult, but it was absolutely possible. God can transform tragedy to triumph, tests into testimonies, and the impossible into the unimaginable. I thank and praise God for blessing me with such a life-changing opportunity and accomplishment, and for guiding me on my predestined path.

To God be all the glory! It is so.

ACKNOWLEDGEMENTS

This work would be impossible without the mentorship, guidance, and encouragement from my doctoral advisor, Dr. Feng Lin. As one of your first students, I have witnessed your growth as an advisor and watched you build a productive, innovative powerhouse of a research group. From the first day meeting you, I was inspired by your charisma and enthusiasm for materials chemistry and energy storage. I thank you for your support in promoting my continued success and maturity as a scientist. I am grateful for the tools you provided me these past five years, as they serve as the foundation for building my career in battery science.

To my committee members, I appreciate how you challenged and guided me through the doctoral program and into a career. Dr. John Morris, thank you for advocating for my success and assisting me in obtaining my goals. I am grateful for your open-mind and willingness to provide resources to alleviate the stress of balancing research, classes, and teaching. Dr. Joseph Merola, I thank you for academically challenging me and asking the tough questions. While I may have been frustrated during the questioning, I now understand that it facilitated improved critical thinking skills and advanced my scientific innovation. Dr. Hongliang Xin, I appreciate your unique perspective and advice towards promoting a high standard of scientific research. Although we did not scientifically collaborate as much as initially expected, your rapid feedback and genuine care for my success was transparent and obvious.

I would like to acknowledge the collaborators at the Stanford Synchrotron Radiation Lightsource, Advanced Photon Source at Argonne National Lab, Brookhaven National Lab, Oak Ridge National Lab, and those abroad. Special thanks to the Virginia Tech facilities and staff for characterization services including ICTAS, NCFL, Dr. Mehdi Ashraf-Khorassani (GC-MS), and Dr. Xu Feng (XPS). I am thankful to each of the Lin group members, past and present, who have

helped challenge and uplift me on this academic journey. Muhammad Mominur Rahman and David Kautz – we will always remember starting a lab together in 2016 and being the Lin groups first PhDs! You two plus Stephanie Spence are not only colleagues, but true lifelong friends.

I am grateful to the Virginia Tech Chemistry department faculty and staff that aided me in being an accepted part of this community. I am forever grateful to Claudia Brodkin and Dr. Karen Brewer for initiating my research efforts here at Virginia Tech in Summer 2014. To Dr. Marcus Cooke, I thank you for being in the NC DMV line that day I was working. You helped me build connections at Virginia Tech that will now last a lifetime. You introduced me to my academic grandfather, Dr. Harold McNair. Although he has passed away, I am forever grateful for the financial support he provided annually towards me fulfilling my dreams. His guidance and knowledge are unmatched.

None of this work would have been possible without financial support from the chemistry department, the Graduate School, Dr. Harold McNair, and Dr. Marcus Cooke. Additionally, grant funding from the Department of Energy, the National Science Foundation, and the ACS Petroleum Research Fund was required for this research to be possible.

ATTRIBUTION

Chapter 3 is a modified manuscript prepared for submission in a peer-reviewed scientific journal. Crystal K. Waters led the project, performed materials synthesis, electrochemical data acquisition and analysis, GC-FID data acquisition and analysis, synchrotron X-ray absorption data analysis, XPS analysis, lab-based XRD pattern acquisition and analysis, and manuscript preparation. Dr. Feng Lin conceived the project. Dr. Yan Zhang, Dr. Muhammad Mominur Rahman, Dr. Dennis Nordlund, and Dr. Cheng-Jun Sun acquired the X-ray absorption data. Dr. Muhammad Mominur Rahman performed the TEM. Dr. Chunguang Kuai assisted in the electrochemical data acquisition. Dr. Medhi Ashraf-Khorassani assisted in collecting GC-MS data and setting up the GC-FID used for future studies.

Chapter 4 is a modified version of the manuscript submitted to *Chemical Communications*. Crystal K. Waters led the project, performed the materials synthesis, electrochemical testing, lab-based XRD data acquisition and analysis, synchrotron X-ray absorption analysis, and manuscript preparation. Dr. Feng Lin conceived the project. Dr. Linqin Mu and Dr. Chunguang Kuai assisted in the EXAFS analysis. Dr. Lu Ma, Dr. Sami Sainio, Dr. Dennis Nordlund, Dr. Cheng-Jun Sun, and Dr. Enyuan Hu performed X-ray spectroscopy acquisition.

Chapter 5 is a modified manuscript prepared for submission in a peer-reviewed scientific journal. Crystal K. Waters led the project, performed materials synthesis, UV-Vis spectroscopy data acquisition and analysis, lab-based XRD acquisition and analysis, synchrotron X-ray absorption spectroscopy analysis, XPS data analysis, and manuscript preparation. Dr. Feng Lin conceived the project. Stephanie Spence assisted in designing the catalysis experiments (UV-Vis). Dawei

Xia, Yuxin Zhang, and Dr. Cheng-Jun Sun performed the synchrotron X-ray spectroscopy data acquisition.

TABLE OF CONTENTS

CHAPTER 1: INTERFACIAL CHEMISTRIES OF FRAGILE OXIDE CATHODES AND LIQUID ELECTROLYTES

1.1 Li-ion Batteries and the Energy Revolution

The energy revolution is catapulted by a necessity to decrease the carbon footprint which is negatively impacting global climate change. As the global carbon footprint continues to increase due to the utilization of fossil fuels and non-renewable energy sources, there is a demand for clean energy generation and storage. The energy transition provides a platform to begin minimizing the negative effects and inspiring a global trend towards clean energy.

Li-ion batteries reside at the pinnacle of the energy revolution. As the demand for consumer electronic devices and electric vehicles continues to grow, there is an increased need for multitudinous approaches towards synthesizing oxide cathodes with high theoretical capacity and Coulombic efficiency. In many cases, high theoretical capacity is challenging because certain classes of oxide cathode materials lack structural robustness and considerable safety concerns exist during operation. Transition metal oxides (TMOs) are readily employed as Li-ion battery (LiB) oxide cathodes.[1–5] Fragile TMO systems possess inherent electronic and structural instability that promote oxide cathode degradation. Cathode degradation manifests as decreased battery performance metrics including battery efficiency and cycle life. There are four main categories of fragile metal oxides including Ni-rich layered oxides (NLOs)[6,7], Li-rich layered oxides (LLOs)[8–10], Li/Mn-rich layered oxides (LMR)[11,12], and disordered rocksalt[13–16], in which this dissertation largely focuses on Ni-rich layered oxides.

Layered oxide materials have the typical formula $LiMO_2$ (M = 3d transition metal). Since lithium cobalt oxide ($LiCoO_2$ or LCO) was commercialized by Sony in 1991, there has been a continuous drive toward improved cathode materials. Li-based layered TMOs have gained much attention in recent years due to intercalation chemistry that drives rechargeability in these systems. In 2019, the Nobel Prize in Chemistry was awarded for the development of Li-ion batteries. Over the past few decades continued efforts towards new chemistries for Li-ion batteries (LiBs) gain interest globally. Much work has been completed on $LiCoO_2$. Nevertheless, the nickel analog has gained much attention as an improved commercialized cathode material for many emerging energy markets. This migratory trend towards minimal cobalt usage to Co-free layered oxide materials[17,18,19] has increased due to the geopolitical issues relating to human rights and labor laws in cobalt mining. Additionally, materials are constantly evolving due to the demand for cost-effective, low toxicity, earth abundant metals.

Herein this dissertation, the technical research focuses on Ni-rich layered oxides, including $LiNiO_2$ (LNO) and $LiNi_xMn_yCo_zO_2$ (x+y+z = 1) (NMC) materials. The following sub-sections of ***Chapter 1*** will review the electronic and structural properties of Ni-rich layered oxides. Additionally, it describes the interfacial chemistries of Ni-rich layered oxide materials with liquid-based organic electrolyte solvents. This chapter will discuss the cathode-electrolyte interphase (CEI) components, as well as strategies towards minimizing undesired, parasitic reactions that promote battery performance degradation.

1.1.1 Ni-rich Layered Oxide Materials

$LiNiO_2$ was first introduced[20] in 1954, but there has been a recent surge in utilizing Ni-rich layered oxides (NLOs) as cathode material due to its high practical discharge capacity (>200 mAh

g^{-1}) and energy density.[21] Nickel analogs of Co-based layered oxide materials have a similar theoretical capacity due to comparable molecular weights. Nevertheless, the practical capacity of Ni-containing layered oxides is higher than Co-based materials due to the ease of oxidizing nickel compared to cobalt. While Ni-rich layered oxide materials are emerging in the commercial market, when Ni content exceeds 80% of the total transition metal content many challenges arise. These electronic and structural challenges of Ni-rich layered oxides delay widespread commercialization of >80% Ni-containing cathode materials.

Layered transition metal oxide materials are synthesized using a co-precipitation[17], a hydrothermal[22], or solid-state[23] method. While researchers have synthesized layered oxide materials using each of these methods, the materials synthesized for research reported in this dissertation were synthesized using the co-precipitation method. Specific synthesis methods are embedded within the technical chapters, as small modifications for improved phase purity may have been employed.

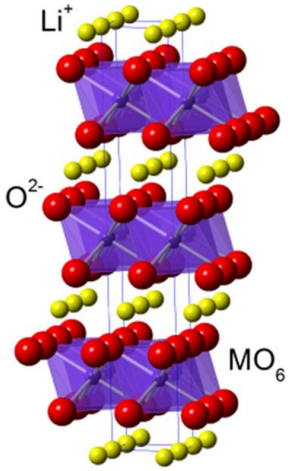

FIGURE 1: Layered transition metal oxide structure with an R$\bar{3}$m space group. The metal cation is octahedrally coordinated by oxygen anions, making up the metal oxide layers. The electronic repulsion of the oxygen anions is alleviated by the Li^+ located between the metal oxide layers. The Li^+ can be de-/intercalated for charging and discharging in battery applications.

Figure 1 illustrates the layered transition metal oxide structure. In the structure, the transition metal is octahedrally coordinated by oxygen anions. The metal cations and oxygen anions are arranged in a hexagonal configuration that make up the metal oxide layered framework. Li^+ reside in the octahedral sites located between the metal oxide layers. The Li^+ are deintercalated during charging and intercalated during discharging to balance the electronic charge. There are practical synthesis challenges associated with Ni-rich layered oxide materials. Many of the challenges are derived from the electron and oxygen transfer pathways that are not well-understood due to the dynamic structure and electronics of Ni-rich layered oxide materials. The synthesis challenges, surface reactivity, and oxide cathode-electrolyte interfacial reactions each increase the complexity of understanding how to mitigate the challenge of commercializing high Ni content cathode materials.

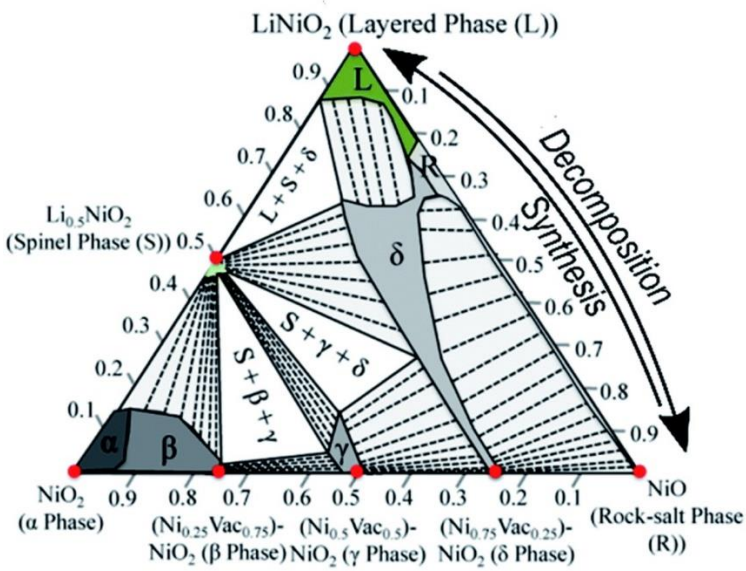

FIGURE 2: The phase diagram of $LiNiO_2$, illustrating the equilibrium that exists between the layered and rock-salt phase. This diagram highlights the structural dynamics between synthesis and decomposition of Ni-rich layered oxide materials. [Modified from Reference[24]]

During synthesis, off-stoichiometry in Ni-rich layered oxides is common and it originates from lithium loss ($Li_{1-x}Ni_{1+x}O_2$) and the presence of Ni^{2+}.[21] Additionally, during high temperature synthesis methods (>700 ºC), it is challenging to maintain the Ni^{3+} due to its unstable nature in the structure and its ability to migrate into Li^+ sites due to similar atomic size. The ionic radius of Li^+ and Ni^{2+} is 0.76 Å and 0.69 Å, respectively.[25] When Li/Ni cationic mixing occurs, Li diffusion must overcome a higher activation energy barrier. Therefore, the structural instability caused by Li/Ni cation mixing during synthesis continues to propagate during the electrochemical charge/discharge cycles.[26–28] As shown in **Figure 2**, an equilibrium exists between synthesis of the layered material and decomposition to the rock-salt phase. This highlights the dynamic structure associated with Ni-rich layered oxide materials. Structural phase impurities, caused by cation mixing at high calcination temperatures[29] can limit optimal Li^+ diffusion rates, causing rapid specific capacity fading and poor overall battery cyclability.[30] The following ***Section 1.1.2*** will further discuss electronic and structural influences on the cathode instability and degradation pathways that facilitate inferior performance metrics in Li-ion battery systems.

1.1.2 Electronic and Structural Influence on Cathode Instability

Ni-rich materials have structural fragility due to various factors including cation disordering[27,30], phase transformations[31], oxygen release[32–34,35], and microcrack propagation in the secondary particle[36–38,39]. Most of these phenomena are greatly influenced by charge/discharge parameters, such as the charging rate and upper cutoff voltage. The charging rate, also referred to as the C-rate, influences the stability of the material. It can also impact the interfacial decomposition reactions that occur between the oxide cathode and liquid-based, carbonate-containing electrolytes. C-rates provide information regarding the time in which a battery is

charged/discharged. For example, 1C means that the cell is charged in 1 hour and discharged in 1 hour. If the C-rate equals 0.1C, the cell charges and discharges in 10 hours, or 10 times slower than 1C. C-rates can influence the oxide cathode stability because the chemistries associated with the materials properties, such as structural disordering and phase impurities, are complicated by the rate at which cathode – electrolyte interfacial electron transfer pathways proceed.

An interplay between electronic and structural changes greatly influence the stability of Ni-rich layered oxide material upon applying high voltages. During charging the oxidation state of the redox center, which is Ni, approaches +4 – a very unstable charge that undergoes a thermodynamically favorable driven reduction.[40] This is mostly due to the TM*3d* – O*2p* orbital hybridization that is found in layered oxide materials. **Figure 3** highlights the energy diagram associated with the thermodynamically favorable transition metal reduction and oxygen loss.

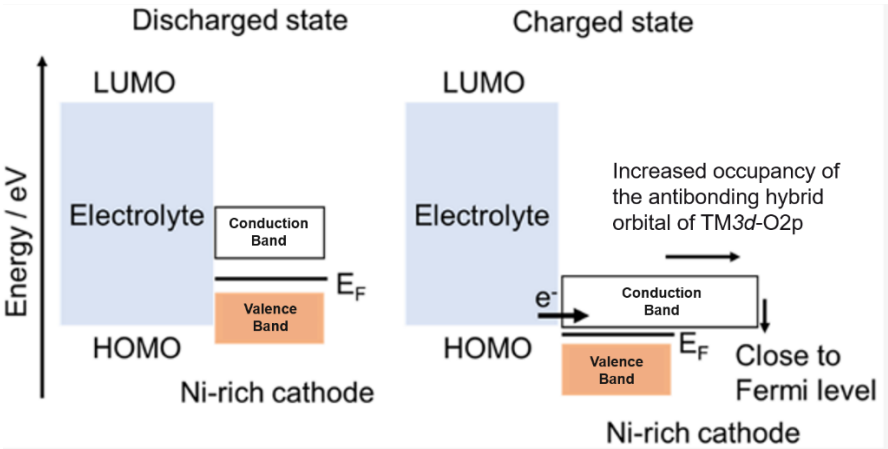

FIGURE 3: Energy diagram of the electrolyte and Ni-rich cathode in the discharged/charged state illustrating the thermodynamically favorable electron transfer from the $HOMO_{electrolyte}$ to the conduction band of the Ni-rich cathode after the decreasing of the Fermi energy. This electron transfer leads to an increased occupancy of the antibonding hybrid orbital of TM*3d*-O*2p* orbital. [Modified from Reference[40]]

In the discharged state, the lithium ions are located between the metal oxide layers, as shown in **Figure 1**. In the energy diagram (**Figure 3**), the y-axis represents the relative energy of the highest occupied molecular orbital (HOMO) and the lowest unoccupied molecular orbital (LUMO) for the electrolyte, in comparison to the valence and conduction band of the Ni-rich layered oxide material. As the cathode undergoes charging, Li ions are deintercalated from the lattice structure causing transition metal oxidation and a decrease of the Fermi energy. Upon lowering the Fermi energy, a thermodynamically favorable electron transfer pathway from the HOMO of the electrolyte to the conduction band of the Ni-rich layered oxide is generated. After electron transfer, the occupancy of the antibonding TM*3d*-O*2p* hybrid orbital increases leading to a lengthened TM*3d*-O*2p* bond. At very high states of charge, the aforementioned electron transfer pathways promote oxygen loss and transition metal reduction, facilitating phase impurities that propagate through the material due to the increased likelihood of metal migration.[41] Many researchers expect that the electronic and structural perturbations during charging directly account for the irreversible capacity associated with these materials.[42,43]

Surface reconstruction is a phenomenon that is a result of the combined phenomena of metal migration and oxygen release in oxide cathodes. In Ni-containing layered oxide material, there is a positive correlation between increased Ni content and structural phase impurity. An example of structural phase impurity is shown in **Figure 4**. Scanning transmission electron microscopy (STEM) is utilized to determine the local structural arrangements. The bright spots are indicative of transition metal cations, due to their high atomic weight compared to Li^+. The STEM image highlights that the bulk of the material possesses the anticipated layered structure, whereas the surface rearranges to a rocksalt phase. The STEM image strongly illustrates how Ni cations inhabit Li^+ sites, blocking (de-)intercalation pathways, leading to decreased Li^+ diffusion

rates. The complexity in understanding the phenomenon associated with surface reconstruction lies in the interplay of bonding arrangements and oxide cathode surface reactivity. For improved battery design this proves challenging because collaboratively cation mixing and oxygen loss induce electrolyte decomposition at the cathode-electrolyte interphase[44]. This collaboration disrupts optimal battery performance.

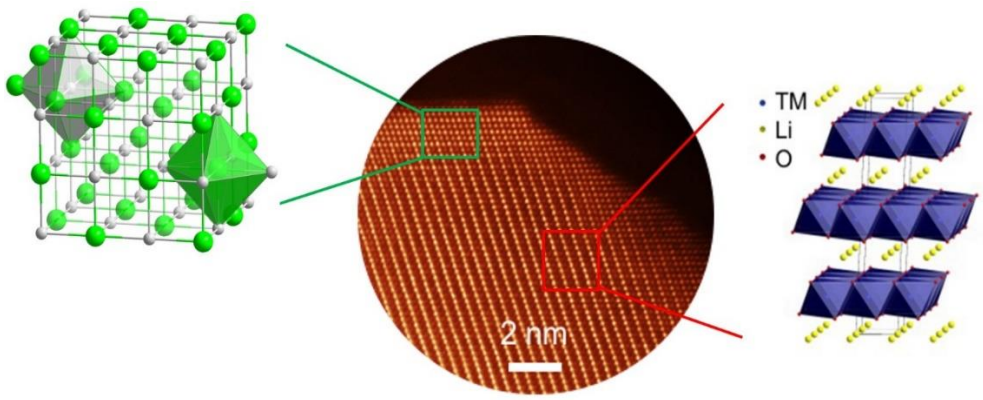

FIGURE 4: Layered oxide surface reconstruction phenomenon, in which the bulk structure retains layered structure whereas the surface undergoes transformation to rocksalt structure. This phase impurity layer is caused by Ni cations inhabiting Li^+ sites and surface-most lattice oxygen loss. [Modified from Reference[30]]

Researchers quantify oxygen evolution from Ni-rich layered oxide materials using various analytical techniques. During charging, oxygen evolution is evident at high onset potentials. The oxygen evolution reaction is attributed to both Ni and O redox couples.[45,46] As the Ni content in the material increases, the onset potential for oxygen evolution decreases.[47] NMC111 and NMC811 have an onset potential for oxygen evolution at ~4.6 and ~4.2V vs Li/Li^+[48]. This highlights that increased Ni content requires lower potentials for irreversible structural instability to be present.

Oxygen evolution is largely associated with the H2 → H3 phase transition in Ni-rich layered oxide materials.[49] The H2 → H3 phase transition exists at high states of charge and has the greatest negative influence on the overall intrinsic stability of $LiNiO_2$ and other Ni-rich layered oxide materials. The structural instability in $LiNiO_2$ can be analyzed using neutron diffraction (**Figure 5**).[50]

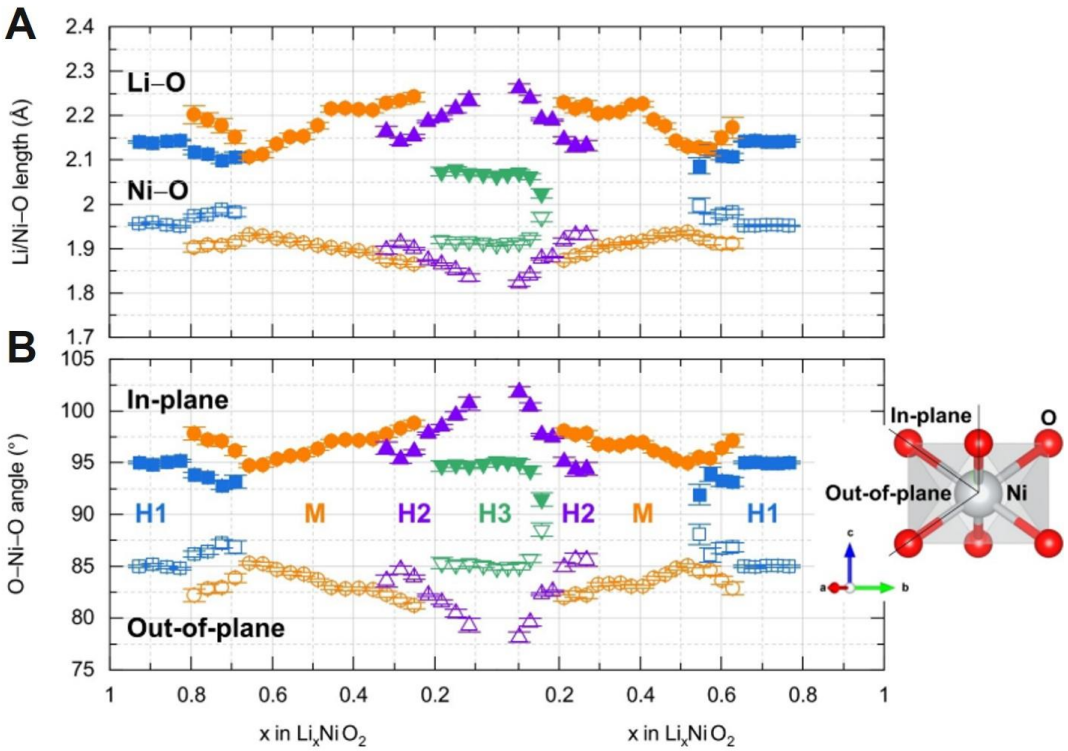

FIGURE 5: Li_xNiO_2 || graphite full cell as a function of Li content in the first cycle. During charge/discharge **A)** Li/Ni-O bond length evolution is shown. **B)** The O-Ni-O bond angles in and out-of-plane are included as a function of Li content. The data was derived by parametric Rietveld refinements. [Taken from Reference[50]]

The neutron diffraction study shows that during charge and discharge, the $LiNiO_2$ structure is very dynamic. The evolution of bond length (**Figure 5A**) shows that during charging the Li-O bond

increases until the H2 phase transition. On the contrary, the Ni-O bond decreases until the H2 phase. The Li/Ni-O bond lengths in the H3 phase suggest that the highlight delithiated states are mainly responsible for the structural collapse. To corroborate the structural transformation, the O-Ni-O bond angles (**Figure 5B**) are analyzed using Rietveld refinement for neutron diffraction. The O-Ni-O bond angles are indicative of structural distortions in the NiO_6 octahedra. During delithiation, the O-Ni-O angles are deviated from the 90º with opposite trends in-plane and out-of-plane angles. During charging, the NiO_2 structures are compressed and greatly distorted. Upon high states of charge, the Li^+-depleted H3 phase is released to have a similar O-Ni-O angle to that of the H1 phase.

Much of the intrinsic stability is compromised due to internal strain of the primary and secondary particles, leading to the decreased cycling stability.[51]

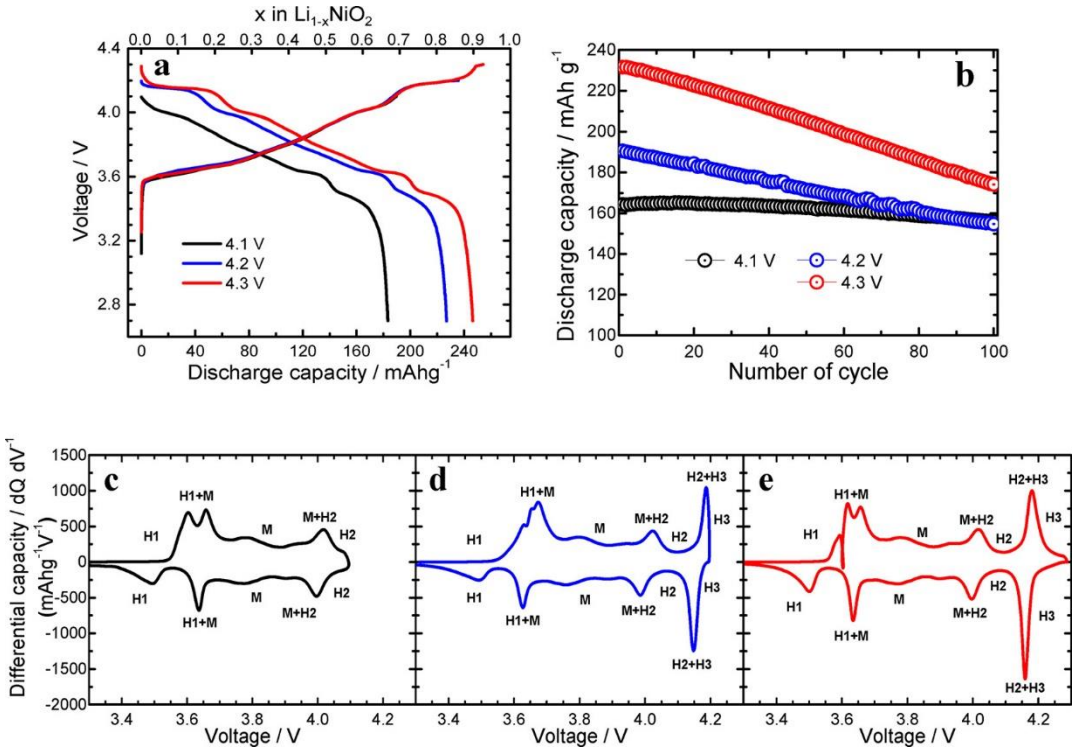

FIGURE 6: Electrochemical testing of $LiNiO_2$ cathodes at 4.1, 4.2, and 4.3 V vs Li/Li^+ upper cutoff voltages. **A)** The initial charge/discharge curves for each of the cutoff voltages is shown, illustrating that higher cutoff voltages generate higher discharge capacity. **B)** The capacity fading for each of the cutoff voltages shows that there is much more rapid fading associated with the 4.3 V vs Li/Li^+ in comparison to the lower cutoff voltages. The differential capacity plots are included for **C)** 4.1, **D)** 4.2, and **E)** 4.3 V vs Li/Li^+, illustrating the irreversibility of the H2 → H3 phase transition. [Taken from Reference[52]]

Yoon and coworkers illustrated[52] in their work that increased cutoff voltages are associated with higher discharge specific capacity (**Figure 6A**). Nonetheless, there is also much more rapid capacity fading with increased upper cutoff voltages (**Figure 6B**). When comparing the differential capacity for the 4.1, 4.2, and 4.3 V vs Li/Li^+ as the upper cutoff voltages, there are phase transitions of H1 → M, M → H2, and H2 →3. The 4.1V vs Li/Li^+ upper cutoff voltage has no H2 → H3 phase transition and therefore lacks oxygen evolution which is detrimental to structural stability (**Figure 6C**). At the 4.2V vs Li/Li^+ upper cutoff voltage, the H2 → H3 phase transition is present, suggesting that there is some oxygen evolution in the material (**Figure 6D**).

When comparing the 4.2V to 4.3 V vs Li/Li^+ the irreversible phase transition has a much greater differential capacity (**Figure 6E**). This study provides a basis for exploring the chemical phenomena that lead to the irreversibility of these transformations.

While much work has been dedicated to understanding the electronic and structural influence on layered oxide degradation, specific capacity fading, and inferior Coulombic efficiency, the mechanisms by which oxygen evolution and cation mixing occurs is not well-understood. It is important to understand these mechanisms to predict how these phenomena lead to irreversible capacity fading and dangerous events such as thermal runaway, battery fires, and catastrophic explosions. One major analytical challenge is that researchers are limited by the lack of kinetic information associated with oxygen vacancy formation to predict these mechanistic pathways.

Environmental transmission electron microscopy (ETEM) was used to investigate the role morphology, structural, and chemical changes had on individual particles in real time.[53] The goal of the study was to explore the role oxygen has on TM ion rearrangement at the surface and bulk of Ni-rich $LiNi_xCo_yAl_zO_2$ (NCA) materials at elevated temperatures. Karki and coworkers illustrated that after oxygen evolution, HRTEM coupled with Fast fourier transform (FFT) show that the particle has transformed from layered to rocksalt phase at increased temperatures. Additionally, the O K-edge has perturbations in the pre-edge features due to a change of the TM*3d*-O*2p* orbital hybridization occupancy.

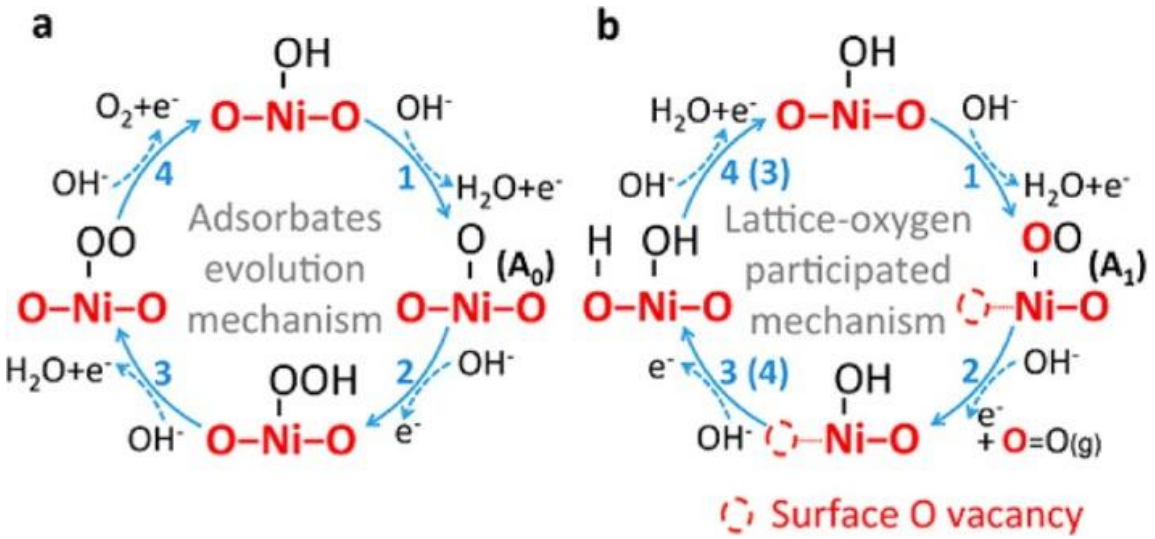

FIGURE 7: $LaNiO_3$ surface reactivity to **A)** adsorbates and **B)** lattice-oxygen participating in the oxygen evolution reaction (OER). [Taken from Reference[54]]

Density functional theory (DFT) is useful when predicting oxygen evolution in oxide materials. Although not a layered Ni-rich material, $LaNiO_3$, a perovskite oxide, was studied to determine how adsorbates and lattice-oxygen can participate in the oxygen evolution reaction.[54] **Figure 7** provides the two predicted pathways in which the oxygen evolution can occur – via an adsorbate mechanism (**Figure 7A**) or a lattice – oxygen facilitated mechanism (**Figure 7B**). $LaNiO_3$ provides some insight into how $LiNiO_2$ decomposition generates oxygen evolution. A major difference to consider is that lattice oxygen is kinetically inhibited from being loss from the bulk of the material.

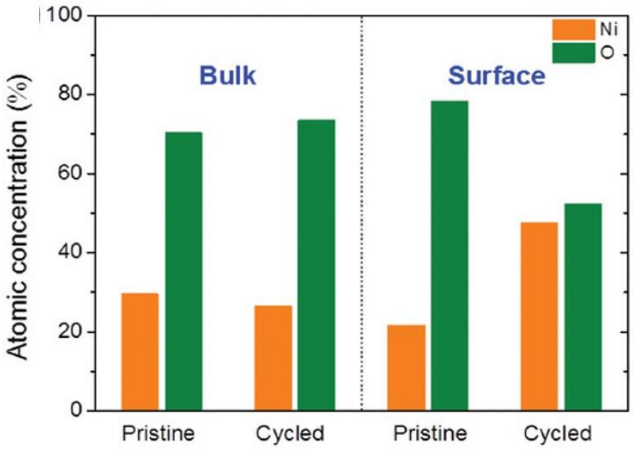

FIGURE 8: The relative Ni and O atomic concentration (%) in the bulk and surface of $LiNiO_2$|Li half-cell after 100 cycles at 0.5C with an upper cutoff voltage of 4.3V vs Li/Li^+. EDS and XPS were used to determine the atomic concentrations. In the bulk of the material, Ni and O atomic concentrations are roughly the same in the pristine and cycled state. The surface of the material has a decreased O atomic concentration, suggesting that surface lattice oxygen loss is more kinetically favorable. [Taken from Reference[55]]

Kong et al. quantitatively illustrate that bulk lattice oxygen loss is kinetically unfavorable.[55] A half-cell is assembled with a $LiNiO_2$ cathode and Li metal anode. The cell is cycled for 100 cycles at 0.5C with an upper cutoff voltage at 4.3V vs Li/Li^+, which is typical when determining the amount of oxygen evolution from a Ni-rich layered oxide material. Pre- and post-mortem cathode analysis was completed using energy dispersive X-ray spectrometry (EDS) and X-ray photoelectron spectroscopy (XPS). By coupling these methods, Kong and coworkers determine that the Ni and O ratios for the pristine and cycled samples from the bulk remained roughly the same. The atomic concentration at the surface of the material after cycling has a much lower atomic concentration of O compared to the pristine sample. This suggests that oxygen was lost exclusively from the surface of the layered oxide material. The results from this study are highlighted in **Figure 8**.

Oxygen evolution is key in understanding the interfacial reaction pathways in Ni-rich layered oxide materials. While much work on quantifying oxygen loss has been completed, much work is still required to understand the mechanism for lattice oxygen loss in Ni-rich materials. This dissertation seeks to answer those questions and provide insight into the chemistries that negatively influence the electronic and structural stability of Ni-rich layered oxide cathodes. Lattice oxygen loss and cation mixing, coupled with Li loss and transition metal dissolution promote many of the side reactions at the oxide cathode-electrolyte interphase (CEI). ***Section 1.2*** focuses on oxide cathode-electrolyte interfacial reactions and its associated properties.

1.2 Oxide Cathode – Electrolyte Interfacial Properties

The cathode-electrolyte interphase (CEI) is very dynamic and unstable. To understand the mechanisms at the CEI, it is important to determine the interplay between the structural transitions and electronic perturbations at various states of charge in the material. Fragile oxide materials, particularly Ni-rich materials, undergo various structural and electronic perturbations during charging, especially voltages >4.2V vs Li/Li^+.[52] Cation mixing, transition metal dissolution[56–59], and oxygen loss all complicate the understanding of electron and oxygen transfer pathways at the CEI. During lithium extraction, Ni^{2+} oxidizes to be close to Ni^{4+}. Tetravalent Ni is extremely reactive and has a significant role in the structural rearrangement of layered oxide materials. As the redox center undergoes oxidation state changes during charging and discharging, the reactivity of oxide cathode surface also changes.

Ongoing research focuses on fundamental investigations to clarify the mechanisms of CEI formation and evolution.[60] The CEI is directly influenced by properties of the layered oxide cathode, as well as electrolyte oxidation, as provided in **Figure 9**.

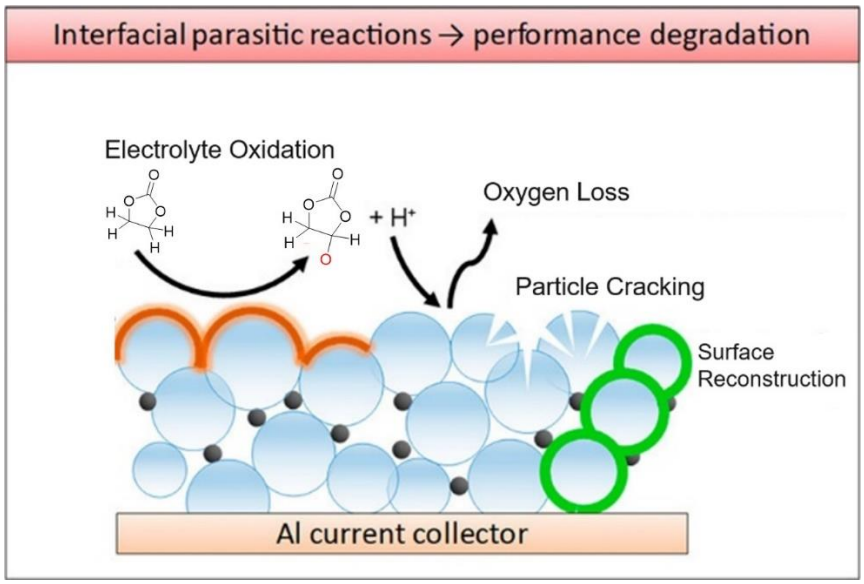

FIGURE 9: Oxide cathode – electrolyte interfacial reactions that lead to performance degradation in Ni-rich layered oxide materials. [Modified from Ref[61]]

Electrolyte decomposition reactions at the cathode surface generate a plethora of chemistries which facilitate battery performance degradation. Electrolyte oxidation at the metal oxide surface is one cause for unwanted surface films that limit Li^+ diffusion kinetics. Liquid-based carbonate containing electrolytes undergo oxidation reactions at the oxide cathode surface which are driven by the cooperativity of oxygen loss and transition metal reduction. This also promotes transition metal dissolution through Li-salt decomposition pathways. The complexity of studying Ni-rich layered oxide materials derives from the interplay between surface and bulk chemistries that must be decoupled to gain a complete depiction of degradation behaviors.

On the secondary particle level, liquid electrolytes can infiltrate the grain boundaries of the material resulting in chemomechanical breakdown. Microcracks are not only caused by CEI

reactions, but can also be facilitated by mechanical stress and electrostatic repulsion during charging.[39]

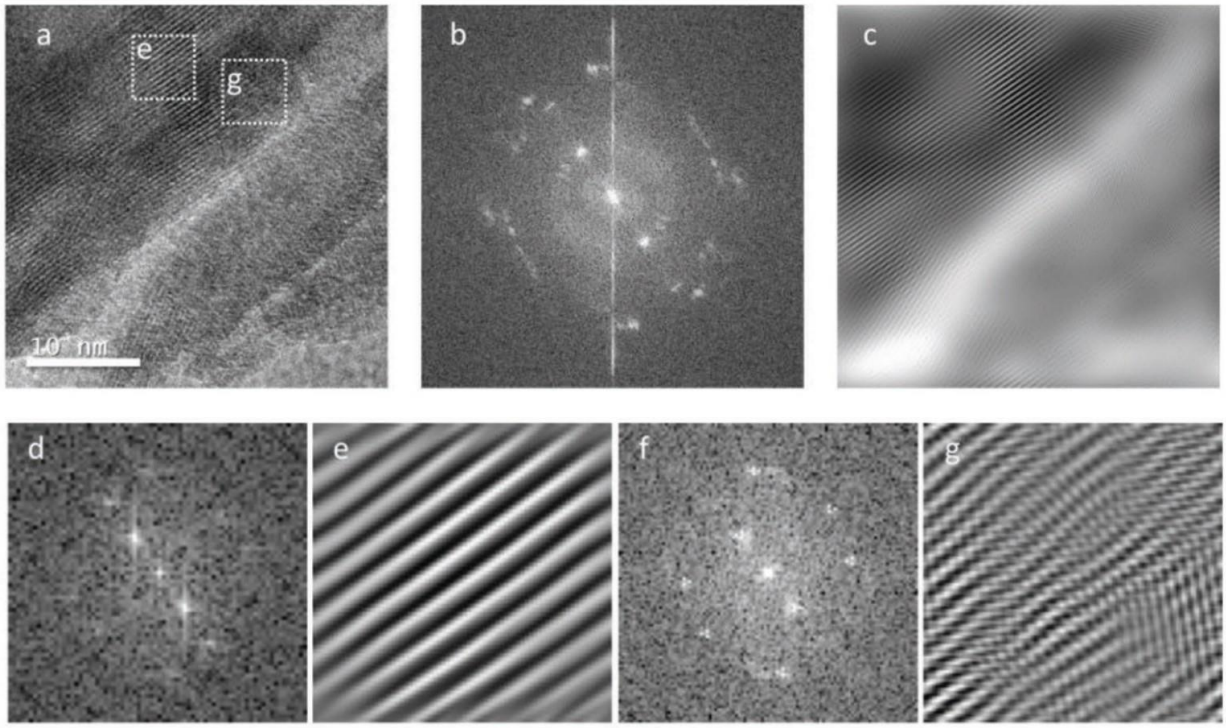

FIGURE 10: $LiNi_{0.6}Mn_{0.2}Co_{0.2}O_2$ (NMC622) material. **A)** TEM image revealing the mixed rocksalt and layered structure. **B, C)** The fast Fourier transform (FFT) and inversed FFT (IFFT) of the TEM image shows the co-presence of the two structures. The **D, F)** FFT and **E, G)** IFFT at the selected regions of interest illustrate the layered and rocksalt phases, respectively. The regions of interest are highlighted by the white dotted squares in **A**. [Taken from Reference[39]]

In illustrating chemomechanical breakdown, **Figure 10** highlights the co-presence of the layered and rocksalt structures in NMC622. The difference of the two atomic structures is illustrated in the TEM image (**Figure 10A**). By utilizing fast Fourier transform (FFT) and inversed FFT (IFFT), the images corroborate the two structures. The FFT images (**Figure 10D, F**) show that the bulk structure remains layered whereas the surface structure transforms into rocksalt. The

IFFT image (**Figure 10E**) illustrate defined rivets at the bulk of the microcrack, highlighting structural ordering. At the surface of the crack, the IFFT image illustrates undefined rivets that highlight the structural disordering (**Figure 10G**). To determine the interplay of these phenomenon that impact battery performance, electronic and structural influences must be individually considered. Additionally, chemistries at the surface and bulk of the material must be deduced to understand the mechanisms that promote oxide cathode degradation.

1.2.1 Electrolytes for Lithium Batteries

Lithium battery electrolytes serve a unique role in comparison to the complex chemistries that exist in and between the electrodes. The role of the electrolyte is to serve as a medium to transfer charge through ions between the cathode and anode. Electrolytes consist of two major components, a Li-salt and a solvent. Many lithium battery systems include a nonaqueous, carbonate containing liquid electrolyte solvent including but not limited to ethylene carbonate (EC), dimethyl carbonate (DMC), and or ethyl methyl carbonate (EMC). In many cases, a combination of carbonates are employed for optimal viscosity and Li-salt dissolution. $LiPF_6$ is the most widely used Li-salt employed in lithium battery electrolyte systems. It is widely used because of its well-studied thermal stability in carbonate electrolyte solvents.[62]

Lithium batteries have many safety concerns surrounding the flammability of liquid carbonate electrolytes. Electrolyte choice, including solvent and Li-salt, is important when developing a novel or improved Li-ion battery system. An appropriate electrolyte selection is made based on its stability within the anticipated operating potential window. The potential window is determined by the energy difference between the lowest unoccupied molecular orbital (LUMO) and highest occupied molecular orbital (HOMO) of the bulk electrolyte.[63] During the

charging process, layered metal oxide materials undergo electrochemical delithiation. In the first cycle, residual lithium species on the surface of the cathode material, such as Li_2CO_3 and LiOH, are decomposed at upper voltages leading to some of the irreversible Li loss in the material.[64] This loss of lithium can lead to some of the initial capacity fading and increase side reaction, illustrated by a decrease in the Coulombic efficiency.

While research confidently suggests the presence of Li_2CO_3 on the cathode surface, as well as other residual lithium species, all of the oxidized electrolyte species are yet to be determined and quantified. During electrochemical delithiation, the electrolyte is oxidized causing undesired side reactions that lead to the formation of surface films. A stable interphase between the cathode and electrolyte is required to minimize capacity fading and decrease the safety concerns associated with flammability in lithium battery applications.

Battery fires and explosions between layered oxide materials and liquid-based electrolytes is associated with the thermal instability of lattice oxygen at highly delithiated states in Ni-rich layered oxide materials.[65] Thermal runaway in high Ni-content cathode materials is one of the great inhibitors associated with commercializing this class of materials with organic, liquid electrolytes.[66] In portable electronics and electric vehicle applications, there are a few components affiliated with battery fires including the rate of charge and discharge, the electrolyte flammability, and battery pack engineering.[67] It is imperative that research continues to improve the chemical understanding of the cathode-electrolyte interphase to mitigate these safety concerns. ***Section 1.2.2*** describes the cathode-electrolyte interphase (CEI) components that are generated from electrode and electrolyte decomposition.

1.2.2 Ni-rich Layered Oxide Cathode – Electrolyte Interphase Components

In Ni-rich layered oxide cathodes, there are often residual lithium compounds found on the active material surface. One of the major components is Li_2O[68], most commonly introduced via excess LiOH used in the calcination process to accommodate for initial Li loss. Lithium carbonate (Li_2CO_3) is a common residual lithium species on the surface of layered oxide materials. This is large due to the surface reactivity of the material with CO_2 after calcination. Li_2CO_3 reacts with protonated species which can cause gassing during battery cycling. Lithium carbonate and other residual lithium compounds (RLCs) possess strong alkalinity, which can catalyze transesterification. RLCs lead to decomposition via oxidation of carbonate-containing electrolyte solvents. This results in battery gassing which leads to volume expansion in the cell. Li_2O, LiOH, and Li_2CO_3 each have critical roles in the cathode degradation pathways.[68]

$LiNiO_2$, the optimal Ni-rich layered material, reacts with water and carbon dioxide. When $LiNiO_2$ reactions with *x* moles of H_2O it yields $Li_{1-x}H_xNiO_2 + xLiOH$, while reactions with carbon dioxide (CO_2) form Li_2CO_3.[68] Lithium carbonate is electrochemically decomposed at potentials greater than 4.3V vs Li/Li^+. When Li_2CO_3 is electrochemically decomposed at higher voltages, it decomposes into Li^+, electrons, O_2, and CO_2 ($2Li_2CO_3 \rightarrow 4Li^+ + 4e^- + O_2 + 2CO_2$).[69] Upon cathode preparation, there is a ratio of active material to carbon black to PVDF. The CEI can also include species associated with the dehydrofluorination of the PVDF binder by LiOH in the following reaction: $[(CH_2\text{-}CF_2)_n] + LiOH \rightarrow (CH{=}CF)_n + LiF + H_2O$.[70,71]

While all of these components make up the cathode-electrolyte interphase, it is not an exhaustive list. There are many other species that reside in the CEI as a result of electrolyte decomposition pathways. Many of the products have yet to be determined or quantified due to molecular instability or thermodynamically unfavorable product formation. The cathode-

electrolyte interfacial chemistries are dictated by the electrochemical and chemical reactions that occur.[72] **Figure 11** includes some of the chemical reaction pathways that generate components of the CEI.

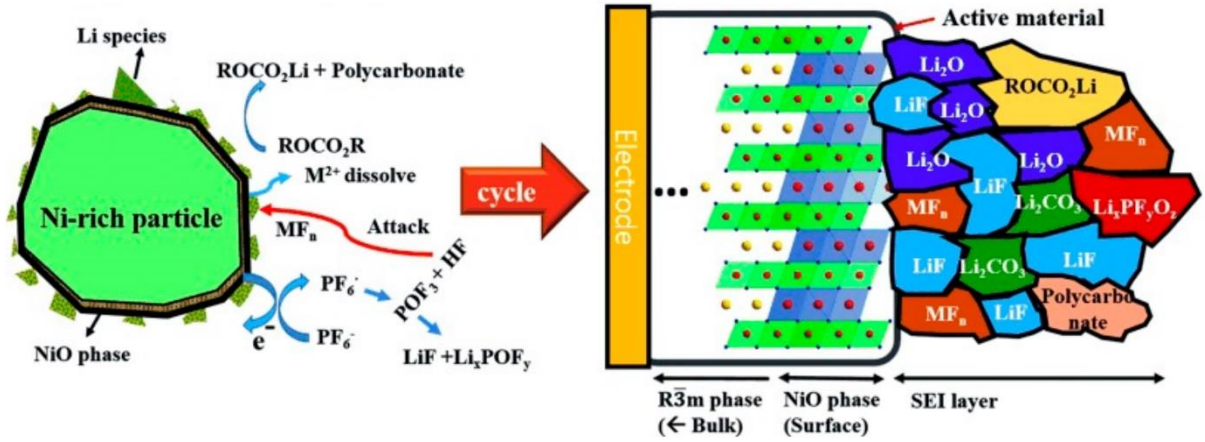

FIGURE 11: Ni-rich layered oxide particle, illustrating the NiO phase and the residual Li species. The associated parasitic reactions at the surface of the Ni-rich particle before cycling are included. After cycling, the bulk of the material remains layered, whereas the surface undergoes transformation. The electrode – electrolyte interphase layer includes many lithiated compounds from electrolyte decomposition. [Taken from Reference[68,73]]

In a typical Ni-rich layered oxide particle, there is a favorable NiO phase that is caused by cation mixing and oxygen loss, as greatly discussed in ***Section 1.1.2***. At the surface of the material, there are many decomposition products that are not widely understood due to the lack of appropriate characterization methods to explore the solid-liquid interface. After cycling, **Figure 11** highlights some of the Li-containing decomposition products predicted at the electrode–electrolyte interphase. While residual lithium species are common to the surface of Ni-rich layered oxides, they lead to phase impurity in the material after charging. Furthermore, the CEI is more unstable than the solid electrolyte interface (SEI), causing increased complexity when studied.[74]

Cross-talk exists between the cathode-electrolyte interphase and solid-electrolyte interphase (SEI) (typically used to denote the interface between the anode and electrolyte) which can complicate understanding cathode degradation in fragile TMO cathode systems. The reactions between the oxide cathode and electrolyte are suggested to be the major cause of capacity fading in the full cell.[75–78] A stable CEI is required in Li-ion battery systems because it allows Li^+ movement, yet is electronically insulating. This is critical to ensure high Coulombic efficiency, cycle life, and safety during the battery lifetime.

In understanding Ni-rich layered oxide materials chemistry, cutting-edge characterization techniques are necessary to understand the components of the cathode-electrolyte interface. These analytical strategies have proven effective when probing the CEI of various oxide cathode-electrolyte systems. Techniques such as high-resolution transmission electron microscopy (HRTEM), cryo scanning electron microscopy (Cryo-SEM), and other electron microscopy techniques, as well as X-ray photoelectron spectroscopy (XPS)[79,80], and synchrotron probes have been successfully employed.[72] Although these characterization techniques have been able to elucidate various CEI components, it is difficult to develop a physical representation of the CEI due to its instability during cycling. Most CEI studies are addressed using a trial-and-error approach instead of the strategic, step-wise approach. This further limits the ability to obtain an accurate, conclusive identity of all the decomposition products.

Ni-rich layered oxides (NLOs) have increased amounts of interfacial chemical reactions compared to other layered oxide cathodes that lack significant surface fragility and oxygen redox chemistry. Both chemical and electrochemical reactions occur on the oxide cathode side of lithium batteries.[81] The reactivity of the oxide cathode and non-aqueous electrolytes is influenced by the metal-oxygen covalency.[82] Additionally, there are increased amounts of oxygen *p* states at the

Fermi level of NLO materials. Surface oxygen loss is typical in Ni-rich materials due to kinetic stabilization of oxygen found in the bulk of NLOs.[55]

Due to the surface instability of NLOs, there are favorable electron transfer pathways that lead to electrolyte decomposition, as well as surface adsorbate decomposition. NLOs tend to oxidize electrolytic species, as well as Li-based salts.[40] These decomposition products make-up the cathode-electrolyte interphase (CEI). Some of the known electrolyte decomposition pathways are illustrated in **Figure 12**.[68]

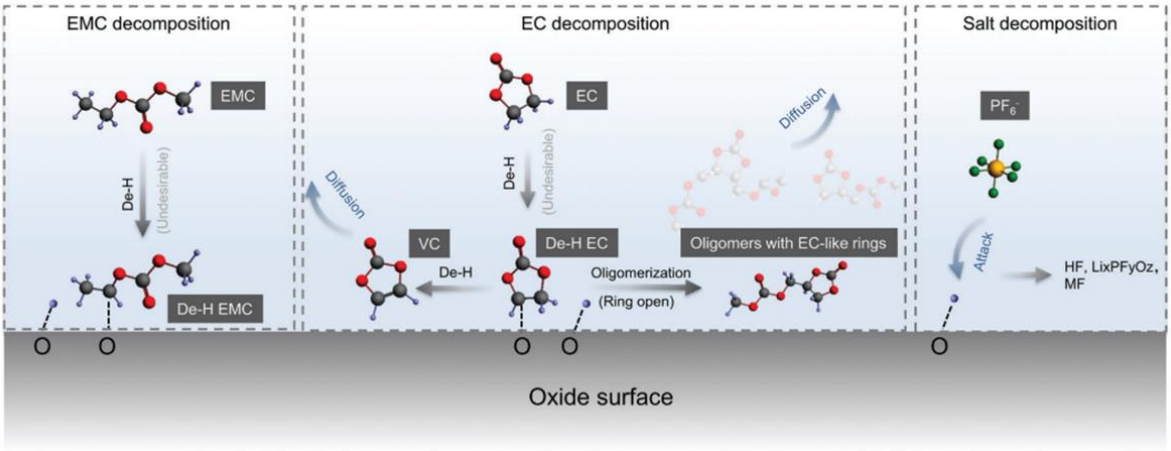

FIGURE 12: Predicted liquid electrolyte decomposition pathways for ethyl methyl carbonate (EMC), ethylene carbonate (EC), and $LiPF_6$. Each decomposition pathway leads to oxide surface degradation due to undesirable interactions with electrolytic species. [Modified from Ref[82]]

Commercial electrolytes include ethyl methyl carbonate (EMC), ethylene carbonate (EC), and Li-salt. As highlighted in **Figure 12**, EMC undergoes undesired dehydrogenation at the oxide surface leading to decomposition products. Due to the ring structure of EC, post-dehydrogenation there are a variety of decomposition pathways. Oligomerization of EC decomposition species is also expected but many of the products are not well known. $LiPF_6$ undergoes oxidation at the surface

of the oxide. It generates Li_xPF_yO species, as well as metal fluorides (MF) and hydrofluoric acid (HF). Salt decomposition is large associated with oxide structural instability due to transition metal dissolution that is complicated by reactions with HF.

Common reports suggest that Ni-rich layered oxides including LNO and NMC with >80% Ni content have increased surface reactivity with gases found in the air. This generates the formation of LiOH and Li_2CO_3 which is commonly found on the surface of fragile oxide cathodes.[83,84] This Li_2CO_3 surface layer is one cause of CO_2 evolution in fragile oxide cathodes.

Gas evolution greatly influences the performance metrics in lithium batteries. When quantifying oxygen release, both oxide cathode degradation and electrolyte oxidation are necessary to develop a working conclusion. The instability of the CEI causes great challenge when hypothesizing degradation mechanisms, especially in fragile, Ni-rich layered oxide materials. To investigate the associated oxygen release and gas evolution mechanisms, various methods can be employed.

While some methods exist to directly quantify the amounts of oxygen release and gas evolution, there are also some indirect methods to probe the structural instability of layered oxide materials. Electrochemical methods[85], such as electrochemical impedance spectroscopy, can be used to characterize the resistance of electron transfer.[86] Additionally, galvanostatic intermittent titration technique (GITT) studies can be used to obtain electrode kinetic parameters and relate it to electrochemical performance.[87,88]

1.2.3 Surface Reactivity of Layered Oxide Materials during Storage

Ni-rich layered oxide materials are polycrystalline and have complex charge heterogeneity in their structure. This results in a variety of degradation patterns, all of which are not simple to probe and understand.[89,90] To mitigate some of the challenges associated with Ni-rich layered oxide materials, particularly $LiNiO_2$, transition metal dopants have commonly been employed. A detailed discussion on the incorporation of metal dopants for modifying cathode chemistry is found in ***Section 1.3.1***.

Not only can dopants influence the structural integrity of Ni-rich layered oxide materials after synthesis, but additionally the chosen storage methods.[17] $LiNiO_2$ and other Ni-rich layered oxides are much more unstable than Co analogs due to the magnetic frustration of Ni^{3+} compared to Co^{3+}.[91] This leads to enhanced surface degradation in Ni-rich layered oxide materials.

Residual lithium species are common to alkali metal containing layered oxide materials. In most cases, the surface of Ni-rich layered oxides contains LiOH and Li_2CO_3, as well as active oxygen species and Ni reduction.[92,93] Researchers report that residual lithium species negatively impact the interfacial chemical and electrochemical reactions with typical liquid-based electrolytes, crucially deteriorating battery performance.[94,95] To study how atmospheric conditions influence the stability of Ni-rich layered oxides, particularly $LiNiO_2$, XPS was employed to determine the surface components (**Figure 13**).

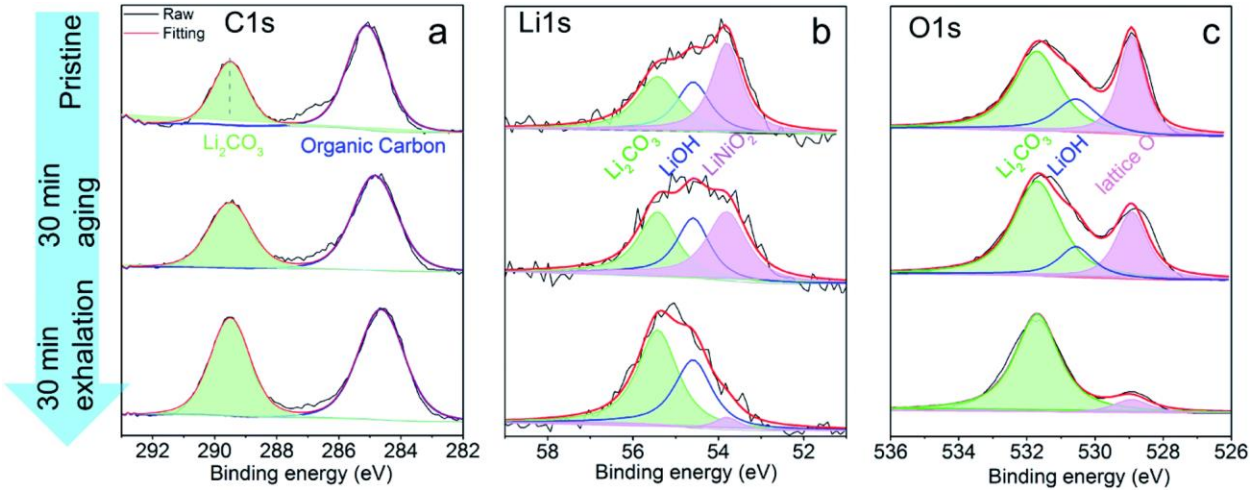

FIGURE 13: XPS spectra for $LiNiO_2$ samples at the pristine, 30 min aging, and 30 min exhalation conditions. The **A)** C 1s spectra is deconvoluted into Li_2CO_3 and organic carbon (adventitious carbon), **B)** Li 1s spectra deconvoluted into Li_2CO_3, LiOH and $LiNiO_2$, and **C)** O 1s spectra deconvoluted into Li_2CO_3, LiOH, and lattice oxygen associated with Li-O and Ni-O. [Taken from Reference[17]]

By deconvoluting the XPS peaks for each of the three spectra, C 1s, Li 1s, and O 1s, a comparison of the lithium residual species can be compared. Upon analyzing the C 1s spectra (**Figure 13A**) the organic carbon and inorganic carbon species are found at 288 eV and 289 eV, respectively. Organic carbon species typically derive from adventitious carbonaceous species, whereas inorganic carbon is largely associated with Li_2CO_3. The peak areas for each of the three samples are associated with ~ 34.48%, 39.62%, and 43.48% for the pristine, 30 min aging, and 30 min exhalation samples, respectively. The Li 1s spectra (**Figure 13B**) includes the deconvolution of Li of $LiNiO_2$, as well as LiOH and Li_2CO_3. The peaks are deconvoluted to ~ 58.73%, 60.56%, and 95.16% for the pristine, 30 min aging, and 30 min exhalation samples, respectively. Lastly, the O 1 spectra (**Figure 13C**) illustrates the deconvolution for Li_2CO_3 and LiOH to be 66.3%, 72.3%, and 90.8%, respectively. Finally, the lattice oxygen species is included for Li-O and Ni-O.[96] This study corroborates previous studies that suggested surface chemical bonding and structure of NMC and other Ni-rich layered oxide materials are directly influenced by CO_2, H_2O,

O_2, and other reactive glove box gases.[97,98,99] The listed gases react with layered oxide materials, extracting Li from the lattice generating LiOH and/or Li_2CO_3 and oxygen vacancies.

Surface reactivity and residual lithium species negatively impact specific capacity and Coulombic efficiency. Upon cycling the $LiNiO_2$ cathode material after being stored under each of the 3 conditions, the fresh material possessed the highest initial specific capacity, followed by storage in the glovebox under Ar for 2 weeks. The least performing material was stored in the drybox for 2 weeks. The Coulombic efficiency followed the same trend (**Figure 14A**). The capacity retention for each material was determined by cycling a coin cell from 2.5 – 44.V vs Li/Li^+ at C/3 at 22 ºC. Three cells were averages to quantify the capacity retention as 68.7%, 73.7%, and 70.1% for the fresh, Ar-2 weeks, and drybox-2 weeks samples, respectively (**Figure 14B**). To determine the electronic perturbations, the O K-edge pre-edge features are analyzed to determine the TM*3d*-O*2p* orbital hybridization changes (**Figure 14C**). The soft XAS data illustrates that the fresh material has more Ni^{3+} content and decreased amounts of Li_2CO_3 in comparison to the material that was analyzed after being stored for 2 weeks in the drybox. This data further corroborates that there are electronic influences that are perturbed after $LiNiO_2$ interacts with gases under ambient conditions.

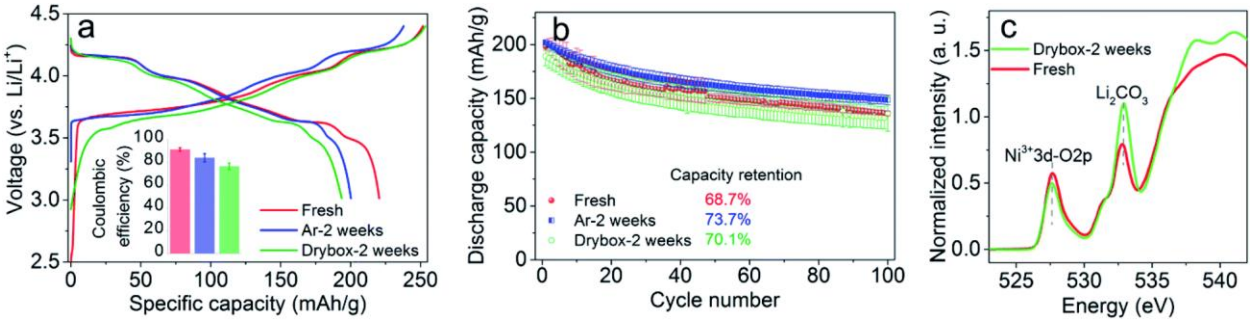

FIGURE 14: $LiNiO_2$ cathode in the pristine state and after being stored in the Ar-filled glovebox and drybox for 2 weeks. The cycling data **A)** illustrates the charge/discharge profiles at C/10, with the initial Coulombic efficiency included in the inset. **B)** The cycling stability is illustrated for 2.5-4.4V vs Li/Li^+ at C/3 at 22 ºC, with three individual cells averaged for the associated error. **C)** Soft XAS O K-edge spectra obtained in the TEY mode highlights the distinct peak intensity located at ~ 534 eV for the fresh pristine sample and the sample stored in the drybox for 2 weeks. [Taken from Reference[17]]

Herein this dissertation, proper storage and handling procedures are utilized to ensure that the analytical techniques employed provide reliable, accurate data. In ***Section 3.2*** background context surrounding C-X bond activation is described. This is necessary to develop a rational understanding of the model reaction chosen to explore the chemistries associated with Ni-rich layered oxide materials.

1.3 Strategies to Reduce Cathode – Electrolyte Interfacial Reactions

Cathode-electrolyte interfacial reactions are undesired in most cases. There are various strategies researchers have employed to suppress side reactions that degrade the cathode material. Strategies include material modifications such as surface coatings, the inclusion of metal dopants to enhance structural robustness, and pre-formed passivation layers. ***Section 1.3*** addresses how metal dopants and surface coating strategies reduce side reactions and improve the structural integrity of Ni-rich layered oxide materials.

1.3.1 Metal Dopants and Coatings to Improve Oxide Cathode Integrity

Metal dopants, specifically those that have a high affinity for oxygen, have been used to improve the structural integrity of layered Ni-rich oxide materials. Kong et. al. calculated the oxygen vacancy formation as well as the bonding orbital energy for different transitions metals and oxygen.[55] Cations that increased the iconicity of metal-oxygen bonding, such as Mn, Co, Ti, and Al, will increase the oxygen binding strength. This increases the oxygen vacancy formation energy. Iron (Fe) has also been used as a dopant[100], stabilizing high spin tetravalent states of Ni during charging.

Dual dopants have been utilized to enhance the structural robustness of Ni-rich layered oxide materials. When coupling Fe and Co as a dopant to Ni-rich layered oxide materials, Ni^{3+} and Fe^{3+} both become oxidized, improving the structural robustness of the cathode at high states of charge.[101] Additionally, Na-Al dual substitution has been used to improve the layered material of Co-free, Ni-rich layered oxide material.[102] Yang and coworkers have illustrated how dopants to the lattice of Ni-rich layered oxides, such as Mg/Ti-$LiNiO_2$, is strategically synthesized in which there is a Ti concentration continuum from the surface to bulk.[103] This dopant strategy is unique because Ti, a superior dopant because of the strong ionicity of Ti-O, mitigates some of the structural fragility challenges associated with oxygen evolution. When Mg/Mn-$LiNiO_2$ is used as a no-cobalt cathode material, the dopants smooth the charging plateaus associated with structural irreversibility mechanisms associated with cation mixing and oxygen release.[104]

Dopant strategies are extremely important in commercializing high energy density Ni-rich layered oxide materials that have >80% Ni content. While dopants are one pathway to enhance the structural stability of $LiNiO_2$ and other Ni-rich layered materials, coating strategies are also extremely important.

Coating can be utilized to effectively modify the surface and bulk of oxide cathode materials for improved structural integrity.[105–107] Surface coatings can minimize undesired cathode-electrolyte interfacial side reactions. Coating materials infiltrate the grain boundaries and limit physical contact between electrolytic species and reactive oxide cathode primary particles. When the electrolyte intercalates into the grain boundaries, it leads to chemomechanical breakdown and capacity fading. One method that coatings improve the surface structural stability is by suppressing lattice oxygen loss. By suppressing lattice oxygen loss, chemomechanical stress is decreased, as well as the number of electrolyte decomposition pathways, improving the overall Coulombic efficiency. Additionally, coatings decrease transition metal dissolution by inhibiting oxide surface interactions with the Li-salt found in the electrolyte.[108]

In developing a superior coating material for fragile oxide cathode materials, there are a few components to consider. While surface coatings provide a physical barrier to eliminate cathode-electrolyte interfacial reactions, it is important that they do not hinder Li^+ transport kinetics. If the coating decreases Li^+ transport, specific capacity fading will be evident. One strategy is to utilize lithium-containing metal oxides as a coating film for high Li^+ conductivity.[109–112] Metal oxides[113], metal fluorides[114], and metal phosphates[115,116] can each be used as suitable coating materials.

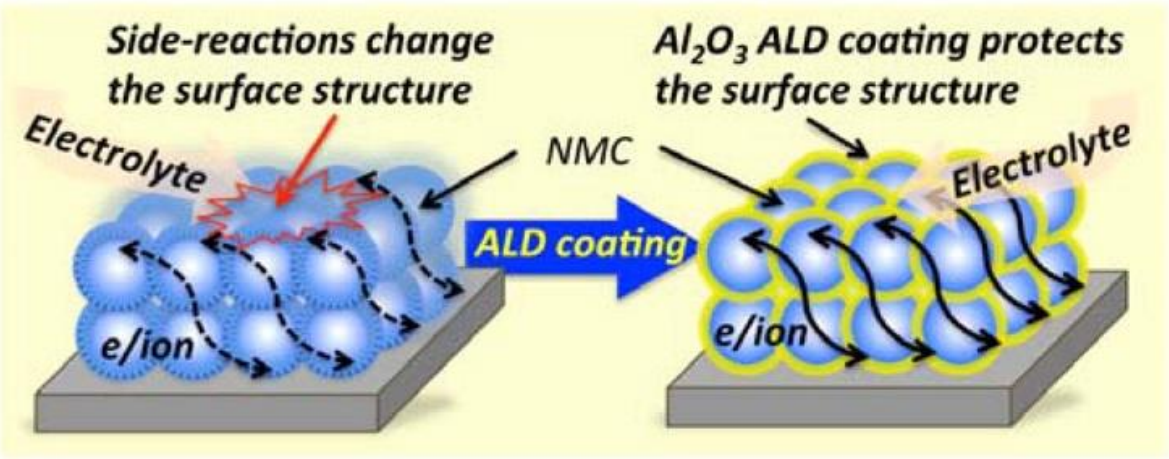

FIGURE 15: Al_2O_3 coating on $LiNi_xMn_yCo_zO_2$ (NMC) to eliminate side reactions that increase structural instability, leading to capacity fading and decreased Coulombic efficiency. [Taken from Reference[117]]

A commonly employed metal oxide coating is Al_2O_3.[118] Al_2O_3 is a well-studied coating material and much of the attention is due to the large band gap, its ability to transport Li^+ without hindrance, and retain electronic stability post-coating.[108,117] **Figure 15** highlights an example of an Al_2O_3 coating on NMC particles and how it protects the surface structure of the oxide material.

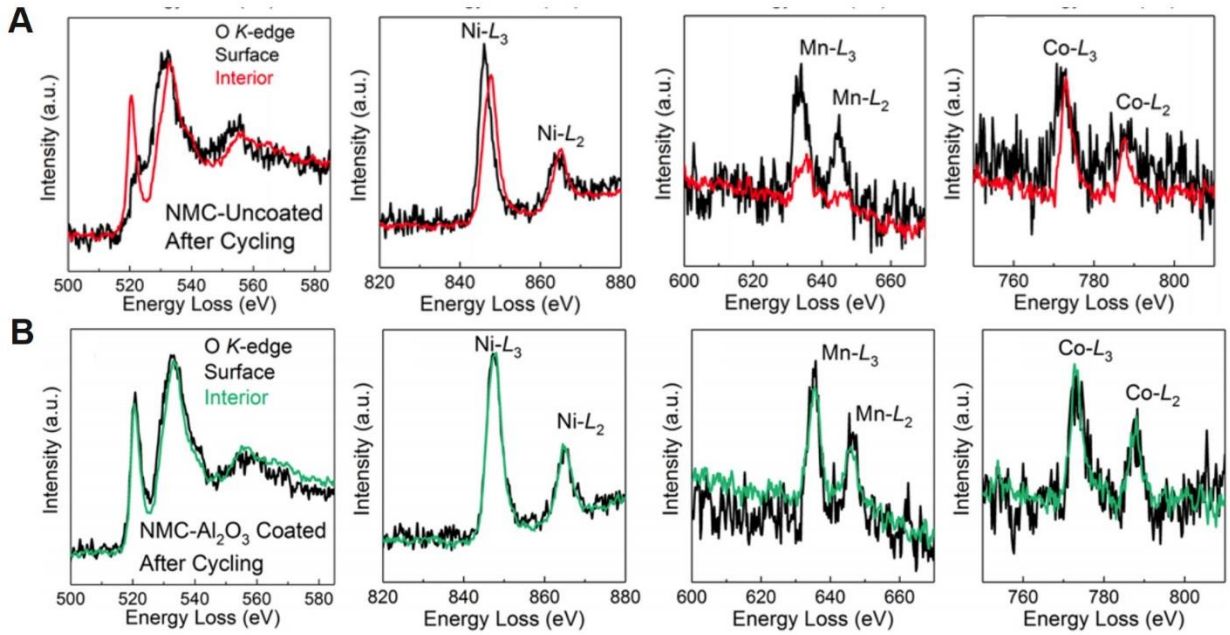

FIGURE 16: X-ray absorption spectroscopy (XAS) of the **A)** NMC uncoated and **B)** NMC Al_2O_3-coated Ni-, Mn-, and Co-L edges. The uncoated material illustrates transition metal reduction at the surface most of the material due to interfacial reactions. The Al_2O_3-coated NMC material shows no transition metal oxidation state change at the surface compared to the interior. [Taken from Reference[108]]

The soft X-ray absorption spectroscopy (XAS) in **Figure 16**, illustrates that prior to coating there is transition metal reduction at the surface of the material compared to the bulk. This is shown by the shift in L edge energy (**Figure 16A**). In comparing the NMC uncoated material to an Al_2O_3-coated material, it is obvious that the oxidation state of each transition metal is preserved (**Figure 16B**). Transition metal reduction is indicative of structural disordering and electronic perturbations. The O K-edge pre-edge features provide information regarding the TM*3d*-O*2p* orbital hybridization. The surface of the material has a decreased peak intensity for Ni^{3+}, compared to the bulk electronic structure. While other metal oxides are utilized in surface coating strategies, Al_2O_3 may have advantages compared to some other metal oxide materials because Al serves as a key dopant in NCA[119–121] to provide enhanced structural stability.

Chapter 1 discusses all of the fundamental chemistry required to understand future chapters detailed in the technical chapters (**Chapters 3-5**) of this dissertation.

CHAPTER 2: ANALYTICAL METHODS

2.1 Introduction

A plethora of analytical techniques are employed to obtain the technical data reported in this dissertation. X-ray techniques, electron microscopy, as well as electrochemical and quantification methods are described in detail. **Chapter 2** highlights the working principles of the analytical methods used to obtain the data required to make conclusions for novelties described in this dissertation. Quantification methods, such as gas chromatography (GC) coupled with flame ionization detector (FID) and mass spectrometry (MS) are discussed in ***Section 2.2***. ***Section 2.3*** will discuss X-ray techniques, including X-ray absorption spectroscopy (XAS), X-ray absorption near-edge spectroscopy (XANES), extended X-ray absorption fine structure (EXAFS), X-ray diffraction (XRD), and X-ray photoelectron spectroscopy (XPS). Lastly, electrochemical testing methods will be explained in greater detail in ***Section 2.4***, highlighting the benefits for the projects described herein this dissertation.

2.2 Quantification using Gas Chromatography

Chromatography is a separation technique made up of a stationary phase and a mobile phase.[122] In gas chromatography, the mobile phase is gas, continuously flowing through the column. The column is typically glass or metal and is considered to be the stationary phase. Gas chromatography allows a carrier gas (mobile phase) to carry a vaporized sample through the

column (stationary phase). During that process an equilibrium occurs between the analyte and the stationary phase, separating them for detection, but most importantly quantification. The signal from the detector provides a chromatogram which can be used to for quantification purposes based on the kinetic processes that occur during the partitioning between the analyte and the stationary phase.

The key advantages of gas chromatography are fast analysis time, efficient with high resolution, sensitive with detection limits of ppm and ppb, small sample size required, and inexpensive.[122] Another advantage is that GC can be easily coupled with detectors such as mass spectrometers (***Section 2.2.1***) and flame ionization detectors (***Section 2.2.2***). In determining characteristics of the analyte, key components are the retention time (t_R) and the column flow rate (F_c). In GC experiments, the column flow rate is typically constant throughout the experiment. This allows one to calculate the retention volume using the following equation: $V_R = t_R \times F_c$.

Disadvantages to GC are that the sample must be volatile and not be extremely large quantities for analysis. Additionally, to determine the true identity of various molecules within an analyte sample, spectroscopy must be used for confirmation. Herein this dissertation, gas chromatography was employed for reactant conversion quantification from the detector provides a chromatogram which can be used to elucidate the quantification based on the kinetic processes that occur during the partitioning between the analyte and the stationary phase.

The key advantages of gas chromatography are fast analysis time, efficient with high resolution, sensitive with detection limits of ppm and ppb, small sample size required, and inexpensive.[122] Another advantage is that GC can be easily coupled with detectors such as mass spectrometers (***Section 2.2.1***) and flame ionization detectors (***Section 2.2.2***). In determining characteristics of the analyte, key components are the retention time (t_R) and the column flow rate

(F_c). In GC experiments, the column flow rate is typically constant throughout the experiment. This allows one to calculate the retention volume using the following equation: $V_R = t_R \times F_c$.

Disadvantages to GC are that the sample must be volatile and not be extremely large quantities for analysis. Additionally, to determine the true identity of various molecules within an analyte sample, spectroscopy must be used for confirmation. Herein this dissertation, gas chromatography was employed for reactant conversion quantification.

2.2.1 Gas Chromatography – Mass Spectrometry (GC-MS)

Mass spectrometry is commonly coupled with gas chromatography. Mass spectrometry (MS) is used to generate ions from compounds, followed by separating them by their mass-to-charge ratio (m/z). This allows for MS to qualitatively and quantitatively determine the m/z and abundance of an analyte. There are three major components of a mass spectrometer including the ion source, mass analyzer, and detector. Each of these components are operated under high vacuum conditions.

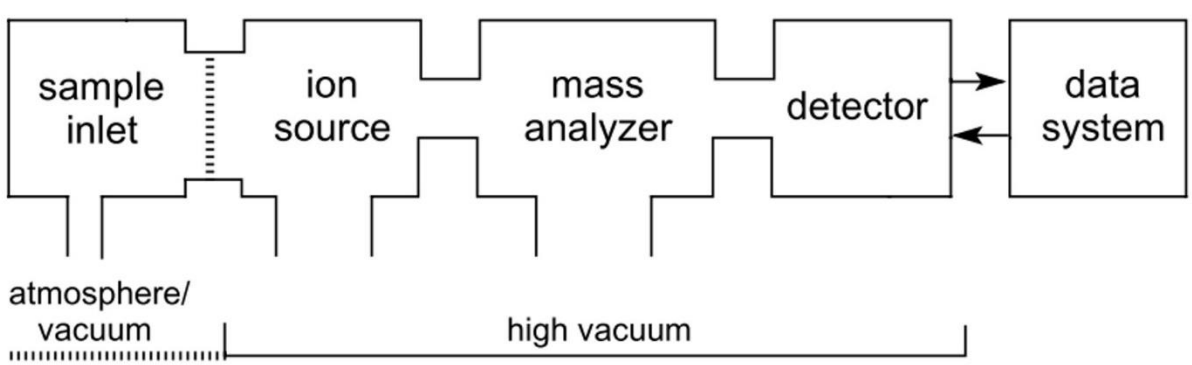

FIGURE 17: Schematic of a mass spectrometer, illustrating that the sample inlet is under atmospheric conditions. Upon the sample reaching the ion source, mass analyzer, and detector, the system is under high vacuum. A mass spectrum is collected by the data system for analysis of the analyte components. [Taken from Reference[123]]

As illustrated in **Figure 17**, the sample is injected into the sample inlet under atmospheric conditions. Following sample injection, the sample is under vacuum and reaches the ion source. The ion source generates the m/z ratio that can be further analyzed by the mass analyzer. The detector provides a representation of the signal intensity versus the m/z ratio. The data system will provide information that can be normalized for one to determine the base peak, also referred to as the molecular ion peak. This is followed by fragment ion peaks at lower m/z ratios that occur due to fragmentation during ionization. The m/z ratio, peak intensity, shape, and width can all be utilized to quantify analytes with high accuracy and resolution.

2.2.2 Gas Chromatography – Flame Ionization Detector (GC-FID)

Flame ionization detections (FID) is the most commonly employed in gas chromatography than any other analytical separation method since its introduction in 1958.[124] FID works on the principle that upon burning carbon compounds, ions are produced. These ions are typically eluted from the GC column. Upon reaching the hydrogen flame of the FID detector, current passes between two electrodes found near the flame providing a signal that can be used for qualitative and quantitative purposes. One of the advantages of FID is that there is a very low noise level, high sensitivity, and very consistent regardless of the other factors required for instrumentation. Key factors include the detector temperature, as well as hydrogen and carrier gas flow-rates.

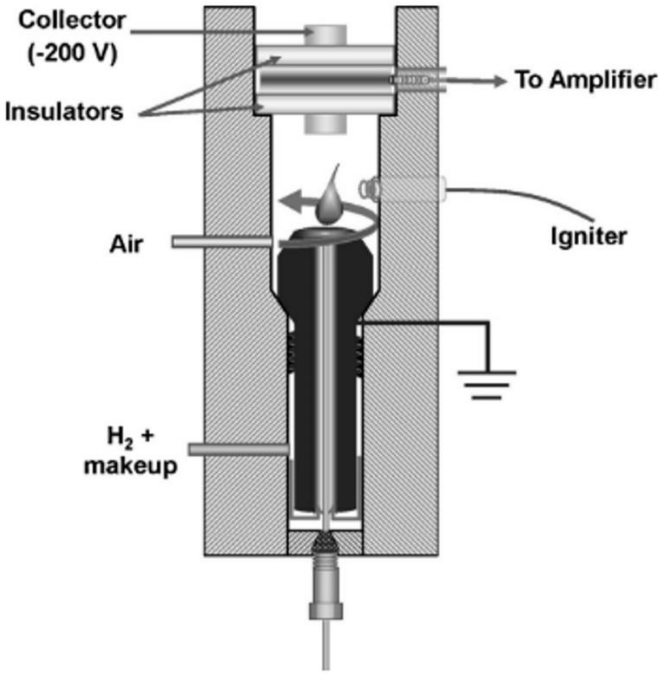

FIGURE 18: Flame ionization detector schematic, illustrating the major components required for operation. [Taken from Reference[125]]

Figure 18 illustrates the schematic for the FID. The detector responds to the combustion of organic compounds. Typically, this combustion occurs under a hydrogen-air flame. The cylindrical collector electrode found near the flame allows for charged particles between 200-300 V to be collection for analysis. For rapid determination of organic molecules, coupling GC-FID proves to be an effective way to quantify conversion.

2.3 X-ray Techniques

This dissertation greatly utilizes X-ray techniques, including X-ray photoelectron spectroscopy (XPS), X-ray absorption spectroscopy (XAS), and X-ray diffraction (XRD). Each of these techniques provides unique information to characterize materials. XPS is a surface sensitive method that describes changes in local chemical bonding interactions, whereas XAS

provides orbital occupancy details of a system. Together, they can cooperatively illustrate how electrons and bonding arrangements exist in materials. When coupled with XRD, a bulk structure technique, a physical depiction of the system can be provided to elucidate mechanisms, electron and oxygen transfer pathways, as well as an improved understanding of decoupling the chemistry at the surface and bulk of these systems. The following sub-sections of ***Section 2.3*** will include a discussion on the working principles of the X-ray techniques used throughout this dissertation.

2.3.1 X-ray Photoelectron Spectroscopy (XPS)

X-ray photoelectron spectroscopy, often abbreviated as XPS, is a common tool used to provide elemental analysis for the surface of materials. Because of its working principles, its greatest advantage is being able to determine the local chemical environment of an atom. This advantage is useful when determine the how local chemical bonding environments have been perturbed in a system after a chemical reaction is complete.

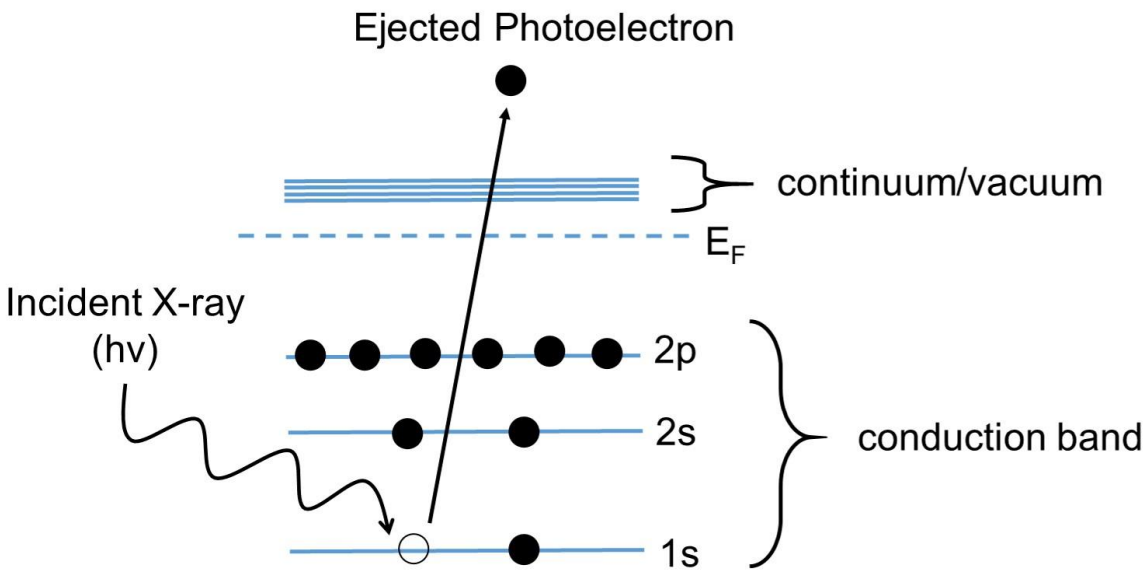

FIGURE 19: XPS working principle, illustrating the excitation of a core level electron by an incident X-ray into the continuum as an ejected photoelectron. The binding energy of the photoelectron is then experimentally determined and used to examine local chemical environment of an atom. [Modified from Reference[126]]

As shown in **Figure 19,** XPS operates by have an X-ray source generate a core hole by ejecting a core level electron into the continuum. The ejected electron is referred to as a photoelectron. The energy of the ejected photoelectron is then analyzed by the electron spectrometer, providing a graph of intensity expressed as counts or counts per section versus the electron energy. Because XPS characterization surfaces using photoelectrons, it is typically operated under ultrahigh vacuum (UHV) conditions.

The parameters of an XPS experiment include the photon energy ($h\nu$), the kinetic energy of the electron (E_K), and the work function of the spectrometer (ϕ). The kinetic energy is the experimental quantity measure by the spectrometer and is dependent on the energy of the X-ray source. Each electron is specifically identified by its parent element and atomic energy level by calculating the binding energy (E_B). The parameters can be used to calculate the binding energy

using the following equation: $E_B = h\nu - E_K - \phi$. It is important to note that although the binding energy is independent of the X-ray photon energy.

X-ray notation is key in understanding how to interpret the data obtained from XPS. XPS uses soft X-rays, commonly Al Kα X-rays. Upon measuring the energy of the photoelectrons emitted, quantum numbers are utilized to formally describe which electrons are involved in the observed transitions. The principle quantum number, *n*, the orbital angular momentum, *l*, and the spin angular momentum, *s*, can help determine the orbital location. The quantum number as defined by nl_j, where *j* is the sum of |l+s| can provide notation needed to elucidate XPS spectra. A *p* orbital can have a j value of ½ (l-s) or 3/2 (l+s), whereas *d* orbitals can have either 3/2 or 5/2. Doublets formed in the spectra are caused by spin orbit coupling due to degeneracies. Values of *l* are typically 0, 1, 2, and 3, with corresponding orbital notation of s, p, d, and f, respectively. These typical orbitals are then translated into X-ray notation, common amongst many other X-ray analytical techniques. When n = 1, 2, or 3, the X-ray notation is K, L, and M, respectively. **Figure 20** below provides a detailed description of the relationship between quantum numbers, spectroscopy notation, and X-ray notation.

Quantum numbers				
n	l	s	Spectroscopy notation	X-ray notation
1	0	±½	$1s_{1/2}$[a]	K
2	0	±½	$2s_{1/2}$[a]	L_1
2	1	+½	$2p_{1/2}$	L_2
2	1	±½	$2p_{3/2}$	L_3
3	0	±½	$3s_{1/2}$[a]	M_1
3	1	±½	$3p_{1/2}$	M_2
3	1	±½	$3p_{3/2}$	M_3
3	2	±½	$3d_{3/2}$	M_4
3	2	±½	$3d_{5/2}$	M_5
				etc.

[a] usually identified as 1s, 2s, 3s, in XPS, the subscript is omitted.

FIGURE 20: Table of the X-ray notation for a selected number of quantum numbers with their associated spectroscopy notion included. [Taken from Reference[126]]

XPS has been commonly employed as a materials characterization method for applications in surface chemistry, including identifying chemistries at interfaces. In many cases, the physical and chemical composition of these surface and the interactions that occur can be elucidated using XPS. Herein this dissertation, we utilize XPS to provide an understanding of the surface chemistry of layered oxide materials and the local chemical bonding changes they undergo when probed with small molecules, such as benzyl alcohol and *p*-nitrophenol. Layered oxide materials possess different chemistry at surface-most compared to the bulk, complicating experimental design in understanding the interfacial chemistries that exist in this class of materials. XPS has shown to be advantageous for understanding the surface chemistry of layered oxides[127–130], as well as complicated liquid/solid interfaces[131], making it an ideal X-ray technique to employ in this dissertation.

2.3.2 X-ray Absorption Spectroscopy (XAS)

The electromagnetic spectrum provides a broad range of the types of electromagnetic radiation. As shown in **Figure 21**, X-rays are split into two different categories – soft and hard.

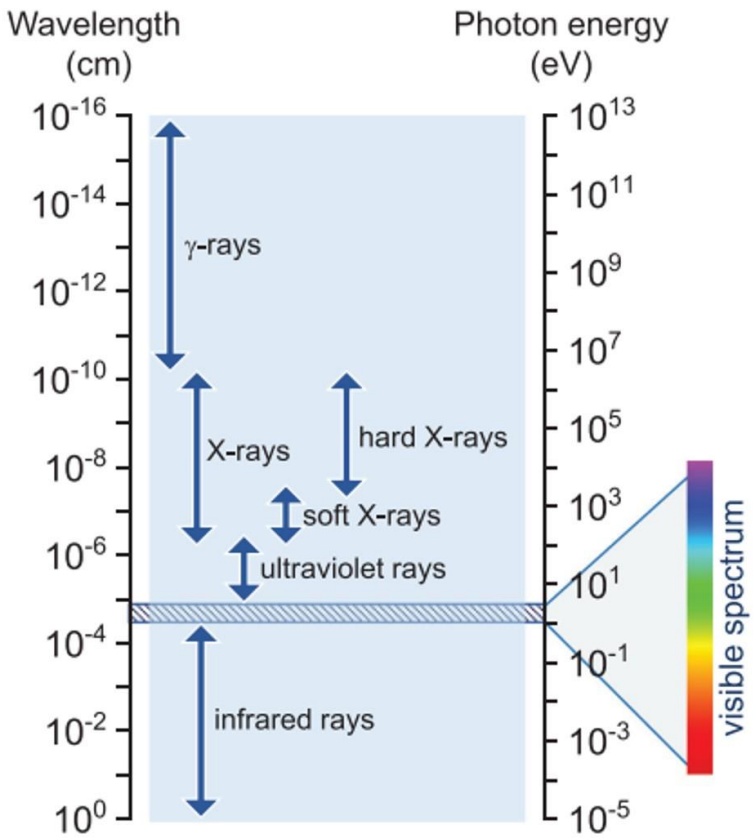

FIGURE 21: Electromagnetic spectrum, illustrating the energy associated with infrared (IR) rays, ultraviolet (UV) rays, X-rays, and gamma rays. X-rays, used to excited electrons in XAS, are commonly divided into hard and soft X-rays, illustrated in the depiction. [Taken from Reference[132]]

X-ray energy is scanned through the binding energy, giving rise to an abrupt increase in the cross-section. This cross section gives rise to the absorption edge, representing the core electron binding energy. The X-ray notation mentioned in ***Section 2.3.1*** is the same for XAS. The amount of electron excitation is directly related to the energy of the incident X-ray beam. Soft X-rays have

less energy and therefore provide orbital occupancy information about the surface-most of the material. Hard X-rays have higher energy, providing orbital occupancy of the bulk of the material.

Soft XAS provides the oxidation state of atoms. In this dissertation, the major elements analyzed by XAS are Ni, Mn, Co, and O. Soft XAS allows for an examination of the transition metal L-edge, particularly the L_3 and L_2-edge, associated with excitation of an electron from a *p*- to *d*-orbital. L_3 edge is normally used to determine the relative transition metal oxide state because the L_2-edge is complicated by the spin-orbit coupling energy when a *p* electron undergoes excitation.[133,134] For oxygen, soft XAS is used to examine the K-edge or excitation from an *s*- to *p*-orbital.

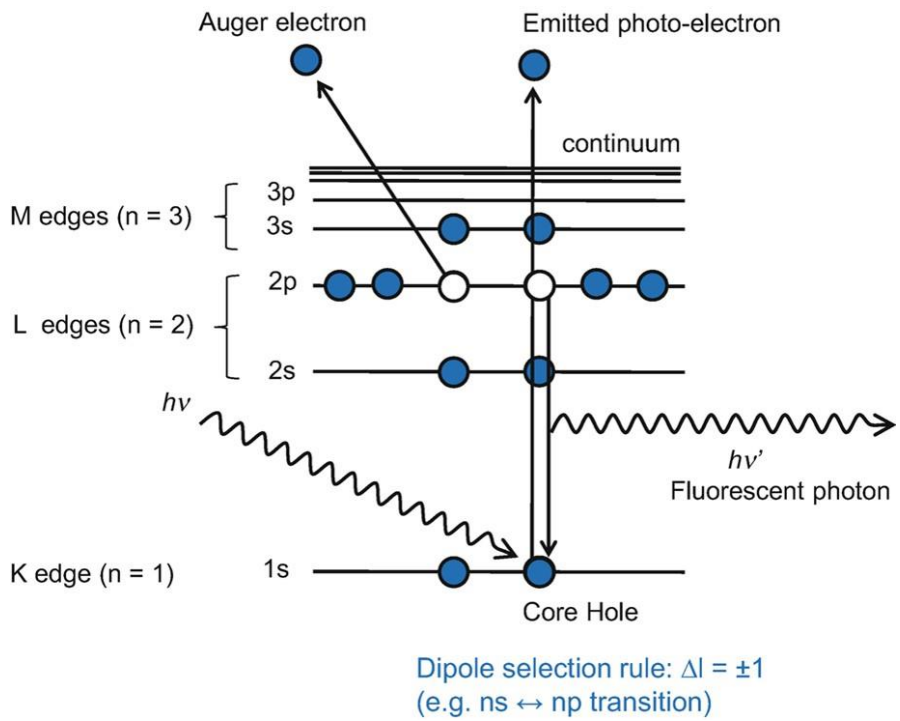

FIGURE 22: X-ray absorption spectroscopy (XAS) working principles, illustrating the various types of electrons analyzed by the detector. Auger electron yield (AEY) mode collects auger electrons, total electron yield (TEY) mode is analyzed by ejected photoelectrons, and fluorescence yield (FY) mode is analyzed by the fluorescent energy generated by a core hold being filled by a high lying electron. [Taken from Reference[135]]

When performing soft XAS, there are three different detection modes (**Figure 22**). The total electron yield (TEY) mode is commonly used and provides information regarding the surface layer up to about 5-10 nm in depth. TEY mode detects photoelectrons generated via X-ray excitation of a core electron into the continuum, as well as auger electrons. Auger electrons are ejected into the continuum when there is an excess amount of energy during the excitation causing a higher lying electron to also be ejected. The combination of these two types of electrons make TEY mode an appropriate detection mode when surface-most orbital occupancy is desired. In auger electron yield mode (AEY), only auger electrons are detected, leading to a much lower signal to noise ratio. The energy of auger electrons are directly related to the mean free path, suggesting that it must have enough energy to be detected. Lastly is fluorescence yield (FY) mode. FY mode detection can probe quite a bit deeper into the bulk of the material, but not as deep as a hard X-ray. Fluorescent photons are generated when a photoelectron is ejected, followed by a higher lying electron losing energy and filling the core hole that was created. The energy lost is fluorescence and can be detected as such by the spectrometer. In this dissertation, surface chemistry and interfacial reactions were analyzed; therefore, the soft XAS results reported were in TEY mode.

Hard XAS, sometimes referred to as X-ray absorption near-edge spectroscopy (XANES), provides identification of the element as well as the oxidation state. Because hard X-rays possess more energy, they can penetrate the sample into the bulk. The oscillations after the edge features can extend for up to 1 keV and the information is considered to be the extended X-ray absorption fine structure (EXAFS). **Figure 23** below illustrates the Ni K-edge for $LiNiO_2$, highlighting the regions associated with XANES and EXAFS at lower and higher energies, respectively.

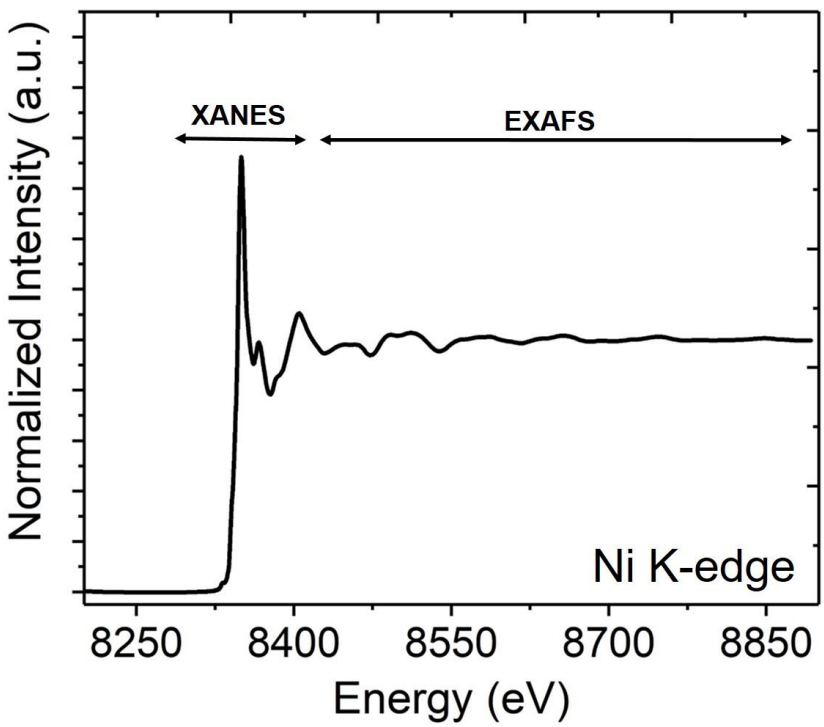

FIGURE 23: XANES and EXAFS region for Ni K-edge of $LiNiO_2$. The energy denotes the element identity, while XANES can provide the orbital occupancy of the bulk material. The EXAFS features can be further used to determine structural distortions in the material due to variances in orbital occupancy. [Taken from Reference[133]]

The use of XAS has become more popular and has been denoted as a valuable analytical tool after the development of synchrotron radiation. Synchrotron radiation allows for electron storage rings to provide extremely intense X-ray sources by the utilization of a magnetic field.[133] Synchrotron XAS experiments have been readily employed in studying orbital occupancy and structural distortions in layered oxide materials. Herein this dissertation, synchrotron XAS was utilized to decouple surface and bulk chemistries in the studied class of materials.

2.3.3 X-ray Diffraction (XRD)

Since Max von Laue discovered that crystals diffract X-rays in 1912, X-ray diffraction is the go-to analytical method for investigating the fine structure of crystalline materials.[136] In 1914, von Laue received the Nobel Prize for his discovery of the diffraction of X-rays by crystals. The father son duo, William Henry and William Lawrence Bragg, further catapulted X-ray diffraction into a mainstream characterization method by confirmed von Laue's experimental methods. Due to the contribution of the father-son duo, they were awarded the Nobel Prize in 1915 for their services in the analysis of crystal structure by means of X-rays.[137] While in the early years of use XRD largely was developed to determine crystal structure, today the analytical method is applied to determine the structure to solve complex problems in chemical analysis, phase transformation, crystal orientation, and polycrystalline aggregates.

A continuous range of wavelengths are employed in the Laue method. This allows for the determination of a set of planes that will diffract at a particular angle, such that the Bragg law is fulfilled. The Bragg law is represented by the equation $n\lambda = 2d \sin\theta$. The Bragg law encompasses the three Laue equations, which represent the crystallographic planes identifiable by *hkl*. In the Laue pattern, an X-ray beam passes through the slit in the direction of the *c* axis, providing details regarding crystallography symmetry, axial ratio, and crystal orientation.[138] Powder XRD is common when studying layered metal oxide materials, as it allows for monochromatic radiation to be used on a large amount of small crystals with random orientation. When the X-ray beam contacts the sample, there is diffraction when the Bragg law is satisfied. Because the sample is totally random, each plane with d-spacing for *hkl* will form a cone of half apex angle $2\theta_{hkl}$. The powder XRD pattern is derived from the intersection of these cones, providing the crystalline structure. **Figure 24** provides a schematic of the working principles of XRD.

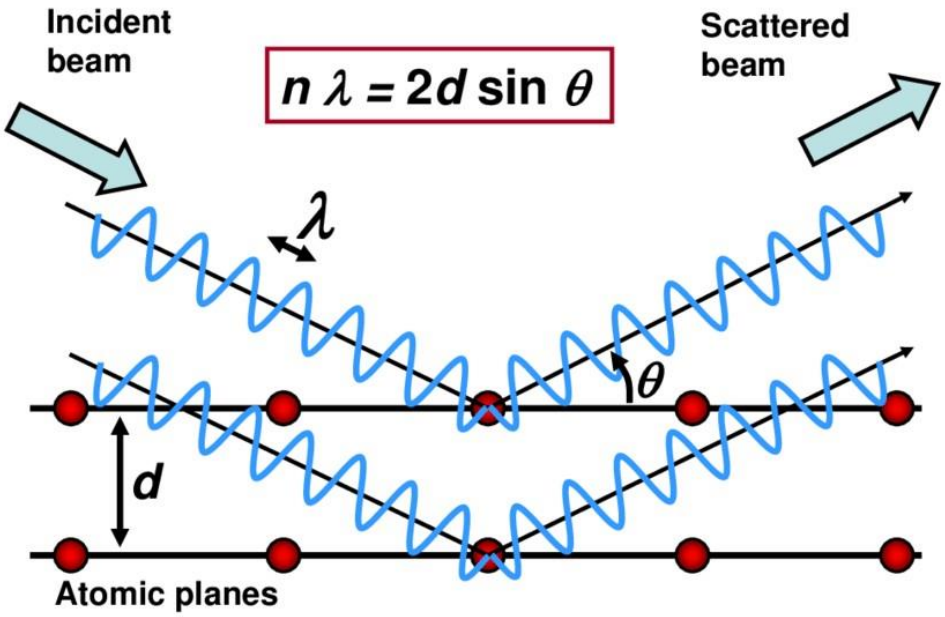

FIGURE 24: Working principles for X-ray diffraction, illustrating the path of the X-ray incident and scattered beam. The angle corresponds to the atomic plane that fulfills the Bragg law, $n\lambda = 2d \sin\theta$. [Taken from Reference[139]]

XRD is key in understanding the bulk structure of layered oxide materials. There are many structural changes in layered oxide cathode materials, which can be quantified using XRD patterns.[140–142] Herein this dissertation, XRD proved to be useful in obtaining the technical data and providing useful conclusions.

2.4 Electron Microscopy

Since the 1920s, electron optics have existed to provide investigative information to describe the topography, morphology, structure, and elemental composition of various inorganic samples. Electron microscopy is commonly employed due to its advantageous high resolving

power that provides the structure of materials. Louis de Broglie associated wavelengths with the movement of electrons.[143] Electrons have a wavelength roughly 100,000 times shorter than visible light photons, enhancing the high resolution associated with electron microscopy analytical methods.

Battery research typically exploits the benefits of electron microscopy to determine the structural, morphological and elemental composition of cathode materials. This dissertation highlights a few electron microscopy techniques, including scanning electron microscopy (SEM), transmission electron microscopy (TEM), and scanning transmission electron microscopy (STEM). A detailed discussion on each electron microscopy analytical method is included in the sub-sections of ***Section 2.4***.

2.4.1 Scanning Electron Microscopy

Scanning electron microscopy (SEM) is commonly used to determine the topography and elemental composition of a sample. In SEM, an electron gun at the top of a column produces an electron beam. The magnetic lens, first discovered by German physicist Hans Busch in 1927, focuses the electron beam found within the column. This electron beam rasters over the sample, generating a signal caused by interactions of the electron beam with the sample. The beam penetrates the sample to a variety of depths, depending on the accelerating voltage and sample density.[144] Two different types of electrons are generated when the beam contacts the sample – secondary and backscattered electrons.

Secondary electrons provide topographical information. They are low energy electrons and are typically used for the majority of imaging for SEM analysis. Secondary electrons are found a few nanometers from the electron beam. These electrons correlated to the high-resolution image that yield the local fine features. Disadvantages to using secondary electrons for imaging

is that there can be decreased gun brightness, increased chromatic aberration and diffraction contribution at the aperture, contamination buildup, and electromagnetic interference effects. The backscattered electrons are affected by atomic number and phase differences. Heavier atoms scatter more electrons making them brighter in the SEM image.

The SEM chamber is under high vacuum so the samples analyzed are dry powder samples. To obtain the appropriate resolution during imaging, an appropriate balance between the spot size must be determined to reveal the finer details of the sample without increasing the noise in the image. The spot size is controlled with the condenser lens, the first lens found beneath the electron gun. The major advantages of SEM are associated with the magnification and resolution, as well as the easy to interpret images. SEM is very useful in providing information in understanding battery cathode materials. This dissertation utilized SEM as an analytical method to illustrate the material morphology.

2.4.2 Transmission Electron Microscopy (TEM)

Although the first electron microscopy was built in 1932, transmission electron microscopy (TEM) did not become widespread until the 1950s and 1960s.[145] The working principles for TEM are similar to that of other electron microscopy images. A beam of electrons is transmitted through the sample which means the sample must be very thin. The signal is generated from the interaction of the electron beam with the sample. The sample must be thinner than 100 nm for the electron beam to penetrate the sample and be transmitted. TEM requires a higher vacuum and voltage in comparison to SEM. TEM provides analytical information to determine the 1) phases and crystal structure types, 2) crystal symmetry and space group, 3) orientation relationships between phases, 4) growth directions and interface coherency, 5) identifying defects, and 6) ordering behavior of crystal structures and site occupancy preferences.

Scanning transmission electron microscopy (STEM) is slightly different from TEM in that a small probe can be focused on a thin sample to compute the image. In this technique a scanned electron beam is used in a raster pattern. The beam electrons and the sample atoms interact and generate the signal. Some of the major advantages over SEM and TEM include improved spatial resolution and Z-contrast in STEM. TEM and STEM have both been utilized to analyze battery cathode materials.[146–149] Herein this dissertation, TEM and STEM are discussed.

CHAPTER 3: EXPLORING SURFACE RECONSTRUCTION IN NMC622 VIA BENZYL ALCOHOL OXIDATION: A CATALYSIS APPROACH

3.1 Introduction: Chemistries that Promote Structural Fragility in NMC Materials

Cathode metrics influence multiple facets of battery performance including energy density, cycle life, and safety. Layered transition metal oxides continue to dominate as frontier lithium-ion battery cathode materials.[66] $LiCoO_2$ (LCO) has superceded the market for consumer electronics since the onset of the commercialization of lithium-ion battery technology.[150,151] While LCO possesses all of the qualities required for superior battery performance such as relatively high theoretical capacity (274 mAh g^{-1}), high discharge voltage, and overall good cycling performance,[152] there has been a migratory trend towards low-Co and Co-free Ni-rich materials due to geopolitical issues surrounding the mining of cobalt. Low-Co and Co-free materials are advantageous due to their reduced cost, minimized toxicity, and increased practical capacity.[153,154,155]

$LiNi_xMn_yCo_zO_2$ (NMC) materials have gained much attention as a lithium battery cathode material because of the transition metal cooperativity that improves its physical properties. In NMC materials, nickel (Ni) generates to higher specific capacities while manganese (Mn) and cobalt (Co) provide increased structural integrity and thermal stability.[156–158] Theoretical specific capacity of cathode materials can be calculated by the equation: $[(F \times n_{Li}) / (MW \times 3600)] \times 1000$ mAh/g. The variables are defined as Faraday's constant (F), which is 96483 C/mol, the moles of Li (n_{Li}), and the molecular weight (MW) of the material. Upon calculating the theoretical specific capacity for LCO and NMC622, the values are ~ 274 mAh/g and ~ 276.5 mAh/g, respectively.

Although the theoretical capacities are similar, Ni-containing materials possess an increased practical capacity due to its ease of Ni oxidation. Nickel has proven to be paramount in the design and innovation strategies toward new classes of cathode materials due to its high specific capacity at relatively low voltages.[159–161] Higher specific capacities at lower voltages is significant because it allows the material to be oxidized while electrolyte decomposition is minimized. Minimizing electrolyte decomposition is advantageous for overall battery performance by decreasing specific capacity fading and increasing Coulombic efficiency.

Although NMC materials are widely studied by researchers, there are many unanswered questions that remain regarding the complex chemistries of this material and its Ni-rich layered oxide analogs. There is a great need to understand how synthetic approaches and electronic modifications in Ni-rich layered oxide materials influences intrinsic properties. Some properties include microcracks between primary particles[39], uncontrollable surface phase changes[30,162,163], transition metal cation dissolution[56,164], and undesired electrolyte decomposition[165,166]. Each of these phenomena cooperatively impact the structural and chemical integrity of layered oxide materials. The sub-sections discussed in **Chapter 3** highlight the technical research completed towards exploring the influences small, organic molecules have on the structural and electronic integrity of $LiNi_{0.6}Mn_{0.2}Co_{0.2}O_2$ (NMC622). Developing a molecular probing strategy is key in understanding the surface chemistry of this class of material.

3.1.1 NMC Cathode Composites – Synthesis Strategies

Developing stable, high energy density cathode materials is a major limiting factor in lithium batteries. Innovative strategies are necessary to improve layered oxide materials. This provides the means to acquire structural and electronic robustness in Ni-rich layered oxide

materials. In doing so, it would minimize capacity fading, decrease undesired, parasitic surface reactions, and improve Li^+ mobility kinetics required for optimal cycling rates and overall performance.

The synthesis of cathode materials prove to be challenging because of lithium off-stoichiometry[167], cation mixing[168,169], and varied surface chemistry reactions[70,170,171]. Synthesis parameters can be modified to improve the phase purity of Ni-rich layered oxide materials. Mixed metal oxide materials, such as NMC materials, can be understood as a solid-solution of $LiNiO_2$, $LiCoO_2$, and $LiMnO_2$. Because of the redox behaviors of each transition metal and oxygen anion, Ni-rich NMC materials have increased practical capacity due to the ease of Ni oxidation compared to cobalt or manganese.[172] While each metal cooperatively improves the structural stability of NMC materials, they further complicate the surface chemistry.

To synthesize NMC cathode materials, a co-precipitation method is used. A 1M metal solution of 150 mL is mixed into 0.6 M $NiSO_4{\cdot}6H_2O$, 0.2 M $MnSO_4{\cdot}H_2O$, and 0.2 M $CoSO_4{\cdot}7H_2O$. The metal solution and base solution (2 M NaOH and 1.2 M $NH_3{\cdot}H_2O$, total 150 mL of H_2O) are separately stored in volumetric flasks. The reaction flask is kept under N_2 protection, decreasing some of the surface reactivity under ambient conditions. The starting solution (1 M NaOH and 1.2 M $NH_3{\cdot}H_2O$, total 100 mL) is placed into the reaction flask, heated to 50 ºC and stirred. The pH value is adjusted to 10.5 ± 0.2. The metal and based solutions are pumped into the starting solution at approximately 2 mL/min. The mixed metal hydroxide is collected and washed using copious amounts of deionized (DI) water, followed by isopropanol (IPA). The filtrate is collected and dried under vacuum at 120 ºC overnight.

High temperature calcination is essential for synthesizing oxide cathode materials.[173] Upon developing a calcination profile for layered Ni-rich oxide materials, there are a few parameters

that must be considered, including Li-salt melting point, dehydration of the $M(OH)_2$, and the ramping rate of heating and cooling of the material. From reported research and synthesis experiments, a trend (**Figure 25**) was developed to determine estimated temperatures necessary to make structurally robust mixed metal oxide materials.

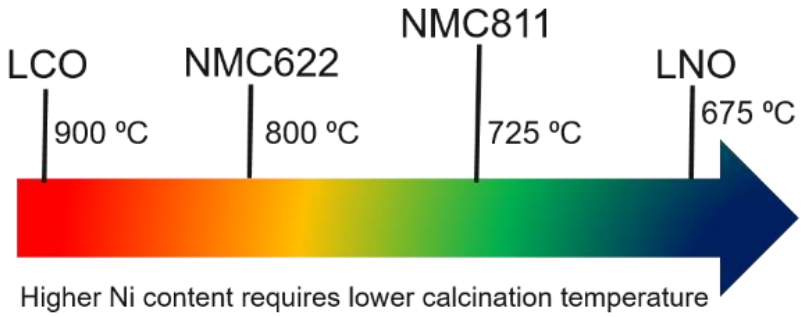

FIGURE 25: Calcination temperature required for various layered Ni-rich NMC materials.

As shown in **Figure 25**, $LiCoO_2$ (LCO) is typically calcined between 850-900 ºC.[151] With increasing amounts of Ni content, the calcination temperature must be decreased because of the difficulty to oxidize Ni^{2+} to Ni^{3+}, leading to more cation mixing and phase impurity. Cation mixing is common due to the similarity in the ionic radii size of Ni^{2+} and Li^{+} are 0.69 Å and 0.76 Å, respectively. Ni^{4+} is very reactive and unstable, leading to surface reconstruction. The equilibrium that exists between the layered and rocksalt structure generates significant challenges to understanding the surface and bulk chemistries of layered oxide materials.

For the NMC622 material used in the experiments described in **Chapter 3** the following calcination methods are used to obtain the pure material. First, the dried $[(Ni_{0.6}Mn_{0.2}Co_{0.2})(OH)_2]$ precursor material is mixed with LiOH (5% excess was added to compensate for Li loss to residual lithium species) thoroughly and calcined under pure oxygen flow at 2 L/min. The sample was

heated at 5 ºC/min to 460 ºC and held for 2 h. Then the sample was heated at 5 ºC/min to 800 ºC and held there for 6 h to ensure dehydration of the metal hydroxide. Finally, the furnace was cooled at 5 ºC/min to 25 ºC under constant oxygen flow. The final material after cooling is air sensitive and stored in the dry box as the final pristine $LiNi_{0.6}Mn_{0.2}Co_{0.2}O_2$ (NMC622) powder.

3.2 Catalytic Methods for C-X Bond Activations

Alternative energy sources have become attractive because of the increased necessity of electricity from portable electronic devices to electric vehicles. Converting energy from fuels, such as hydrocarbons and alcohols, to electricity is challenging because alkane and alcohol oxidation is kinetically sluggish. Catalysts are utilized to overcome a large activation barrier by decreasing the energy required for the reaction to proceed.

There are two categories of catalysts – homogeneous and heterogeneous. Homogeneous catalysis occurs in one phase, typically liquid. There is a positive correlation between solubility and catalytic activity. Ensuring solubility of the catalyst optimizes the number of catalytically active sites, maximizing conversion rates. Heterogeneous catalytic systems proceed in dual phase media, typically gas-solid or liquid-solid. While heterogeneous catalysis has its advantages, such as the ease of recovering the catalyst for reusability, there remains challenges in understanding mechanisms by which they proceed. Gas-solid interactions are more easily probed in comparison to liquid-solid interactions. This is largely due to the lack of *in situ* techniques that can probe liquid media. The vast majority of analytical methods requiring ultrahigh vacuum to operate, probing liquid-solid surface interactions is exceedingly challenging.

C-X bond transformations require harsh chemical conditions that generate many environmentally unfriendly waste by-products. To combat this challenge, researchers have studied

synthesis methods analogous to enzymes for various types of chemical transformations.[174,175] Metal-containing heterogeneous catalysts[176] have been utilized for different purposes in the chemical industry, including cracking for oil, oxidations, dehydrogenations, and isomerizations. In recent years researchers have sought methods to understand how different heterogeneous catalysts can activate the inert C-H bond. Latimer et al.[177] provided insight about a wide range of heterogeneous catalysts used to activate the C-H bond. It was suggested that hydrogen affinity (E_H) could be used as a universal descriptor of hydrocarbon activations that possess a radical-like transition state.

Transition state theory describes how reactants gain enough energy to overcome the activation energy barrier. The transition state is the moment at which a small molecule is activated for conversion to products. There exists a quasi-equilibrium in which some molecules lose energy and return back to the initial reaction state. The transition state explains bonding between the activated state of the reactant molecule and the catalyst. While C-H bond activation can be difficult, C-OH bonds are an easier place to begin when developing a platform for understanding mechanisms for electron transfer.

Experimental methods employed in catalytic studies prove useful in exploring the surface chemistry of metal oxide materials. Ni-rich layered oxide materials can be probed using small molecules that can be easily oxidized through catalytic pathways. In catalysis, conversion rates commonly illustrate the surface reactivity of a catalyst and the products that are generated after the completions of the reaction. By utilizing a small oxidizable organic molecule to interact with the layered oxide surface, electron transfer pathways can be elucidated in clean model systems. The following sub-sections of ***Section 3.2*** highlight how experimental methods from catalysis provide a platform for studying the chemistries of a frontier Ni-containing layered oxide material.

3.2.1 Catalytic Methods for Aerobic Alcohol Oxidation

Increasing the functionality of a molecule can be extremely desirable. Alcohol oxidation is extremely beneficial to the pharmaceutical and petrochemical industries by converting inexpensive, abundant reactants into more valuable, diverse products necessary for faster synthesis routes for developing new medicines and providing a method to explore new fuel types for alternative, cleaner energy. Alcohol oxidation is one method to generate higher functionalities, including aldehyde, carboxylic acids, and esters (**Scheme 1**).

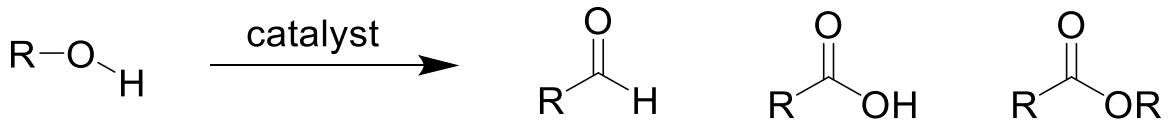

SCHEME 1: General form of aerobic alcohol oxidation, illustrating the aldehyde, carboxylic acid, and ester.

Metal nanocatalysts are typically supported on transition metal oxides. Nanoparticles (NPs) have been studied as catalysts because of their high catalytic activity and chemical selectivity even when mild reaction conditions are used.[178] Metal NPs receive interest because catalyst reactivity can be tuned by changing the size and shape. As the size of metal NPs decreases, the surface area increases causing faster reactivity rates. This phenomenon occurs because as the particle size decreases the number of collisions increases causes faster reactivity. Gaining size, shape, and morphology control of metal NP catalysts can be exploited to change selectivity and reactivity in catalytic reactions.[178] Although trends of NP size and catalyst reactivity have been determined for many systems, the exact reason why NP size has this effect remains a great debate.

Alloy systems have received attention because mixed metal NPs have been shown to enhance catalytic performance beyond that of a single metal.[179] Bimetallic[180,181,182,183] nanoparticles have recently received attention for aerobic alcohol oxidation under mild reaction conditions. Au-Pd[184,185] has been used for benzyl alcohol oxidation and it was determined that both metals play a role in the mechanism.[186] It was determined that Pd-rich alloys in bimetallic systems are predominantly responsible for the oxidation of benzylalcohol. By changing the ratio of Au-Pd in the system, different catalytic efficiencies can be observed. Research groups determined that Pd and Pt are useful catalysts, but a metal promoter such as Pb or Bi could be added to increase the rate and selectivity of Pd and Pt for oxidation reactions.[187,188]

Metal oxides have been shown to be used as supports for precious metal catalysts. Gold (Au)[189,190], platinum (Pt)[187], and copper (Cu)[191], are widely studied as precious metal catalyst supported on metal oxides. Many chemists make extensive efforts to determine the role metal oxide catalyst have in oxidation reactions. The role of the metal and support have been studied using different alcohol oxidation reactions, but the goal of most research is to determine the selectivity[192], catalytic efficiency, and reusability of metal catalysts.

Gold is typically known as very inert, but as a nanoparticle it can be very advantageous to promoting oxidation of alcohols. By tuning the NP size, a relationship between structure and activity can be studied. Because Au has so many advantageous properties, including chemoselectivity[193], many have explored how to improve the catalytic ability it possesses. By changing the metal oxide support, selective oxidation of alcohols is induced.[194] Many factors affect catalytic performance and can be explored to make relationships between reactivity rates and a specified reaction parameter.

Platinum and palladium are also used as metals catalysts and are also support on metal oxides. The catalytic activity of Pd, like Au, is driven by the size of the nanoparticles.[195,196] Pd/SiO_2-Al_2O_3 was shown to catalyze benzyl alcohol solvent-free.[195] The parameters for the benzyl alcohol oxidation were at 353K for 24 hours yielded 99% conversion and 99% selectivity. Even though Pd is an effective catalyst for alcohol oxidation, gold typically can outperform it when an alloy is present.

3.3 Developing a Model Platform for Study

Oxygen loss and electron transfer pathways have yet to be determined in the surface chemistry of layered metal oxide materials, specifically NMC materials. A model probing experiment was developed to analyze the surface chemistry of NMC622. Both the structural and electronic perturbations must be determined in the system. NMC622 is the preferred material to study because it is a frontier oxide cathode material that is well-studied and representative of layered oxides.[39,90,197–199]

A simple, clean model system is used to predict the mechanisms and understand potential electron and oxygen transfer pathways. To do so, we can take an example from heterogeneous catalysis to study the surface chemistry and quantify small molecule oxidation. Battery applications have complex cathode-electrolyte interfacial reactions yielding many oxidized carbonate molecules. Here, we employ benzyl alcohol as a small, organic molecule that is easily oxidized.

Benzyl alcohol oxidation has gained much attention in the oxidation catalysis literature[200–203] as a model reaction due to high selectivity and oxidation ease with limited product formation. Benzyl alcohol[204] (**Figure 26A**) is oxidized predominantly to benzaldehyde, followed by benzoic acid and an aldehyde coupling product, benzyl benzoate.[205–208] Gas chromatography coupled with

a flame ionization detector (GC-FID) provides an analytical method to quantify conversion products. To ensure that benzyl alcohol was the appropriate organic molecule that could be used to determine oxygen and electron transfer pathways, cyclic voltammetry (CV) was completed to determine the oxidation potential of benzyl alcohol using a three-electrode cell. Similarly to other Ni-rich layered oxides, the voltage window is 2.5-4.4V vs Li/Li^+, in which upper cutoff voltages accelerate surface oxygen loss and transition metal migration.[120,209,210]

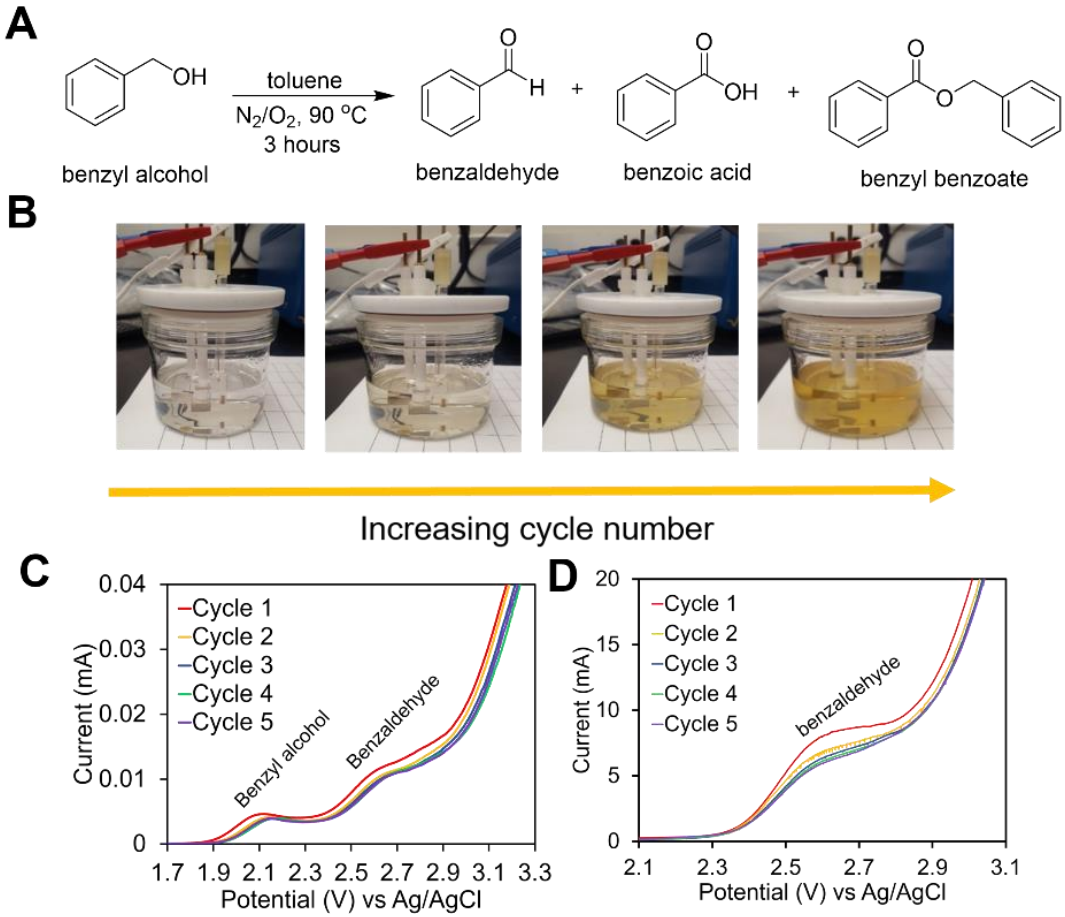

FIGURE 26: A) The reaction scheme of benzyl alcohol oxidized to its analogous products, including benzaldehyde, benzoic acid, and benzyl benzoate. The CV scans **B)** qualitatively show benzaldehyde production due to the increased yellow color with increased cycle number. CV analysis of both **C)** benzyl alcohol and **D)** benzaldehyde at 0.001V/s with a three-electrode cell show the onset oxidation potential of benzyl alcohol and benzaldehyde 4.8V vs Li/Li^+ and 5.3V vs Li/Li^+, respectively.

In a proper scheme, benzyl alcohol must be oxidized at higher potentials than the NMC622 voltage window. As shown in **Figure 26C, D**, the cyclic voltammetry experiments illustrate the oxidation potential for benzyl alcohol and benzaldehyde as 4.8V and 5.3V vs Li/Li^+, respectively. Qualitatively, as the cycle number increases the solution color becomes more yellow. A yellow solution color is indicative of product formation.

Cyclic voltammetry (CV) was obtained using a three-electrode cell in which platinum (Pt) served as the working and counter electrode. A scan rate of 0.001 V/s was used to obtain the data for five (5) consecutive cycles. The data in **Figure 26C** illustrates the onset oxidation potential and each of the peaks are labeled appropriately for the benzyl alcohol and benzaldehyde, suggesting the decomposition to the oxidized products. In **Figure 26D**, benzaldehyde oxidation was completed and a white precipitate was formed on the working electrode, further corroborating benzoic acid production at increased voltages.[211]

After developing a reliable, yet simple model our goal is to determine chemically-induced electronic perturbations of NMC622 through benzyl alcohol oxidation. This platform provides a model to explore the interplay between layered oxide material surface fragility and small, organic molecule oxidation. To decouple bulk and surface electronic changes, we employ X-ray absorption spectroscopy and X-ray photoelectron spectroscopy. Data analysis from this work yields a reaction mechanism in which small molecule oxidation disrupts NMC surface stability leading to more thermodynamically favorable arrangements, specifically rocksalt formation.

3.3.1 Results and Discussion

Extensive X-ray analysis provides electronic information to propose a reaction mechanism for NMC lattice oxygen loss (**Scheme 2**). We rationalized 6 steps in the scheme that describe surface structural disordering in the material due to thermodynamically favorable electron transfer pathways.

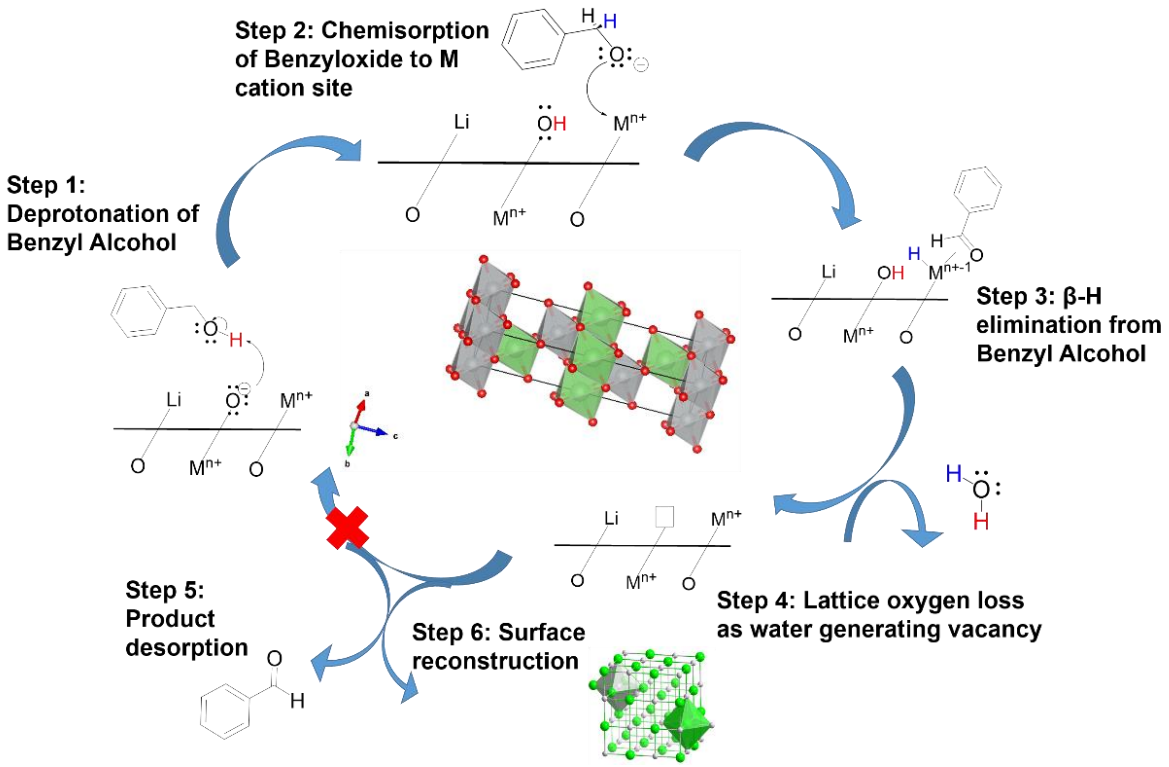

SCHEME 2: Reaction mechanism of NMC lattice oxygen loss during surface reaction with benzyl alcohol, illustrating structural rearrangement from layered to rocksalt.

The reaction mechanism is schematically depicted using a simple lattice structure. In step one, negatively charged oxygen anions promote surface basicity. The oxygen anions deprotonate benzyl alcohol leading to a benzyloxide species. Step 2 highlights that the surface becomes increasing basic due to surface hydroxides. The benzyloxide species then reacts with the transition metal cation. In Ni-rich layered oxide material, the redox center, Ni, is likely the most reactive

species. Because there are small concentrations of Mn and Co due to the mixed metal oxide composition, any metal cation is likely the site of benzyloxide reactivity. It was reported that after chemisorption of benzyloxide of the metal oxide surface, alkoxide species undergo β-hydride elimination. Upon benzyloxide conversion to benzaldehyde, lattice oxygen loss occurs through the generation of water. This oxygen vacancy generation in Step 4 leads to either two potential pathways – product desorption (Step 5) and surface reconstruction (Step 6). Extensive Synchrotron X-ray analysis is used to rationalize and corroborate each proposed step.

3.3.2 Chemical Delithiation Methods to Develop Electronic Continuum for Study

$LiNi_{0.6}Mn_{0.2}Co_{0.2}O_2$ (NMC622) was synthesized using a co-precipitation method, similar to the one described in ***Section 3.1.1***. After synthesis and calcination, we choose to mimic various oxide cathode states of charge by performing chemical delithiation to develop electronically tuned NMC622 oxidation states. Chemical delithiation[46,90] provides a chemical method to generate electronic perturbations in the TM*3d*-O*2p* orbital hybridization with correlated to surface oxygen lattice loss[4,212–214]. The lattice oxygen that is lost from the transition metal oxide material can be used to promote benzyl alcohol oxidation.

There are two methods that can be used to delithiate layered oxide materials. In both cases, an oxidant is used that can bind with the Li^+ causing it to be deintercalated from the lattice framework, similarly to electrochemical cycling. The two oxidants that are typically used include nitronium tetrafluoroborate (NO_2BF_4) and bromine (Br_2). The pristine powder can be mixed with stoichiometric ratios to adequately delithiated the material. The mixture is stirred on the benchtop for 24 hours before centrifuging the dispersed material post-delithiation. The powder is then

washed with acetonitrilte three times to remove an undesired species related to the oxidant. The powder is them dried under vacuum at 120 ºC.

The trouble with using NO_2BF_4 for chemical delithiation is that Ni-rich oxide materials are electronically fragile. This means that in many cases NO_2BF_4 delithiates the material too rapidly causes electronic repulsion between the transition metal layers due to the negatively charged oxygen anions. This electronic repulsion can facilitate in chemomechanical cracking of layered oxide materials, exposing more rocksalt structure than the layered structure.[39] This will influence expected trends in oxidation state with respect to delithiation degree. Bromine proves to be a milder oxidant and was used to develop a linear trend between relative oxidation state and delithiation degree. Because the Br_2 removes Li more slowly, sometimes higher concentrations of delithiation may prove to be less oxidized than the electrochemically delithiated counterparts.

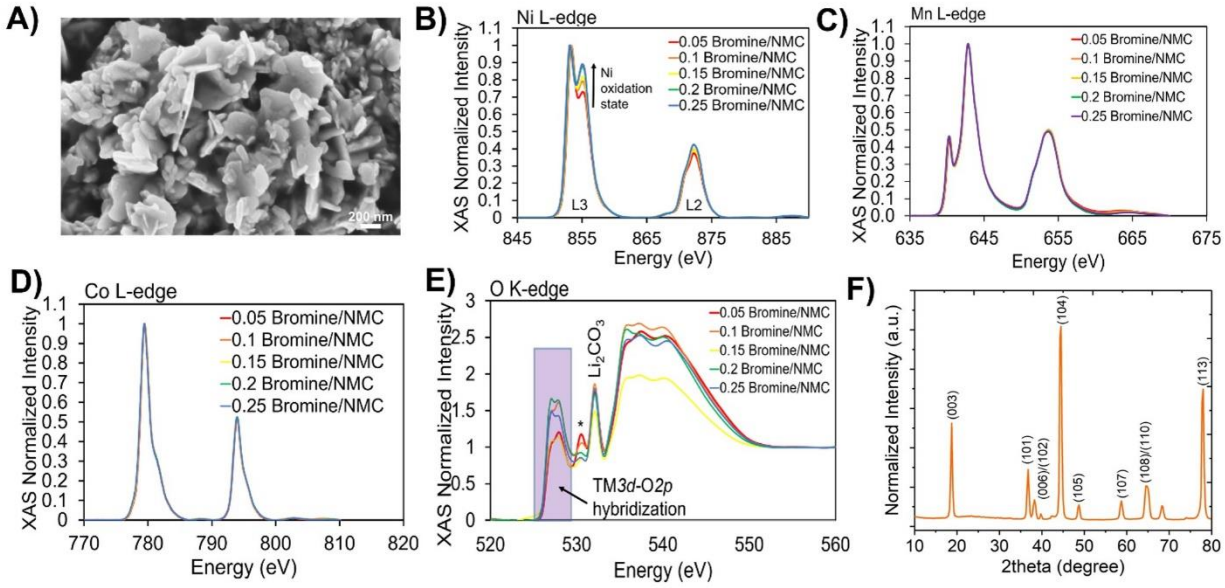

FIGURE 27: NMC622 surface structure and electronic characterization including **A)** SEM of the pristine powder showing a polycrystalline structure. Soft-XAS provides electronic analysis in TEY mode at five different delithiated states for the **B)** Ni L-edge, **C)** Mn L-edge, **D)** Co L-edge, and **E)** O K-edge. The Br_2/NMC ratios represent the amount of Ni oxidation based on theoretical chemical delithiations. The XRD data **F)** shows bulk electronic changes and is provided for the pristine material.

After synthesizing the pristine NMC622, as described in ***Section 2.1.1***, the material was characterized using scanning electron microscopy (SEM) (**Figure 27A**). The SEM illustrates the polycrystalline structure of the NMC622 layered oxide material. To gain a continuum of surface electronic states, the material was chemically delithiated and synchrotron X-ray absorption spectroscopy (XAS) was employed to determine the relative oxidation state of the material post-delithiation.

XAS can operate in many modes to elucidate orbital occupancy from the surface or bulk of the material. Using soft X-rays, or low energy excitation, surface-most orbital occupancy can be determined. A complete description of XAS working principles can be found in **Chapter 2**. Here, we manipulate the surface oxidation state and develop the electronic continuum illustrated in **Figure 27B**. L-edge provides occupancy information that corresponds to electron excitation from a 2*p* to 3*d* orbital. In the total electron yield (TEY) mode, we probe the material to a depth of 5-10 nm and find that with increasing amounts of Br_2/NMC concentrations there is a linear response in Ni oxidation state, as expected. The Mn L-edge (**Figure 27C**) and Co L-edge (**Figure 27D**) have no change in oxidation state. This corroborates the knowledge that Ni is the redox center and will have greater electronic perturbations due to the TM*3d*-O*2p* orbital hybridization. The O K-edge pre-edge features are indicative of the TM*3d*-O*2p* orbital hybridization that occurs at various states of delithiation. The changes in peak intensity are directly related to the perturbations in the orbital overlap. The peak denoted with the asterisk (*) is Mn^{4+}/Ni^{2+}-O, which corroborates with previous reports of the O K-edge for NMC622.[46] Although the work does not focus on residual lithium and carbonate surface species, due to the inherent basicity of the material there is a peak in the O K-edge features that correspond to Li_2CO_3, which is inevitable for layered oxide materials.[163,17,64,170,215] **Figure 27** provides a summation of the structure and electronic

properties of the pristine NMC622 material that is necessary for comparison upon introducing the surface with the probing organic molecule, benzyl alcohol.

3.3.3 Decoupling Surface and Bulk Electronic Properties

Layered oxide materials are complex in the sense that the surface and bulk properties have their independent influences on the system. Although the surface and bulk may seem independent, their properties have distinct interplay in how oxide material degrade over time. To decouple the surface and bulk chemical and electronic properties, extensive materials characterization was completed.

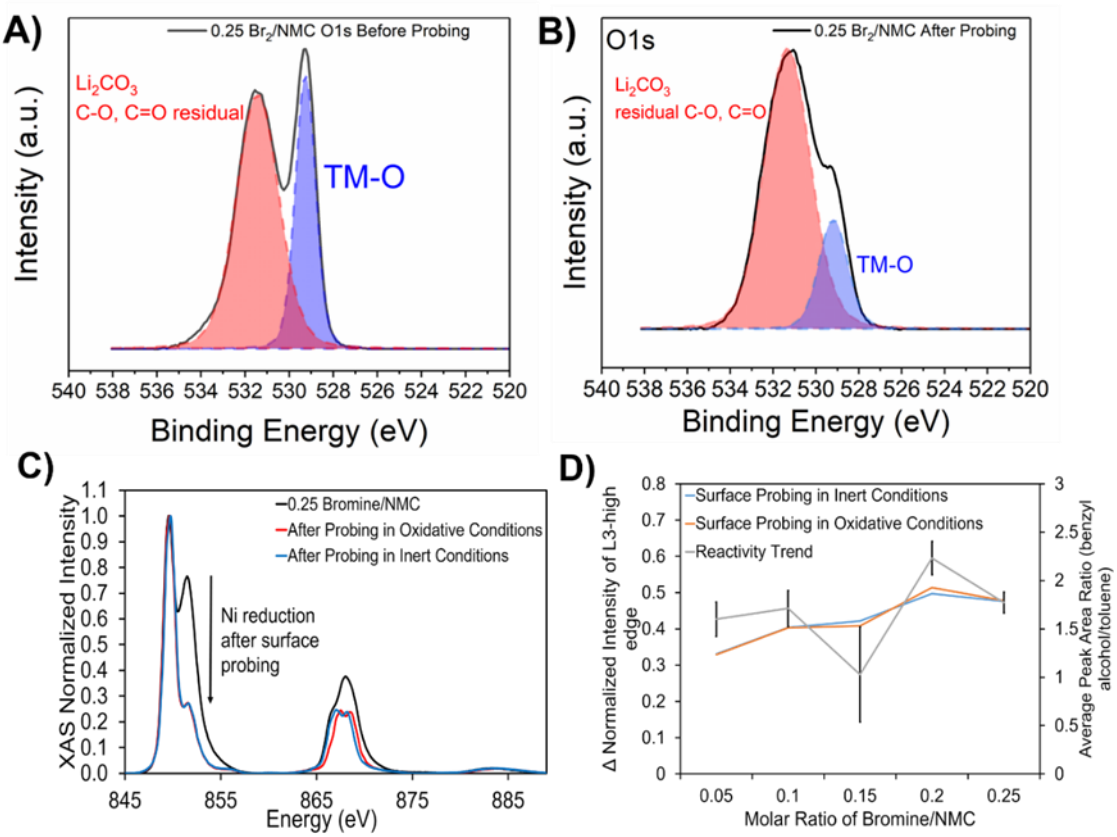

FIGURE 28: NMC622 oxidized with 0.25 Bromine/NMC showing the XPS O1s spectra for **A)** before and **B)** after surface probing with benzyl alcohol illustrating decreased TM-O bonding and increased C-O species. This is corroborated with **C)** soft-XAS data before and after probing under oxidative and inert conditions, in which the oxidation state becomes reduced. Lattice oxygen release can facilitate benzyl alcohol oxidation, as shown by a **D)** correlation trend between the Ni L-edge and benzyl alcohol decomposition.

X-ray photoelectron spectroscopy (XPS) is a surface analytical technique that provide information about the chemical environment of solid surfaces. The working principles of XPS are discussed in depth in **Chapter 2**. Researchers have used XPS to determine surface characteristics of NMC materials.[216–218] In the experiment, we stir the NMC622 material in a benzyl alcohol solution. After the experiment, the material was dried under vacuum prior to performing XPS. When analyzing the O1s spectra before (**Figure 28A**) and after (**Figure 28B**), we find that the TM-O peak has decreased after the reaction due to lattice oxygen loss. This is likely because of surface

reconstruction upon reacting with benzyl alcohol. In contrast, the C-O/C=O/residual peak increases, corresponding to the residual lithium species[219] and desorbed benzyl alcohol or its oxidized products on the surface of the material.

Electronically, there are also occupancy changes after probing the material with benzyl alcohol. The L_3-edge (**Figure 28C**) illustrates that Ni reduction occurs and is non-selective under oxidative or inert conditions. This implies that benzyl alcohol oxidation has no direct relationship with ambient O_2 provided in the experiment and is facilitated by the lattice oxygen loss in the NMC material. Notably by the figure, Ni is reduced to the same oxidation state regardless of the initial oxidation state. Upon plotting the normalized intensity difference of the L_3-edge shoulder for both reaction conditions and correlating that trend to benzyl alcohol oxidation (**Figure 28D**). In doing so, the transition metal reduction – benzyl alcohol oxidation relationship is as expected, due to the thermodynamically favorable electron transfer pathway.

While XPS and soft-XAS provide information about the surface of the material, hard-XAS is required to determine oxidation state changes in the bulk. Hard X-rays have higher energy and therefore can penetrate into the bulk of the material to provide orbital occupancy information. Transition metal K-edge data yields bulk information because it excites electrolytes from a 1*s* to 3*d* orbital. **Figure 29** illustrates that each of the transition metals becomes reduced, as shown by the edge shifting toward lower energies.

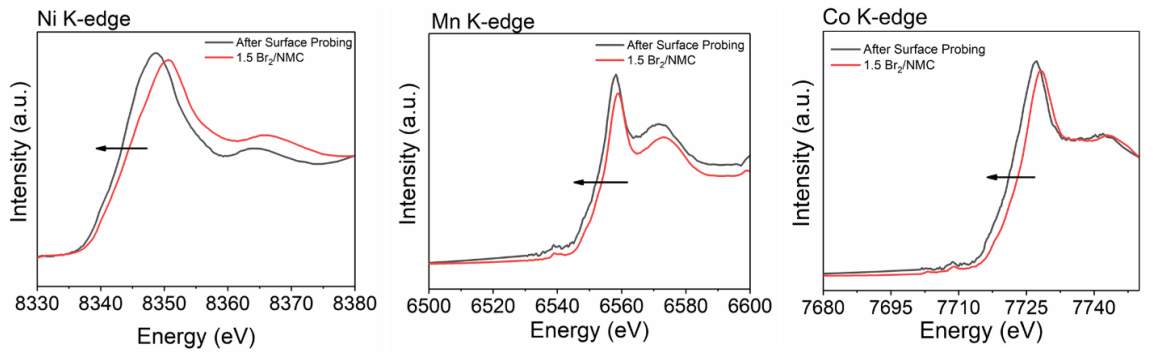

FIGURE 29: Hard-XAS from NMC622 before and after surface probing for 1.5 Br_2/NMC ratio for the **A)** Ni K-edge, **B)** Mn K-edge, and **C)** Co K-edge. Each metal cation undergoes bulk metal reduction after probing with benzyl alcohol.

Ni reduction (**Figure 29A**) was expected due to the TM*3d*-O*2p* orbital hybridization perturbation and structural rearrangement. Mn (**Figure 29B**) and Co (**Figure 29C**) also under transition metal reduction, as shown by the left shift in the K-edge edge features. Overall bulk metal reduction was unexpected but it is likely caused by benzyl alcohol being a strong reducing agent compared to typical electrolyte solvents. As a strong reducing agent, benzyl alcohol compromises the NMC structural integrity. Hard-XAS data support the theory that structural fragility is caused by oxygen loss and bulk electronic changes. Oxygen loss leads to localized stress, promoting the formation of microcracks.[39,220] A dual presence of layered and rocksalt structure exists upon the formation of cracks via chemomechanical breakdown.

3.4 Conclusions

From this study, a mechanism for lattice oxygen loss is proposed. This model study was proven to be simple, yet insightful due to use benzyl alcohol. Electrochemical testing illustrated that the onset oxidation potentials for benzyl alcohol and benzaldehyde were 4.83V vs Li/Li^+ and 5.23V vs Li/Li^+, respectively. While benzyl alcohol is harder to oxidize than Li-containing liquid electrolyte species, it provides a quantifiable, controllable model. Additionally, it has comparable

oxidation potential to other electrolyte solvents, but upon the additional of Li-salts the oxidation potential of organics decreases. Model systems are necessary to decouple the surface and bulk chemical and electronic changes to understand the structural decomposition in layered oxide materials.

Extensive X-ray analysis is used to decouple surface and bulk chemistries. The bulk oxidation state illustrates transition metal reduction. This is likely due to benzyl alcohol being a strong reducing agent. The chemomechanical breakdown leads to two distinct structures in the material – layered and rocksalt. The structural changes are due to TM*3d*-O*2p* orbital hybridization perturbations upon probing the system with benzyl alcohol. Soft-XAS and XPS are used to determine the explicit surface changes with respect to probing NMC622 with benzyl alcohol. By corroborating all of the data, the proposed mechanism illustrates that the lattice oxygen loss occurs via water generation during benzyl alcohol oxidation.

While this study using a small, organic molecule to probe the structural changes of layered oxide materials, it is expected that electrolytic species can follow a similar reaction pathway. The cathode-electrolyte interfacial reactions can lead to oxide cathode degradation which greatly impacts battery performance. This study highlights the interplay between the structure and bulk chemistries that lead to the oxide cathode structural instability.

CHAPTER 4: UNDERSTANDING THE STRUCTURAL AND CHEMICAL EVOLUTION AROUND PHASE TRANSITIONS OF CO-FREE, NI-RICH LAYERED OXIDES

4.1 Introduction

Energy storage devices continue to exponentially grow due to the demand for consumer electronics and electric vehicles. Layered oxide cathode materials have dominated commercial electronics and have become the starting point for fundamental battery research.[66] $LiCoO_2$ became an exemplary layered oxide cathode material after it was commercialized in 1991. Within the past decade, research efforts have shifted towards decreasing the Co content to improve cost efficiency, lower toxicity, and mitigate geopolitical issues deriving from mining. In making this shift away from Co-containing layered metal oxides, the challenge is in determining the balance between structural stability and output capacity. This transference gave rise to multi-metal layered oxide cathodes, such as $Li[Ni_xMn_yCo_{1-x-y}]O_2$ (NMC) and $Li[Ni_xCo_yAl_{1-x-y}]O_2$ (NCA) materials.

While considerable research has been conducted to eliminate Co[221–223], Ni-rich materials have structural instability caused by transition metal migration and lattice oxygen loss. Surface reconstruction is arguably caused by electronic changes upon charging. Upon charging the TM*3d*-O*2p* orbital hybridization is perturbed, causing the system to possess undesired, cathode–electrolyte interfacial reactions. Density functional theory studies show that the Fermi level of the transition metal oxide (TMO) cathode is located near the HOMO energy level of typical liquid electrolytes used in lithium batteries.[77,40] The Fermi level of the TMO is lowered in the charged state, promoting favorable electron transfer from the HOMO of the electrolyte to the conduction band of the layered TMO. This encourages transition metal reduction, further promoting metal

cation migration and lattice oxygen loss. Repetitive charge-discharge cycles exacerbate the structural fragility of Ni-rich layered oxide materials. Repetitive cycling leads to an increase in capacity fading caused by decreased Li^+ (de)intercalation kinetics. While electrochemical influences are largely to blame for cathode degradation, mechanical agitation can exacerbate structural degradation due to accelerated side reactions.[90] This is key to note when performing accelerated experimental analysis that include stirring.

Initial causes of surface reconstruction are still under debate due to complexities of a dynamic Ni-rich layered oxide surface[224]. The significant interplay between the material properties and uncontrollable interfacial reactions make it challenging to understand how the cathode-electrolyte interphase (CEI)[225] causes oxide cathode degradation behavior. It is known that state-of-charge impacts oxide cathode surface fragility.[52] Layered oxides with ultrahigh Ni content usually exhibit four different phases at specific states-of-charge, including hexagonal H1, monoclinic M, hexagonal H2, and hexagonal H3.[7] Transitions between different phases can create mechanical stress in these materials, contributing to degradation of layered cathodes. Multi-element doping approaches have been applied to mitigate these phase transitions.[17,103,104,221] However, there remains a limited understanding of the Ni-rich layered oxide phase transitions and degradation behavior.

Although CEI interactions mostly occur on the surface-most of the oxide cathode material, there are global structural effects influenced by state-of-charge, and phase transitions during cycling.[226,33,227] In this study, degradation kinetics of $LiNiO_2$ are deduced by introducing a voltage oscillation experiment. By employing X-ray spectroscopy and strategic electrochemical testing, the interplay between bulk phase transitions and oxide cathode degradation behaviors are explored. Herein capacity fading and Coulombic efficiency behaviors are determined. Additionally, the

work explores the electronic and structural distortions at the $LiNiO_2$ charging plateaus. The following sections provide the technical results and discussion of the experimental findings.

4.2 Results and Discussion

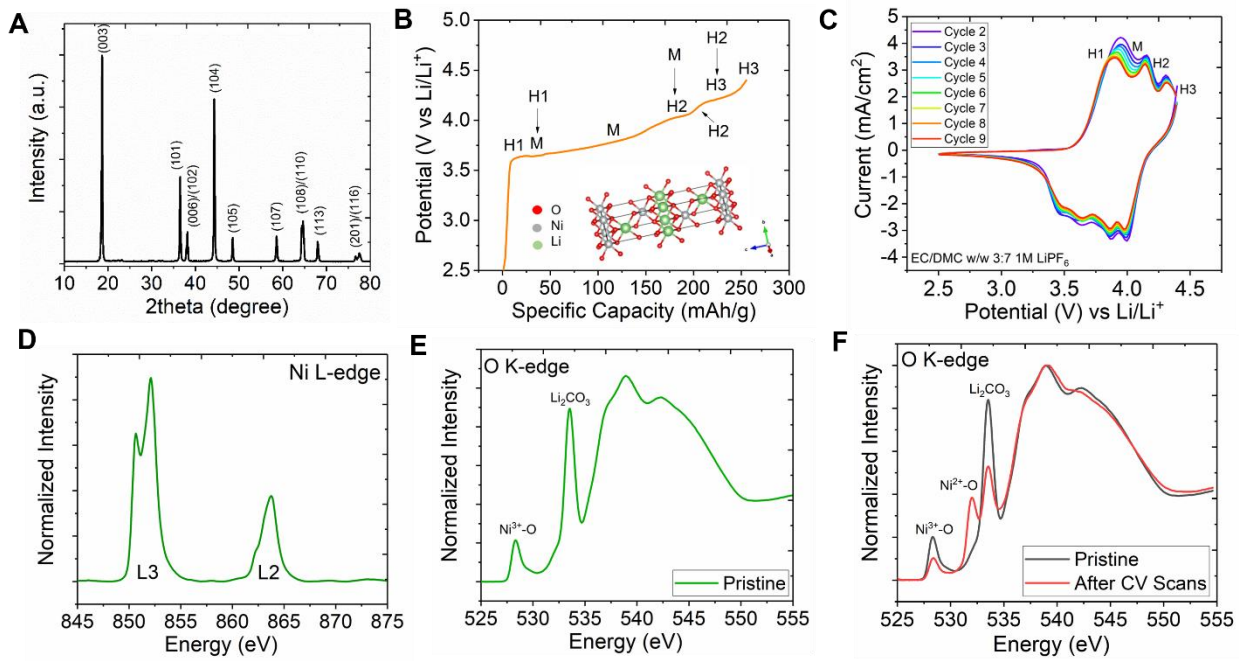

FIGURE 30: Decoupling surface and bulk properties of $LiNiO_2$ cathode material using **A)** the pristine XRD pattern, illustrating the $I_{(003)}/I_{(104)}$ ratio of 1.3 for the layered material. The bulk structural phase transitions are highlighted in the **B)** charging profile for LNO cycled with Li metal anode from 2.5-4.4 V vs Li/Li^+ with the associated hexagonal and monoclinic structures. **C)** The CV curves highlight the phase transitions and the irreversibility that is found in Ni-rich oxide cathodes that lead to capacity fading and overall decreased battery performance. Soft XAS in TEY mode was used to determine the relative **D)** Ni oxidation state using the Ni L-edge, illustrating increased orbital vacancy shown by the L3-edge peak intensity ratio. To indirectly probe the TM*3d*-O*2p* orbital hybridization perturbations, **E)** the pristine $LiNiO_2$ O K-edge shows the Ni^{3+}-O bonding and Li_2CO_3 due to the surface reactivity with CO_2. The pre-edge features in the **F)** O K-edge comparing the pristine and after CV scans show the increase of Ni^{2+}-O bonding and a decrease in the Ni^{3+}-O bonding and Li_2CO_3 peaks, highlighting the structural instability after cycling.

$LiNiO_2$ serves as a model platform. X-ray diffraction (XRD) provides bulk structural information. Typical layered oxide materials have an XRD pattern that possess two distinct peaks that confirm the structure, the (003) and (104) peaks. In $LiNiO_2$, the (003) peak has a higher normalized intensity than the (104) peak, as shown in **Figure 30A**. The XRD pattern can be used to evaluate the degree of cation mixing in the layered oxide material by calculating I_{003}/I_{104}. The intensity ratio of the calculated (003)/(104) peaks is 1.3. The higher the I_{003}/I_{104} ratio is indicative of minimal cation mixing and no presence of NiO-type structures.

After determining the structural purity of $LiNiO_2$, basic electrochemical testing is performed. A Li metal anode is used in the testing with EC/DMC w/w 3:7 1M $LiPF_6$ electrolyte. The cell is cycled between 2.5-4.4V vs Li/Li^+. The charging curve (**Figure 30B**) indicates the associated phase transitions of the material. The $LiNiO_2$ cathode exhibits four different phases at different states-of-charge, including hexagonal H1, monoclinic M, hexagonal H2, and hexagonal H3.[31] The transition between two different phases is reflected in the voltage profile as a plateau. Cyclic voltammetry (CV) (**Figure 30C**) is used to further illustrate the redox events during charging and discharging. As the cycle number increases, the peak current decreases. This is likely due to structural distortions in the material that are influencing Li^+ de-/intercalation kinetics.

While XRD and electrochemical testing provide bulk structural information of the material, it is important to determine how structure and electronic properties are interconnected. Synchrotron X-ray absorption spectroscopy (XAS) is used in the total electron yield (TEY) mode to investigate the surface electronic properties of the material.[218,221,162] The Ni *3d* orbital occupancy is analyzed using the Ni L-edge (**Figure 30D**). The $L3_{right}$ peak has a greater normalized intensity than the $L3_{left}$ peak, suggesting a decreased Ni *3d* orbital occupancy and increased Ni oxidation state. The Ni oxidation state changes are indirectly probed using the O K-edge.

Additionally, the O K-edge is used to directly probe TM*3d*-O*2p* orbital hybridization perturbations (**Figure 30E**). The O K-edge is generated by electron excitation from O *1s* to O *2p* orbital. There are two distinct features in the pre-edge region showing a peak for Ni^{3+}-O and surface carbonate. Carbon dioxide in the air readily reacts with the surface of Ni-rich layered oxide material, generating Li_2CO_3 on the surface as a residual lithium compound after synthesis.[17,64,71]

After CV cycling, $LiNiO_2$ undergoes electronic changes which can be qualitatively determined by comparing the O K-edge pre-edge features. **Figure 30F** highlights the pre-edge features of the pristine cathode and the recovered cathode after the CV testing for 9 cycles. The O K-edge illustrates that there is a decrease in the amount of Ni^{3+}-O on the material after cycling and an increase in Ni^{2+}-O.[46] This corroborates previously reported data suggesting that after cycling Ni-rich layered oxides undergo surface reconstruction and have surface metal reduction.[162] In $LiNiO_2$, the Ni oxidation state is higher than 2+ and upon charging it can approach 4+. Ni^{4+} is a very unstable oxidation state that undergoes rapid reduction. When the oxidation state is closer to Ni^{2+}, the rocksalt structure predominates. Metal reduction, metal migration, and oxygen loss work cooperatively to generate significant battery performance degradation. The Li_2CO_3 content evident in the O K-edge spectrum has decreased after cycling which is expected due to applied voltages greater than 3.8 V vs Li/Li^+. Carbonate decomposition was evident in cycle 1 of the CV plot, but is removed as a formation cycle.

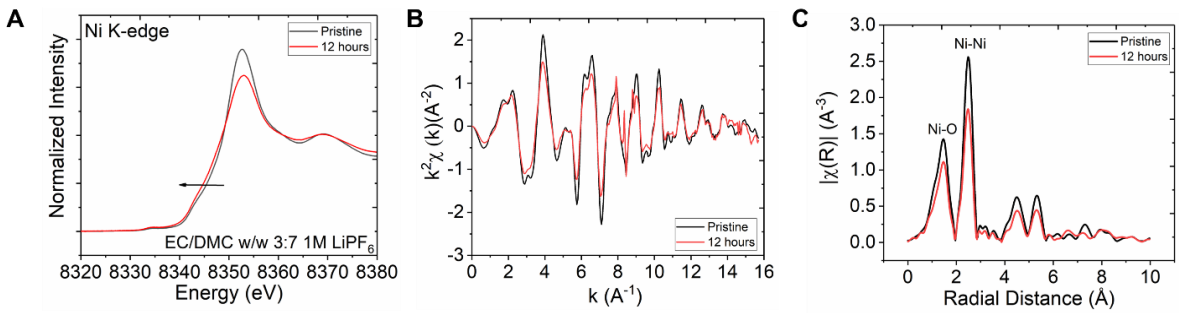

FIGURE 31: Bulk changes of $LiNiO_2$ powder after stirring in the electrolyte (EC/DMC w/w 3:7 1M $LiPF_6$) for 12 hours. **A)** The Ni K-edge shows that after stirring in the electrolyte, the edge has a left shift highlighting Ni metal reduction. **B)** The EXAFS and **C)** radial distance plots illustrate decreased peak intensities after 12 hours of stirring, corresponding to structural disordering due to mixed Ni oxidation states.

To determine the effects of chemical electrolyte decomposition on $LiNiO_2$ electronic instability, an electrolyte stirring experiment is performed. X-ray absorption near edge spectroscopy (XANES) and extended X-ray absorption fine structure (EXAFS) is used jointly to probe bulk electronic and local structure changes in the material. The bulk electronic changes after the pristine power is stirred in the liquid electrolyte, EC/DMC w/w 3:7 1M $LiPF_6$, is reported in **Figure 31**. The electrolyte stirring experiment provides an accelerated testing method to determine the influences chemical electrolyte decompositions at the oxide cathode surface have on the bulk electronic properties. This method provides a platform to understand how electrolyte decomposition impacts the electronic stability of $LiNiO_2$ without the added complexity of the electrochemical decomposition pathway. After stirring the material in the electrolyte solution for 12 hours, the material was collected and dried under vacuum at 120 ºC. The Ni K-edge provides bulk oxidation state changes. EXAFS provides an indirect method to understand the structural distortions in the material after the stirring experiment. Hard-XAS probes the bulk of the material due to high energy X-rays that can generate electron excitation from a *1s* to *3d* orbital. Upon analyzing the edge features, the Ni K-edge has a shift towards decreased energy. This suggests a

decrease in Ni oxidation state in the bulk (**Figure 31A**) after 12 hours of stirring in the electrolyte solution. Transition metal reduction, metal migration and oxygen loss are the fundamental phenomena that occur during surface reconstruction. The bulk oxidation state changes suggest that with global Ni reduction, there is a significant amount of structural reordering throughout the material. In summary, the electrolyte stirring experiments show that the reactions between electrolyte and pristine $LiNiO_2$ create substantial TM reduction, corroborating previous studies reported for other Ni-containing layered oxide materials upon exposure to electrolytic species.[212]

The EXAFS features (**Figure 31B**) of the Ni K-edge illustrate the $LiNiO_2$ structural distortions after introducing the Ni-rich powders to the electrolyte solution by having a depression in the peak intensities. The decrease in peak intensity is also attributed to a decrease in the coordination number for Ni-O due to the structural disordering after stirring in the electrolyte solution. Electronically when two structures exist within the material – layered and rocksalt – Ni is likely in a mixed valence state. In the layered arrangement, Ni has an oxidation state closer to 3+, whereas in the rocksalt structure it is 2+. The duality in the oxidation state enhances the mean square disorder within the Ni-O and Ni-Ni distance decreasing the peak intensities illustrated in **Figure 31B**. The structural distortion is corroborated by the radial distribution changes shown in **Figure 31C**. This data provides the atomic distances before and after introducing the oxide cathode powder to the electrolyte solution. After the electrolyte stirring experiment, there are no discernible changes in the interatomic distances for Ni-O and Ni-Ni, but the decrease in peak intensity correlates the structural distortions due to chemically induced perturbations of structural stability. Structural distortions are highly likely in Ni-rich layered oxide materials upon surface chemical interactions with liquid-based electrolytes. The electrolyte stirring experiment allowed us to probe the electronic changes of the material without electrochemical responses, but how can

this be translated into exploring the chemistries associated with a more practical battery cell? To correlate the electrolyte stirring experiment with electrochemical cycling, a voltage oscillation electrochemical testing method was developed. It limits the state-of-charge changes of the $LiNiO_2$ material, generating a testing method to evaluate the compatibility between cathode and electrolyte selection with degradation behaviors.

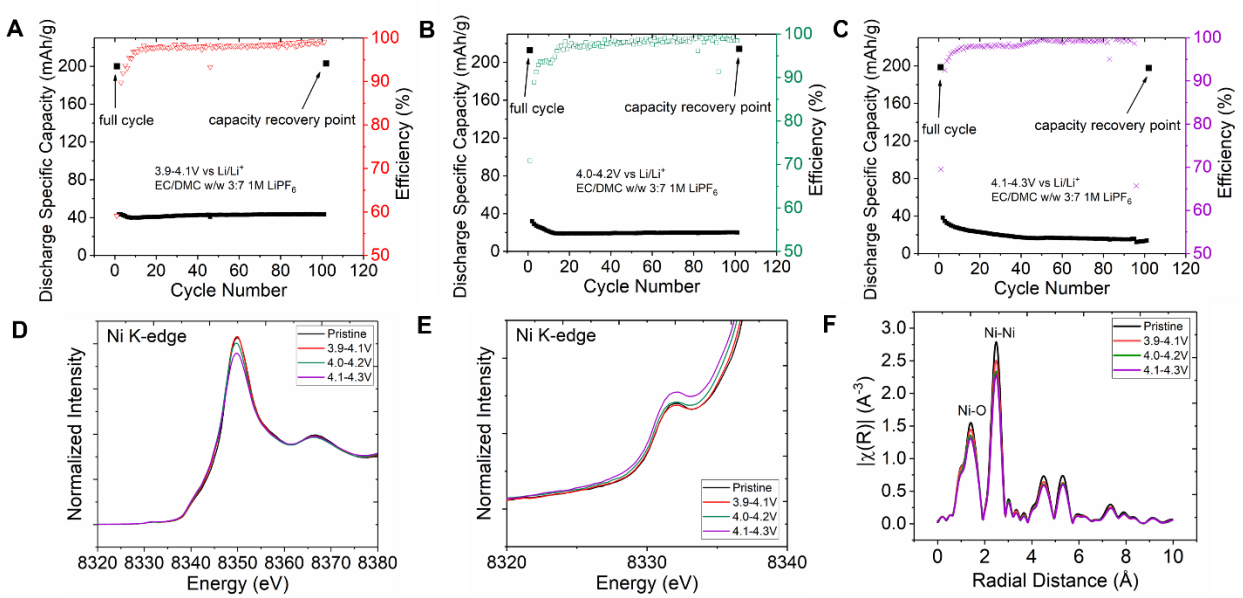

FIGURE 32: Specific discharge capacity and Coulombic efficiency behaviors while oscillating the voltage at **A)** 3.9-4.1V, **B)** 4.0-4.2V, and **C)** 4.1-4.3V vs Li/Li^+. The experiment was completed with one full charge-discharge cycle, followed by 100 oscillations around the specified voltage window, and then returning to a full charge-discharge cycle. The full charge-discharge cycles were completed from 2.5-4.4V vs Li/Li^+ at 1C. At the capacity recovery point found after the 100 voltage oscillations, bulk electronic changes were probed using XANES and EXAFS. At the capacity recovery point, the **D)** Ni K-edge data shows that increased voltage corresponds to Ni reduction. The **E)** pre-edge Ni K-edge features provide indirect structural information, highlighting that increased voltage corresponds to higher peak intensity and increased structural distortion. **F)** The radial distance plots show peak depression with increased voltage oscillation voltages, illustrating the bulk structural distortions likely caused by the presence of dual structures.

Structural changes and electronic perturbations are aligned in that electrolyte solvents can exacerbate transition metal reduction and oxygen loss in the material. Li^+ de-/intercalation kinetics become limited due to the structural distortions. This leads to overall capacity fading and poor

Coulombic efficiency. Many studies have attributed the performance degradation of $LiNiO_2$ to the multiple phase transitions during charging and discharging, because such phase transitions are believed to destabilize the layered lattice.[104,228] On the other hand, research has shown that the surface degradation caused by the side reactions with the electrolyte play an important role in performance degradation.

The voltage oscillation experiments provides a useful method to decipher oxide cathode degradation behavior. In addition, it provides a method to gain a better understanding of the electrochemical consequences of different phase transition regions on the cathode degradation. The latter two phase transitions – M to H2 and H2 to H3 – are most notably associated with performance degradation. First, a full charge-discharge cycle is completed between 2.5-4.4V vs Li/Li^+ at 1C. This allows for the initial surface reaction to occur, removing most residual lithium species. After one full cycle, the voltage was oscillated around a particular window including 3.9-4.1V (M to H2, **Figure 32A**), 4.0-4.2V (H2 to H3, **Figure 32B**), and 4.1-4.3V vs Li/Li^+ (**Figure 32C**). After oscillating around the narrow voltage window for 100 cycles, the capacity was recovered by returning to the full charge-discharge cycling parameters. After capacity recovery, the cell was dissembled, and the cathode underwent post-mortem X-ray analysis to determine the electronic and structural changes (**Figure 32D-F**).

First, we oscillate the voltage between 3.9-4.1V vs Li/Li^+ which is greatly associated with the M to H2 charging plateau (**Figure 32A**). When analyzing the oscillation region, the data illustrates that there is minimal capacity fading, although after the full charge-discharge cycle, there is some decrease in Coulombic efficiency that is quickly regained. At subsequent voltage windows at 4.0-4.2V vs Li/Li^+ (**Figure 32B**) and 4.1-4.3V vs Li/Li^+ (**Figure 32C**), there are increased amounts of discharge capacity fading during the voltage oscillation, suggesting that there

is more significant oxide cathode degradation. Upon beginning the voltage oscillations, the discharge capacity is similar for each of the voltage windows. Nevertheless, at the higher voltage windows there degradation is described by exponential decay. Upon analyzing the Coulombic efficiency, we find that during the first 100 oscillations at each of the voltage windows the efficiency recovery exhibits similar behavior.

To correlate the electrochemical data to a physical meaning of the oxide cathode material, we analyze the pre-edge and edge features of the Ni K-edge. The edge features show a slight left shift in energy (**Figure 32D-E**), suggesting that there is bulk metal reduction with increasing voltage oscillation windows. This is expected due to the irreversibility of the latter phase transition from H2 to H3, largely associated with oxygen loss. There are increased amounts of rocksalt structure present after only 100 voltage oscillations at the higher voltage windows. This suggests that the higher voltage phase transition possesses more significant structural distortions. Taking a closer look at the EXAFS spectrum in **Figure 32F**, there is no difference in Ni-Ni radial interatomic distances at higher voltage oscillation windows. This same trend is apparent in the Ni-O radial interatomic distance, with respect to oscillation voltage window. The peak intensity of the two highlighted peaks decreases with increasing voltage oscillation window. Here, the intensity correlates to structural evolution in which decreased intensity suggests a more disordered structure. The degradation is the most significant at 4.1-4.3V, followed by 4.0-4.2V, and then 3.9-4.1V vs Li/Li^+.

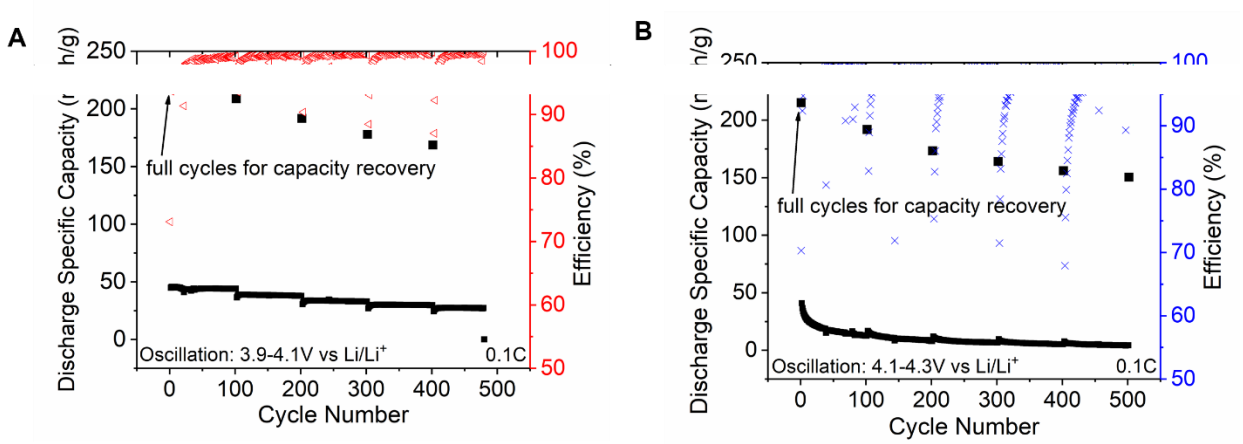

FIGURE 33: Extended voltage oscillation experiment in EC/DMC w/w 3:7 1M $LiPF_6$ at 0.1C. A full cycle from 2.5-4.4V vs Li/Li^+ was completed, followed by 100 voltage oscillations at the charging plateaus for **A)** 3.9-4.1V and **B)** 4.1-4.3V vs Li/Li^+. The charging plateaus and are in the voltage regions mostly associated with irreversible capacity fading. After the oscillations, another full cycle is completed to determine the capacity recovery value to monitor fading with respect to the phase transition regions. Extended voltage oscillations with full cycle capacity recovery points show that the latter phase transition undergoes more side reactions due to increased cycle numbers required to regain optimal Coulombic efficiency. The capacity recovery points illustrate the degradation behaviors at the phase transition regions, in which 3.9-4.1V and 4.1-4.3V vs Li/Li^+ oscillations have a linear and exponential decay trend, respectively.

After increasing the number of cycles and charging rate for the voltage oscillations, degradation behavioral trends are examined. By plotting the Coulombic efficiency during the oscillation, we can also determine how fast the Coulombic efficiency can recover after the full range cycle (**Figure 33**). During the first charge, each of the cathode materials have an initial capacity of >200 mAh/g, as expected with $LiNiO_2$ cathodes. At the first charging plateau, found at 3.9-4.1V vs Li/Li^+ window, the voltage oscillations illustrate minimal capacity fading. Additionally, by analyzing the Coulombic efficiency plot it is evident that the efficiency reaches equilibrium much faster than at the higher voltage oscillation window**,** in which the efficiency shows more resistance towards regaining equilibrium and the optimal Li^+ intercalation ability. By taking a closer look at the Coulombic efficiency recovery for each of the voltage oscillation regions, we find that 4.1-4.3V vs Li/Li^+ has a decreased Coulombic efficiency recovery rate. The data provided in **Figure 33** also

shows that Li^+ deintercalation is easier than intercalation at plateau regions. The fitting was performed on the five capacity recovery points. The 3.9-4.1V vs Li/Li^+ voltage oscillation recovery points were fitted with a linear equation, while the 4.1-4.3V vs Li/Li^+ was represented by an exponential decay function. These kinetics provide a basis for future mechanistic studies used to understand the influence of chemical and electrochemical interfacial reactions on the Ni-rich layered oxide degradation pathways.

4.3 Conclusions

$LiNiO_2$ is a good model system to investigate the structural stability and degradation behaviors associated with Ni-rich layered oxide materials. As unique characteristics in Ni-rich layered cathodes, phase transitions at different charging plateaus have negative impacts on battery performance metrics. The voltage oscillation experiments presented here have allowed us to determine the relative contribution of each plateau on degradation parameters such as capacity fading and Coulombic efficiency. In general, the plateaus at higher voltages create more surface side reactions leading to more severe structural distortions. Furthermore, the upper voltage plateaus have a more negative impact in Coulombic efficiency, as it takes more cycles to achieve an optimal Coulombic efficiency. Bulk-sensitive analytical methods and electrochemical testing provides a platform to deduce the interplay between $LiNiO_2$ phase transitions, electronic changes, and interfacial chemistries. Structural distortions can be induced via a mechanical effect[36], highlighting the necessity to complete the electrolyte stirring experiment to corroborate electronic changes in the pristine state before electrochemical influences. In understanding degradation behaviors of Ni-rich layered oxide materials at segmented voltage windows, it provides insight into individual reaction processes at phase transitions in this class of material.

4.4 Materials and Methods

Synthesis. $LiNiO_2$ (LNO) was synthesized via co-precipitation. A 1M metal solution of 150 mL was made with 1M $NiSO_4 \cdot 6H_2O$. The metal solution and base solution (2 M NaOH and 1.2 M $NH_3 \cdot H_2O$, total 150 mL of H_2O) were separately stored in volumetric flasks. The reaction flask was under N_2 protection. The starting solution (1 M NaOH and 1.2 M $NH_3 \cdot H_2O$, total 100 mL) was placed into the reaction flask, heated to 55 ºC and stirred continuously. The pH value was adjusted to 11.0 $\pm$ 0.2. At 2 mL/min, the metal and base solution were pumped into the starting solution. The precipitate was collected and washed copiously with DI water, followed by isopropanol. The solid material was then collected and dried under vacuum at 120 ºC. The dried precursor was mixed with LiOH (2% extra was added to compensate for Li loss) thoroughly and calcined under pure oxygen flow at 2 L/min. The sample was heated at 5 ºC/min to 460 ºC and held for 2 h. Then the sample was heated at 5 ºC/min to 725 ºC and remained there for 6 h. Finally, the furnace was cooled at 5 ºC/min to 25 ºC under oxygen flow to obtain the final pristine LNO material.

Electrochemical Testing. The $LiNiO_2$ cathode powders were processed into electrodes immediately following high temperature calcination. Acetylene carbon and poly(vinylidene difluoride) (PVDF) were stored in a humidity-controlled dry box prior to electrode preparation. The cathodes were prepared by uniformly casting the slurry (M-methyl-2-pyrrolidone as the solvent) with the active material (90 wt %), acetylene carbon (5 wt %), and PVDF (5 wt %), casted on carbon-coated aluminum foils. The cathode and Li metal anode were punched into 10 mm diameter disks. The cathodes were dried under vacuum at 120 ºC and transferred into an Ar-filled glove box. CR2032 coin cells were assembled in the glovebox using the cathode and Li metal anode, Whatman glass fiber (1827-047934-AH) as the separator, and 1M $LiPF_6$ dissolved in

ethylene carbonate (EC) and dimethyl carbonate (DMC) with a w/w 3:7 as the electrolyte. All of the cells were cycled with an electrochemical workstation (Wuhan Land Company) at 22 ºC. A fully charged cathode in 1h was defined as 1C with a corresponding specific current density of 200 mAh/g. The cyclic voltammetry (CV) testing was completed with a scan rate 0.001 V/s. The electrochemical testing window is 2.5-4.4 V vs Li/Li^+, by which the coin cell was cycled for 9 cycles. Since the first cycle is the CEI formation cycle, it is not included in the CV data reported.

Voltage Oscillation Experiments. Using the same coin cell assembly, the battery was first cycled from 2.5-4.4V vs Li^+/Li at 0.1C. After one full charge-discharge cycle, the voltage was oscillated around a 0.2V window for 100 cycles before recovering the voltage to the full cycling window. The cycling pattern was repeated and the recovered specific capacity points were compared to determine state-of-charge influences on cathode degradation.

Materials Characterization. XRD was performed on a Rigaku MiniFlex II diffractometer scanning from 10-80º at a rate of 0.5º/min. Soft XAS measurements were performed on the 31-pole wiggler beamline 10-1 at Stanford Synchrotron Radiation Lightsource (SSRL) using a ring current of 350 mA and a 1000 L/min spherical grating monochromator with a 20 µm entrance and exit slits, providing a 0.2 eV resolution. Data was acquired under ultrahigh vacuum (10^{-9} Torr) in a single load at room temperature using total electron yield (TEY) mode, in which the same drain current was collected. All the spectra were normalized by the current from freshly evaporated gold on a fine grid positioned upstream of the main chamber. Hard XAS data was acquired at the Advanced Photon Source (APS) Beamline 20-ID at Argonne National Laboratory.

CHAPTER 5: EXPLOITING ELECTRONICALLY TUNABLE LAYERED OXIDES TO UNDERSTAND SUPPORTED-AU CATALYTIC REDUCTION PATHWAYS

5.1 Introduction: Structure-Activity Trends of Supported-Au Catalytic Reactions

In modern chemistry, efficient chemical transformations are required. Catalysis is at the pinnacle of chemical conversions at the laboratory scale to industrial processes. Nanocatalysis has emerged due to its exceptional potential in conversion rates and selectivity.[229–231] Heterogeneous catalytic systems are advantageous because of the ease of separation and recovery of the catalyst.[232] Additionally, supported-metal nanoparticles have proven to be highly tunable with respect to size and morphology.[233–235]

Reducible transition metal oxides (TMO) are used as supports for precious metal nanocatalyst such as Au[236,237], Pt[238,239], and Pd[240–242]. Researchers have utilized *p*-nitrophenol reduction as a controllable reaction under pseudo first-order conditions to probe the catalytic reactivity of precious metal nanocatalysts.[243–245] Nitroaromatic hydrogenation has been studied for more than a century, but comparative catalytic activity was first suggested in 2001.[246] Nitrostyrene hydrogenation illustrated that metal oxides are able to influence the chemoselectivity of the reaction.[247,248] The reduction of *p*-nitrophenol to *p*-aminophenol is used to determine catalytic activity because the reaction does not occur without a catalyst. In the chemical industry, *p*-aminophenol is mainly used as black-and-white film developer. The reaction proceeds under ambient temperatures in aqueous media and the reaction is easily quantified using ultraviolet-visible (UV-Vis) spectroscopy.[249]

Nitrophenol reduction requires a reducing agent, such as sodium borohydride ($NaBH_4$), to proceed.[250,251,250–252] $NaBH_4$ hydrolysis produces hydrides, increasing the pH and deprotonating *p*-nitrophenol to form the *p*-nitrophenolate anion which is a yellow colored species that absorbs at λ = 400 nm.[253] The reducing agent is typically added in excess to ensure that the reaction rates can be fit to pseudo first-order kinetics, simplifying quantification. The reaction requires a catalyst to proceed. Even unsupported Au can be utilized to reduce *p*-nitrophenol.[254] Upon coupling the use of supported-Au with the reducing agent, there is potentially increased stabilization, facilitating the observed increased conversion rates.[255]

While research has shown metal oxides influence the catalytic capability of the metal nanocatalyst, the exact interplay of the two on reaction parameters such as the induction period and conversion rate are still highly debated. Key factors that are known to influence the conversion rate include the metal identity[256], nanoparticle size[257], $NaBH_4$ hydrolysis rate[241,251], reaction solution pH[256,258], and dissolved oxygen within the system[249,259–261]. In this work, layered Co-free, Ni-rich oxide material, Li_xNiO_2, is employed as a support for Au. This material was chosen due to its ease of achieving varied Ni oxidation states. By exploiting the Li^+ intercalation chemistry, typically utilized in rechargeable batteries, isostructural nickel oxides containing different ratios of Li-ions can be readily obtained to design an electronically tunable support to understand the metal oxide influences on Au catalytic capabilities for *p*-nitrophenol reduction to *p*-aminophenol.

Upon delithiation of Li_xNiO_2, the material undergoes electronic and structural perturbations due to changes in the oxidation state of Ni, the redox center. This trend can be exploited to understand how $LiNiO_2$ surface chemistry influences catalytic conversion. By incorporating an electronically tunable support material and depositing Au nanoparticles, an

understanding of the electronic influences the support has on the induction period and conversion rates can be developed.

A major feature of the *p*-nitrophenol reduction reaction is the effect of dissolved oxygen on the induction time (t_0) – a period during which no reaction occurs that can last from seconds to minutes.[260] Reaction kinetics have illustrated that with higher amounts of $NaBH_4$, the induction period becomes reduced. The interpretation of what influences the induction period is highly debated in ongoing research. Three hypothesis have been 3 highlighted in the literature. *Hypothesis 1* is that the induction period is a re-reduction of the metal nanoparticle surface. Researchers have found that the induction period disappears under inert reaction conditions.[246] Although this was reported, there are other hypothesis that refute this understanding in the literature.[261] *Hypothesis 2* suggests that the induction period is due to the diffusion of reactants, particularly *p*-nitrophenol and BH_4^-.[262] Lastly, *Hypothesis 3* states that the induction period is relative to the amount of dissolved oxygen in the solution, which can be facilitated by borohyride that can dissolve an oxide layer on the metal nanocatalyst. The reaction kinetics follow the Langmuir-Hinshelwood model.[249,260,261] Research suggested that N_2 gas could be used to purge the system of dissolved oxygen species, reducing the induction period.

While many hypotheses are suggested, many are not representative of all reaction pathways and are often negated by further research. An interplay between each hypothesis provides insights to understanding the influence of Li_xNiO_2 on the Au nanocatalyst. While the structural and electronic instability of layered Ni-rich oxide proves challenging for Li-ion battery applications, it proves favorable when developing an understanding about the role supports have in the mechanistic pathway of the reduction reaction. Materials characterization methods are used to explore the structure and electronic changes of Li_xNiO_2 before the reaction and after completion.

In doing so, structure-activity relationships were determined. Additionally, the role of the metal oxide on the conversion rate and induction period is elucidated.

5.2 Results and Discussion

Scheme 3 is a schematic highlighting the experimental proposed reaction process used for insight on the role metal oxide supports have on Au nanocatalysts. First, we employ an electronically tunable layered oxide material, $LiNiO_2$ (LNO). $LiNiO_2$, as well as other Ni-rich layered oxides are strategically synthesized to have a primary particle size of roughly hundreds of nanometers.[263] Li^+ intercalation chemistry is exploited to develop a continuum of electronic states.[90] Exactly 2 wt% of Au is deposited on $LiNiO_2$, followed by washing with water. After drying the Au/$LiNiO_2$ material under vacuum at 120 ºC, it was chemically delithiated using a strong oxidant, nitronium tetrafluoroborate (NO_2BF_4). Theoretical calculated ratios of NO_2BF_4/$LiNiO_2$ were set at 0.27, 0.54, 0.82, and 1.09, providing electronic differences to develop a structure- reactivity trend for *p*-nitrophenol reduction.

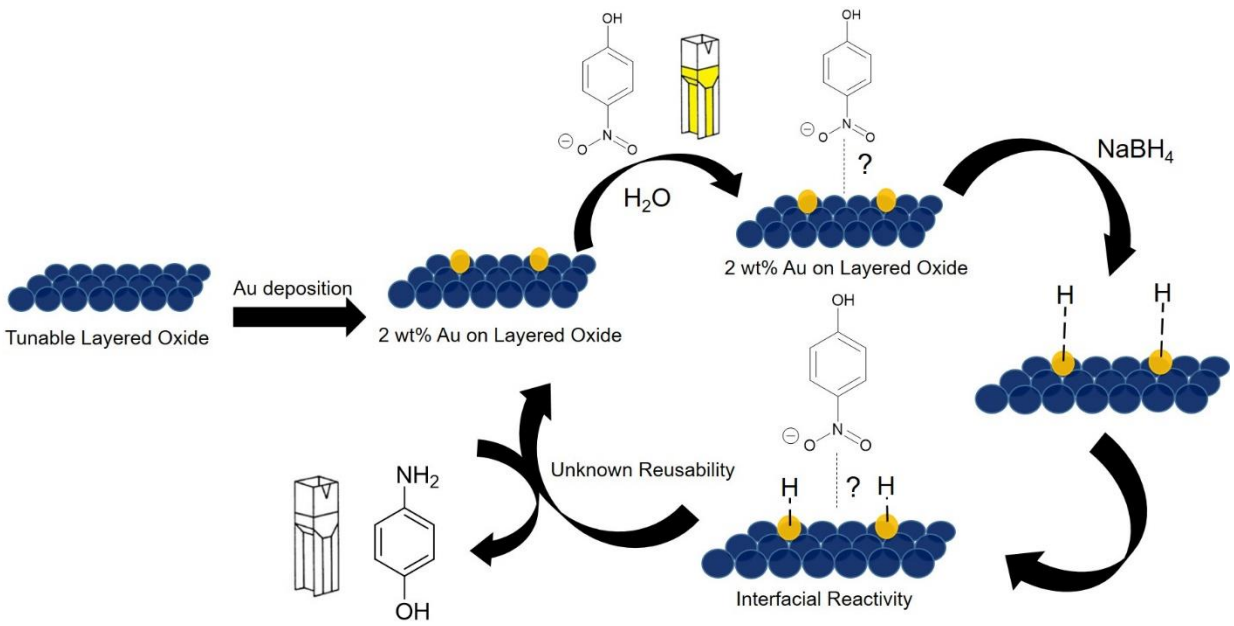

SCHEME 3: Schematic of 2 wt% Au nanocatalyst deposition on an electronically tunable layered oxide, $LiNiO_2$, followed by the proposed reaction steps that influence the induction period and conversion rate of nitrophenol reduction. In the *p*-nitrophenol reduction reaction, nitrophenol is added first, followed by small molecule ordering upon the addition of the reducing agent, $NaBH_4$ in excess. Hydrogen populates the oxidized Au surface providing a reductive environment in which the nitro- group of *p*-nitrophenol can be reduced, likely at the Au/$LiNiO_2$ interface, aided by dissolved oxygen from lattice oxygen vacancies in the support material.

Scheme 4 provides the reaction conditions used to complete the *p*-nitrophenol reduction to *p*-aminophenol. Although mechanistically many questions remain, the proposed schematic (**Scheme 3**) illustrates that a strategic method was followed to obtain reproducible results. The *p*-nitrophenol solution was added first to the reaction vessel, followed by the catalyst slurry. This allows for initial adsorption of the reactant to Au/$LiNiO_2$ catalyst. Sodium borohydride, $NaBH_4$, is added last, as the BH_4^- hydrolysis plays a key role in activating the conversion reaction. A cooperativity between oxidized states of Au and Ni reduction assist in facilitating *p*-nitrophenol reduction, likely through interfacial reactivity. Herein, the analytical techniques used to rationalize electronic

influences of $LiNiO_2$ on the Au nanocatalyst are explained. It provides further insights to its influences on the induction period and conversion rates.

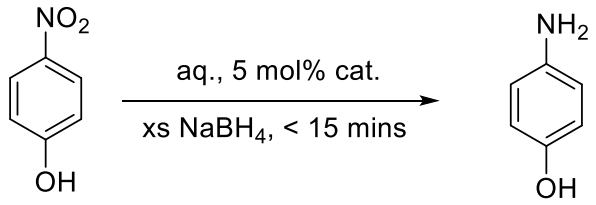

SCHEME 4: The *p*-nitrophenol reduction reaction completed in aqueous media with $NaBH_4$ as a reducing agent, added in excess. Exactly 5 mol% of the Au/$LiNiO_2$ catalyst was used for the conversion to *p*-aminophenol, which occurred within 15 minutes.

X-ray absorption near-edge spectroscopy (XANES) provides information regarding bulk orbital occupancy because X-rays penetrate into the bulk of the material to excite core electrons into the continuum. In doing so, the associated energy of the electrons can be quantified to determine the transition metal oxidation state. When comparing the pristine $LiNiO_2$ to Au/$LiNiO_2$, the oxidation state is roughly the same when reviewing the Ni K-edge edge features (**Figure 35A**).

This suggests that the Au deposition method does not affect the bulk metal oxidation states. It is important to note that electrostatic interactions between Au nanoparticles and bulk materials may influence the work function of Au. Additionally, the size of Au nanoparticles affect the work function and other electronic properties of adjacent materials.[264] The benefit of utilizing this system is that the Fermi energy is modifiable. The electronics of the support can greatly influence the work function of the Au nanocatalyst (**Figure 34**).

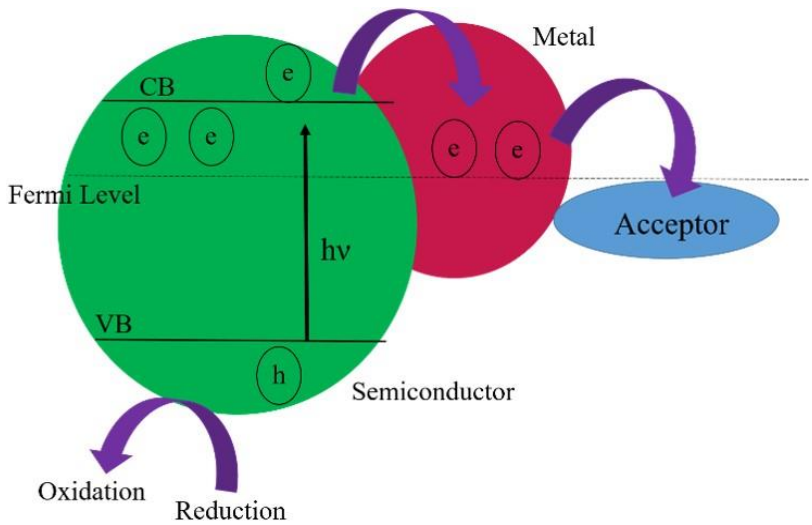

FIGURE 34: Schematic of nanocatalysts on a metal oxide support. The Fermi level is the energetic midpoint between the valence and conduction bands of the tunable metal oxide. [Adapted from Reference[265]]

While the bulk Ni oxidation state has not been changed due to the aqueous media required for Au deposition, there is minor structural distortion that has occurred, as illustrated from the extended X-ray absorption fine structure (EXAFS). Increased symmetry in layered oxide materials may be associated with the structural transition from layered to more stable phases including spinel and rocksalt.[266,267] From the EXAFS data, the interatomic distances for Ni-O and Ni-Ni do not change (**Figure 35B**). Additionally, there is no major difference in the pristine samples of $LiNiO_2$ and Au/$LiNiO_2$. This suggests that there is increased symmetry in the lattice structure after Au deposition.

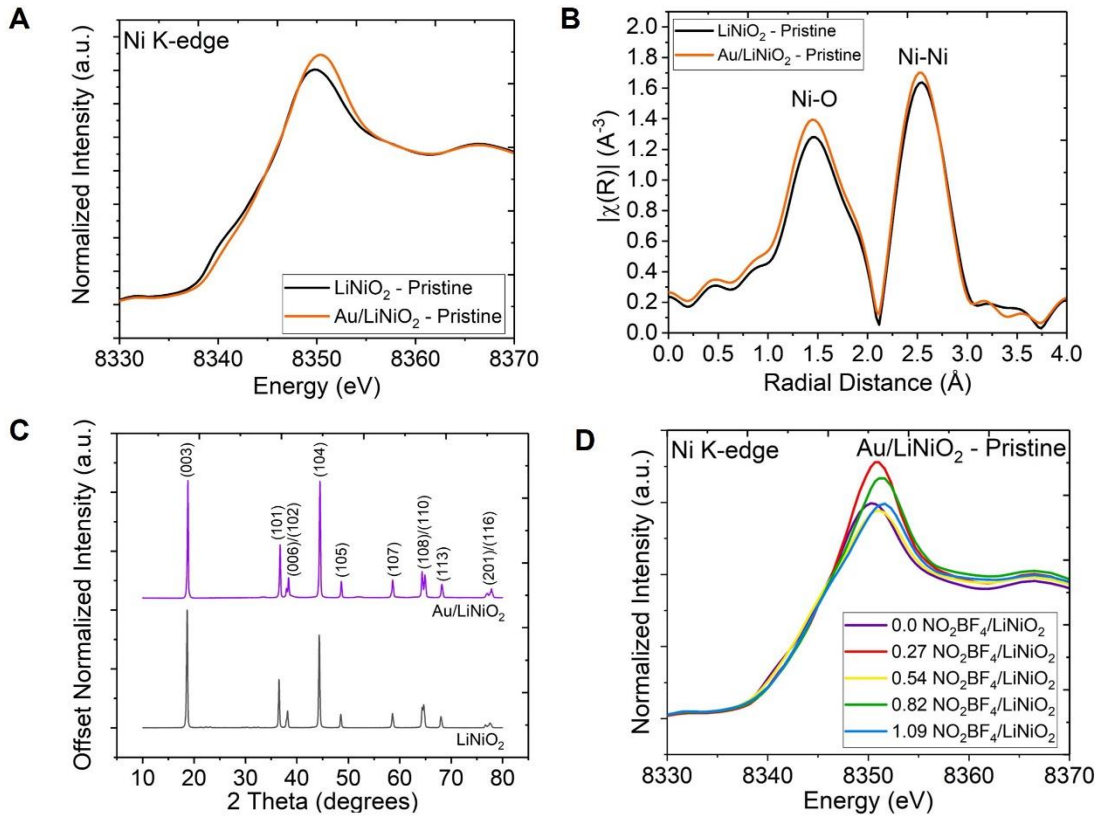

FIGURE 35: X-ray analysis for the pristine materials. **A)** Ni-K edge XANES. Au/$LiNiO_2$ has roughly the same oxidation state as the pristine $LiNiO_2$, which is Ni^{3+}. **B)** To indirectly determine the local structure changes, EXAFS was employed to highlight any structural distortion that arise from Au deposition on the $LiNiO_2$ material. **C)** The XRD pattern for the pristine $LiNiO_2$ and Au/$LiNiO_2$ is included to highlight the bulk structure of each material. The $I_{(003)}/I_{(104)}$ is 1.27 and 1.01 for $LiNiO_2$ and Au/$LiNiO_2$, respectively. After Au deposition, the bulk structure has some reconstruction. **D)** The Ni K-edge features for the Au/$LiNiO_2$ at various degrees of delithation in the pristine state are included. The ratios of NO_2BF_4/$LiNiO_2$ represent the theoretical amount of delithiation.

To ensure the phase purity of the pristine materials, X-ray diffraction (XRD) was employed to quantify the peak $I_{(003)}/I_{(104)}$ (**Figure 35C**). The (003) peak has greater intensity than the (104) peak, suggesting the bulk structure is layered and has phase purity because of the lack of NiO peaks.[268] In finalizing the pristine analysis of Au/$LiNiO_2$, XANES was utilized to ensure that there was a positive correlation between delithiation degree and Ni oxidation state. Theoretical amounts of strong oxidant, NO_2BF_4, was used to chemically delithiate the $LiNiO_2$ material, creating a

continuum of Ni oxidation states. The Ni K-edge measurements confirm that an increased degree of delithiation corresponds to increased Ni oxidation state. Although the edge energy seems very similar, there may be very small oxidation state changes. The orbital occupancy changes are better visualized by the white line energy shifts to higher energies (**Figure 35D**), suggesting some transition metal oxidation. The $NO_2BF_4/LiNiO_2$ ratios reported in the figure are associated with varied degrees of delithiation. For example, increased ratios of $NO_2BF_4/LiNiO_2$ are positively correlated to increased amounts of delithiation.

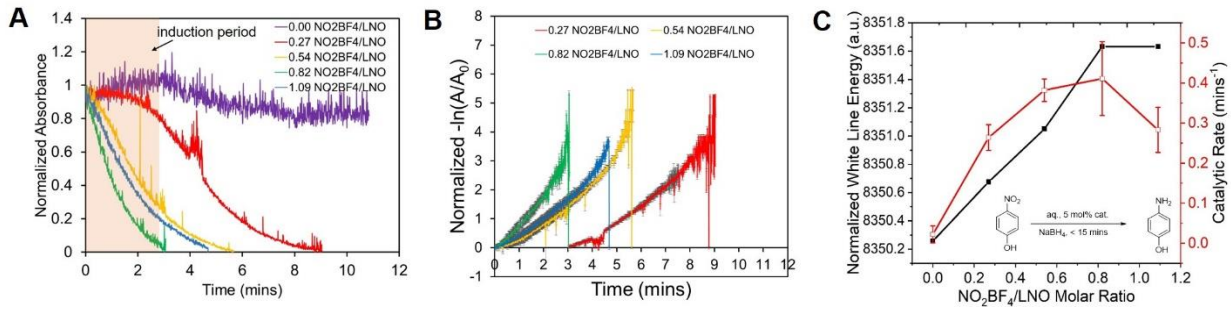

FIGURE 36: *P*-nitrophenol reduction using Au/$LiNiO_2$ and excess $NaBH_4$ monitored using UV-Vis spectroscopy at 400 nm. The $LiNiO_2$ was delithiated with 0.0, 0.27, 0.54, 0.82, and 1.09 $NO_2BF_4/LiNiO_2$ ratios. **A)** After normalization, the highlighted region denotes the induction period, which exists for the 0.0 and 0.27 $NO_2BF_4/LiNiO_2$ delithiated materials and is negligible for the other chemically delithiated degrees. **B)** Conversion rates were quantified by using pseudo first-order reaction kinetics and are denoted as 0.0193 min^{-1} with no catalyst present. The $NO_2BF_4/LiNiO_2$ ratios of 0.0, 0.27, 0.54, 0.82, and 1.09 had rates of 0.1615 min^{-1}, 0.6597 min^{-1}, 0.7436 min^{-1}, 1.1030 min^{-1}, and 0.7013 min^{-1}, respectively. **C)** A trend between structure and activity is highlighted when plotting trends between the pristine white line energy from the Ni K-edge and the catalytic rate for each of the delithiated materials. There is a positive trend between delithiation degree, pristine Ni oxidation state, and catalytic conversion rate.

The *p*-nitrophenol reduction reaction was monitored *in situ* using UV-Vis spectroscopy in absorbance mode. The reaction was completed under pseudo first-order kinetics with $NaBH_4$ added in excess with 5 mol% of the Au/$LiNiO_2$ catalyst (**Scheme 4**). When sodium borohydride undergoes hydrolysis, the solution pH increases and *p*-nitrophenol is deprotonated to form the nitrophenolate anion[249] which has an absorbance intensity at λ = 400 nm. By monitoring the absorbance wavelength, conversion rates were quantified. An excess amount of BH_4^- removes the oxidation layer of the support.[246]

First, absorbance versus time data was plotted (**Figure 36A**), illustrating that there is a plateau feature found in the 0.0 and 0.27 $NO_2BF_4/LiNiO_2$ samples. The highlighted region found in this samples is associated with an induction period that occurs for roughly 3 minutes, followed by reactant conversion to products. The remaining samples, 0.54, 0.82, and 1.09 $NO_2BF_4/LiNiO_2$ have no induction period and increased conversion rates. Utilizing the pseudo first-order reaction

kinetics, the data was fitted with a linear regression and the conversion rates are represented by the slope of the linear equation (**Figure 36B**). When no catalyst was used, there was almost negligible amounts of conversion with a rate of 0.0193 min^{-1} and very little color change of the reaction solution. The $NO_2BF_4/LiNiO_2$ ratios of 0.0, 0.27, 0.54, 0.82, and 1.09 had conversion rates of 0.1615 min^{-1}, 0.6597 min^{-1}, 0.7436 min^{-1}, 1.1030 min^{-1}, and 0.7013 min^{-1}, respectively. There is a positive correlation with increased $NO_2BF_4/LiNiO_2$ ratios, although the relationship deviates at the highest delithiated state (**Figure 36C**). This may be caused by the electronic and structural fragility found in Ni-rich layered oxide materials. The structural fragility leads to a rearrangement of the material from layered to rocksalt, common to Ni-rich layered oxide materials at high degrees of delithiation.[30,168,269] The structural rearrangement perturbed the electronic configuration of the TM*3d*-O*2p* hybridization, leading to decreased amounts of dissolved oxygen in solution that can be used to facilitate sodium borohydride hydrolysis. The structure-reactivity trends highlighted in **Figure 36** assist in determining the role of the support in the overall reduction mechanism.

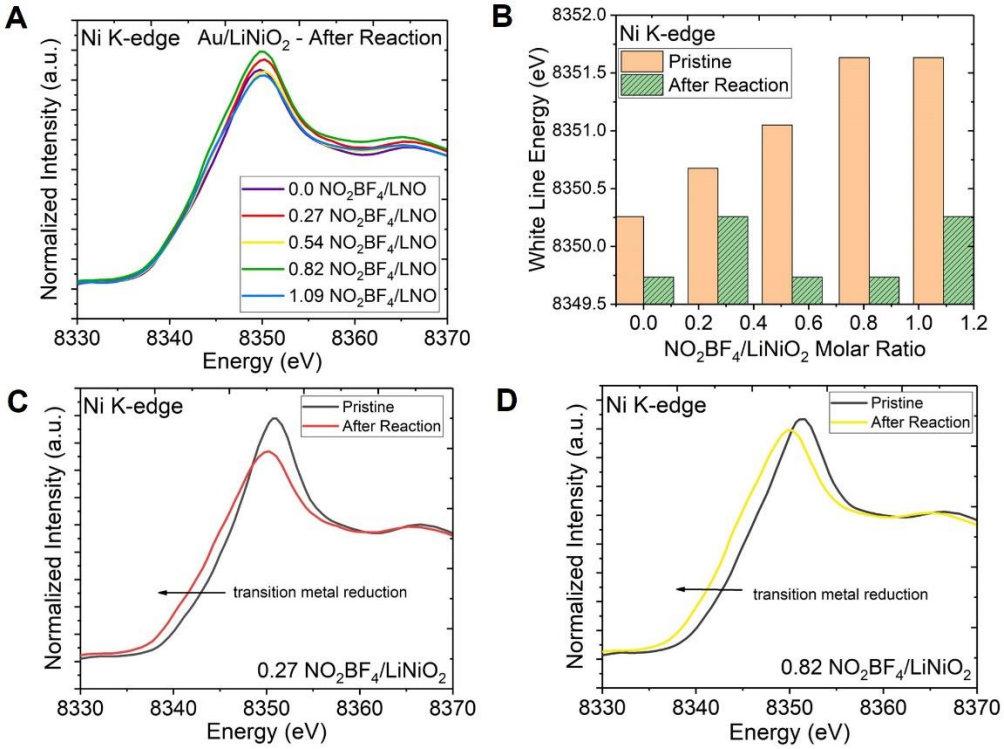

FIGURE 37: XANES and EXAFS features for Au/$LiNiO_2$ after the reaction. **A)** The Ni K-edge for Au/$LiNiO_2$ for 0.0, 0.27, 0.54, 0.82, and 1.09 NO_2BF_4/$LiNiO_2$ ratios illustrate that there is Ni reduction to roughly the same oxidation state, as shown by the white line energy features. **B)** To correlate a relationship between NO_2BF_4/$LiNiO_2$ molar ratios and the white line energy, when comparing the pristine and after the reaction there is Ni reduction. Taking a closer look at the **C)** 0.27 and **D)** 0.82 NO_2BF_4/$LiNiO_2$ samples in the pristine and after reaction, further illustrates the transition metal reduction.

When looking Li_xNiO_2 Ni K-edge after the reduction experiment was completed, the edge features show Ni metal reduction for each of the delithiated states (**Figure 37A**). For each of the Au/$LiNiO_2$ 0.0, 0.27, 0.54, 0.82, and 1.09 NO_2BF_4/$LiNiO_2$ molar ratios, the Ni oxidation state is roughly the same. This suggests that there is a similar electron transfer pathway for each of the materials regardless of the pristine oxidation state. A histogram is included to highlight the pristine and after reaction white line energy, illustrating transition metal reduction for each of the Au/$LiNiO_2$ samples (**Figure 37B**). Comparing a sample with an induction period versus the highest performing material, the 0.27 (**Figure 37C**) and 0.82 (**Figure 37D**) NO_2BF_4/$LiNiO_2$ molar

ratios, illustrates that for both samples there is a Ni K-edge edge shift towards lower energy. This left-most shift suggests that there is Ni metal reduction.

X-ray photoelectron spectroscopy (XPS) is used to determine the local chemical environment changes in a material (**Figure 38**). For the delithiated Au/$LiNiO_2$ samples, the Ni2p and Au4f binding energy would provide the most information to determine the surface chemistry that is occurring during the *p*-nitrophenol reduction reaction pathway. To prepare the XPS samples, exactly 5 mol% of Au/$LiNiO_2$ was reacted with nitrophenol and $NaBH_4$ for 15 minutes to emulate the reaction conditions illustrated in **Scheme 4**.

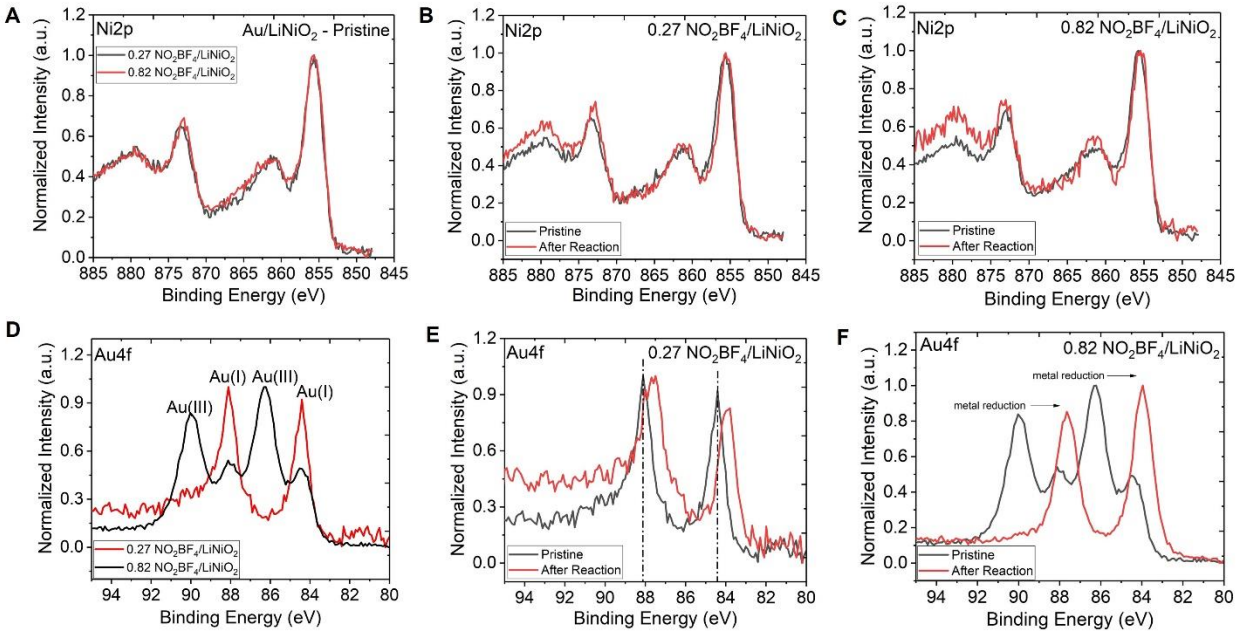

FIGURE 38: XPS Ni2p of **A)** the pristine 0.27 and 0.82 $NO_2BF_4/LiNiO_2$ delithiated material, illustrating no changes in local bonding structure. This suggests that the surface-most Ni oxidation state is the same for both materials. The Ni2p data for **B)** 0.27 $NO_2BF_4/LiNiO_2$ and **C)** 0.82 $NO_2BF_4/LiNiO_2$ material in the pristine state and after the completion of the reaction shows no peak shifting, suggesting that the surface oxygen becomes stabilized during the preparation of the Au/LNO material. The XPS Au4f of **D)** the pristine 0.27 and 0.82 $NO_2BF_4/LiNiO_2$ material, illustrating the presence of Au(I) for the 0.27 $NO_2BF_4/LiNiO_2$ and both Au(I) and Au(III) for the 0.82 $NO_2BF_4/LiNiO_2$ material. **E)** The 0.27 $NO_2BF_4/LiNiO_2$ pristine and after reaction material shows peak shifting to lower binding energies, highlighting Au reduction from Au(I) to Au(0). **F)** The 0.82 $NO_2BF_4/LiNiO_2$ pristine material corresponds to Au(I) and Au(III) peaks. After the completion of the reaction, Au(0) is present.

Two samples were analyzed for XPS that are representative of the entire delithiated series. Typically, increased Ni oxidation states are depicted as higher binding energies.[217] The Ni2p XPS features for the material before reaction at the 0.27 and 0.82 delithiated Au/$LiNiO_2$ (**Figure 38A**) show that the four peaks show no shifts in the binding energy, suggesting that the surface most Ni local chemical environment has not been perturbed. This corroborates that Au on the surface is not electronically bound to Ni because there are not changes in the Ni2p binding energy. Even upon the completion of the *p*-nitrophenol conversion reaction for both 0.27 $NO_2BF_4/LiNiO_2$ (**Figure 38B**) and 0.82 $NO_2BF_4/LiNiO_2$ (**Figure 38C**) Au/LNO materials illustrate no peak shifting for both the Ni $2p_{3/2}$ and Ni $2p_{1/2}$ peaks. This suggests that the material before and after the reaction has very stable surface oxygen since the Ni*3d*-O*2p* hybridization directly influences the Ni oxidation state. If the oxygen was not stable and subjected to surface lattice oxygen loss, the Ni oxidation state would decrease and shifts in the Ni2p binding energies would be evident. To establish an interplay dynamic between Ni and Au, XPS was employed to determine the local chemical environmental perturbations for Au4f (**Figure 38D-F**).

The pristine 0.27 and 0.82 $NO_2BF_4/LiNiO_2$ Au/LNO materials were plotted first to analyze the initial Au4f XPS features. **Figure 38D** shows that the 0.27 $NO_2BF_4/LiNiO_2$ Au/LNO shows the presence of Au(I), illustrated by the peaks found at ~ 84.5 and 88 eV. The same Au(I) peaks are evident in the 0.82 $NO_2BF_4/LiNiO_2$ material, although there is an additional peak at ~86.0 and 90.0 eV corresponding to Au(III). While Au is considered to be inert, high delithiated states seem to activate higher oxidation states of Au. By completing pre- and post-mortem studies for the 0.27 $NO_2BF_4/LiNiO_2$ (**Figure 38E**) the peak has a right shift towards lower binding energies. This suggests that there is Au metal reduction from Au(I) to Au(0). Upon analyzing the 0.82 $NO_2BF_4/LiNiO_2$ Au/LNO material (**Figure 38F**), the pre- and post-mortem material begins with

both Au(I) and Au(III) present, but after the reaction only Au(0) is present. This may justify why higher delithiated materials have increased reaction rates. If the support can directly oxidize Au to facilitate in increased electron transfer, the conversion rates can be influenced by the interplay between Au and the $LiNiO_2$ support electronics.

5.3 Conclusion

To summarize, the data reported describes novelties of electron transfer pathways that occur at the interphase of the Au/$LiNiO_2$ catalyst for *p*-nitrophenol reduction to *p*-aminophenol. By employing an Li_xNiO_2 as an electronically tunable support, XAS, XRD, XPS, and UV-Vis were used to develop structure-activity relationships that are often debated. Studying the pristine material and the recovered material after the reaction, we found that there is a direct correlation between Ni oxidation state in the material, conversion rates, and time duration of the induction period. By probing the bulk Ni oxidation state using XANES, we report that after the reaction the Ni oxidation state becomes reduced. While XANES highlights bulk oxidation state changes, it additionally provides detailed information about the bulk and surface interplay of the metal oxide material and how each independently influence the supported-Au nanocatalyst. XPS was employed to determine the surface chemical bonding changes. The data illustrates that higher degrees of delithiation, such as 0.82 $NO_2BF_4/LiNiO_2$ are associated with Au(III), whereas lower delithiated states, such as 0.27 $NO_2BF_4/LiNiO_2$ can only oxidize Au to Au(I). This is positively correlated to the conversion rate. After the reaction, Au(0) is present. Based on the data collected and reported herein, an experimental proposed reaction scheme was presented to provide insights into the role transition metal oxide supports have on the Au nanocatalyst. While more future work is required to determine distinct reaction mechanisms for *p*-nitrophenol reduction, we hope this

work provides a buildable platform for future studies to understand the interplay of metal oxides and precious metal nanocatalyst.

5.4 Materials and Methods

Synthesis. $LiNiO_2$ (LNO) was synthesized through a co-precipitation method in a flask. A 1 M metal solution of 150 mL was mixed into 1 M $NiSO_4 \cdot 6H_2O$. The metal solution and base solution (2 M NaOH and 1.2 M $NH_3 \cdot H_2O$, total 150 mL of H_2O) were separately stored in volumetric flasks. The reaction flask was under N_2 protection. The starting solution (1 M NaOH and 1.2 M $NH_3 \cdot H_2O$, total 100 mL) was placed into the reaction flask, heated to 50 ºC and stirred. The pH value was adjusted to 11.0 ± 0.2. The metal and based solutions were pumped into the starting solution at approximately 2 mL/min. The precipitate was collected and washed using DI water, followed by isopropanol. A filtrate was collected and dried in a vacuum oven overnight at 120 ºC. The dried precursor was mixed with LiOH (2% extra was added to compensate for Li loss) thoroughly and calcined under pure oxygen flow at 2 L/min. The sample was heated at 5 ºC/min to 460 ºC and held for 2 h. Then the sample was heated at 5 ºC/min to 675 ºC and remained there for 6 h. Finally, the furnace was cooled at 5 ºC/min to 25 ºC under oxygen flow to obtain the final pristine LNO powder.

Au Deposition. Au was deposited on LNO by first dispersing LNO in water. Exactly a 2 wt% of Au was added using a 0.0048M $HAuCl_4$ solution. The LNO/$HAuCl_4$ solution was stirred and heated at 95 ºC until the solution was evaporated to 20% of the starting solution volume. The material was dried under vacuum at 120 ºC.

Chemical Delithiation. $LiNiO_2$ (LNO) was synthesized using the method described above. To prepare the various chemically delithiated samples, the pristine powder was mixed with the

oxidant (0.05M NO_2BF_4 in acetonitrile) using stoichiometric ratios of 0.0, 0.27, 0.54, 0.82, and 1.09 $NO_2BF_4/LiNiO_2$ molar ratios. The mixture was stirred on the benchtop for 24 hours before centrifuging. The powder was washed with pure acetonitrile three times to remove undesired species due to the oxidant. The powder was dried in a vacuum oven at 120 ºC with limited air exposure.

Nitrophenol Reduction. A 0.2mM aqueous solution of *p*-nitrophenol was prepared and 1mL of solution was added to the cuvette. For the aqueous solution, 0.9 mL of H_2O was added to the solution. A catalyst slurry with a density of 1.18 g/L was added to the nitrophenol solution, in which 0.8 mL of slurry was added. Exactly 0.30 mL of a 0.132M $NaBH_4$ aqueous solution was added to the reaction cuvette. Absorbance measurements were completed using UV-Vis spectroscopy.

CHAPTER 6: CONCLUSIONS – LAYERED OXIDE CATHODE STRUCTURAL AND ELECTRONIC INFLUENCES ON SURFACE CHEMISTRY AND OTHER PHYSICAL PROPERTIES

6.1 Conclusions

Ni-rich layered oxide materials are continuing to gain interest as a frontier material due to its high theoretical capacity and specific energy. Portable electronic devices and electric vehicles are catapulting the demand for improved oxide cathode design and materials chemistry to enhance the current development of materials for lithium battery applications. **Chapter 1** provided a review of the chemistries associated with layered oxide materials. In designing experiments to understand the surface chemistry of Ni-rich layered oxides, various analytical methods were utilized. **Chapter 2** provided detail about the analytical methods and their associated working principles. **Chapters 3-5** described the technical experimental findings to develop fundamental platforms to understand oxide cathode degradation pathways and how to employ the chemistry in catalytic applications.

6.1.1 Understanding Surface Reconstruction in NMC622

Surface reconstruction is common in layered transition metal oxide materials. This structural fragility is magnified in Ni-containing materials due to the ease of electron transfer pathways due to TM*3d*-O*2p* orbital hybridization. Herein this dissertation, we developed a model platform to study the mechanism in which lattice oxygen loss occurs. In **Chapter 3**, we utilized

benzyl alcohol oxidation as the model reaction to probe the surface of $LiNi_{0.6}Mn_{0.2}Co_{0.2}O_2$ (NMC622) to determine the mechanistic pathway in which electrons and oxygen transfer. To understand the mechanism of lattice oxygen loss, materials characterization techniques including X-ray absorption spectroscopy (XAS), X-ray photoelectron spectroscopy (XPS), X-ray diffraction (XRD), and electrochemical testing methods were coupled with quantitative GC-FID studies. In doing this, we developed a structure-activity relationship while decoupling the bulk and surface electronic and structural properties.

In the study, we determined that there was a positive relationship between delithiation degree and benzyl alcohol oxidation under oxidative and inert environmental conditions. This suggested that lattice oxygen loss is irreversible and is likely loss to oxidizable electrolytic species. Surface and bulk chemistries were decoupled by using soft-XAS and XPS to investigate the surface-most electronic and chemical bonding. The bulk chemistries were analyzed using hard-XAS and XRD to determine electronic and structural changes.

After corroborating all of the information obtained during the experiments, the mechanism of lattice oxygen loss occurs by deprotonation of benzyl alcohol, followed by chemisorption at the metal cation side of NMC622. There is β-hydride elimination followed by the generation of water generation, facilitating the lattice oxygen loss. This reaction assists in understanding the interplay between lattice oxygen loss and transition metal reduction, promoting surface reconstruction in layered Ni-containing materials.

6.1.2 Structural and Chemical Evolution at Phase Transitions

During the transition toward minimal-Co and Co-free cathode materials, the structural fragility of Ni-rich layered oxide materials impedes the commercialization of this class of

materials. Most of the concern derives from battery safety. Thermal decomposition of Ni-rich layered oxide material tends to undergo exothermic reactions with flammable, carbonate-containing liquid electrolytes. To mitigate these concerns, this dissertation develops a novel voltage oscillation experiment to quantify oxide cathode degradation at the phase transitions. **Chapter 4** greatly discusses the charging plateaus associated with $LiNiO_2$ and probes the chemical and electrochemical degradation pathways.

The technical data included electrochemical testing, coupled with XAS and EXAFS. The voltage oscillation experiment provided a platform to minimize the amount of Li^+ reaction, decreasing electrochemically promoted interfacial reactions. This allows for greater insight into the chemical reactions that occur at the phase transitions. By oscillating around the latter two phase transitions, largely associated with cation mixing and lattice oxygen loss, capacity recovery points were used to quantify cathode degradation. The M → H2 has linear degradation, whereas the H2 → H3 phase transition undergoes degradation with exponential decay fitting. Additionally, the voltage oscillation electrochemical testing method generates a means to understand the number of cycles required to recover optimal Coulombic efficiency.

6.1.3 Electronically Tunable Oxides for Catalytic Applications

Chapter 5 of this dissertation discusses a means to utilize layered transition metal oxides in another application, catalysis. The role of the transition metal on metal nanocatalysts is greatly misunderstood. In this dissertation, an experimental schematic of the reaction was proposed to summarize the results from the conversion rates, coupled with XANES and XPS. By utilizing these techniques, a structure-activity relationship was developed. XPS highlighted that the delithiated material with higher Ni oxidation state was able to provide Au(III), whereas lower Ni

oxidation states only allowed for Au(I). The electronics of the support can influence the electronics of the Au nanocatalysts, leading to changes in the conversion rates. While there are many questions surrounding *p*-nitrophenol reduction mechanism and the influences the supported-Au has on key factors such as the induction period, this work provides a unique platform to understand these nuances.

CHAPTER 7: THE FUTURE OF NI-RICH OXIDE CATHODES AND THE STRATEGIES TOWARDS A SUSTAINABLE FUTURE IN BATTERIES

7.1 Future Directions for Ni-rich Layered Oxide Materials

Ni-rich layered oxide materials are extremely important in the energy transition. This dissertation describes a few of the key aspects associated with the challenges of commercializing Co-free, Ni-rich layered oxides. Many of the challenges are associated with structural fragility, facilitated by lattice oxygen loss and cathode-electrolyte interfacial reactions. A detailed summary of the technical work provided in this dissertation is described in **Chapter 6**. **Chapter 7** provides a discussion on the future directions for understanding the surface chemistry of this class of materials. Additionally, this chapter discusses other oxide cathode designs for applications in lithium batteries and catalysis. This chapter provides insights into the global perspective of energy storage and sustainability.

Chapter 3 describes how the electronic and structural degradation of Ni-rich layered oxides can be elucidated by borrowing techniques from the field of catalysis. The work utilizes a probing molecule, benzyl alcohol, to understand the surface chemistry of Ni-containing layered oxides. In doing so, oxygen and electron transfer pathways are predicted to explain electronic perturbation and structural rearrangement in the metal oxide material. Novel, creative Ni-rich layered oxide cathode designs are conceived regularly by incorporating various metal dopants, coatings, and alternative synthesis methods. While new materials are constantly being developed, there are complex chemistries that impede a detailed understanding of the cooperativity found in battery systems. In particular, it complicates understanding the surface chemistry at the

oxide cathode-electrolyte interphase. Additionally, crosstalk between the cathode and anode can influence the overall structural fragility of the Ni-rich layered oxide material. Each of these competing chemistries must be decoupled to understand how they independently and collaboratively influence battery performance metrics, including capacity fading, Coulombic efficiency, energy density, and cycle life.

Decoupling surface and bulk chemistries provide a platform towards improved material design. The degree of oxygen instability is fundamental in understanding the structural fragility of Ni-rich layered oxide materials. Atomic interactions between the oxide cathode and electrolytic species cause a significant amount of the structural degradation in the material. While electrolyte molecules are complex, they can be modified to explore the surface properties of Ni-rich layered oxides. This is key in elucidating the fundamental interactions between electrolyte solvents and $LiNiO_2$ analogs.

To predict oxygen stability in other cathode materials, small molecule probing strategies described in **Chapter 3** can be used. While in this work benzyl alcohol was used for surface probing, there are other molecules that may prove to be insightful to advance the current knowledge-base.

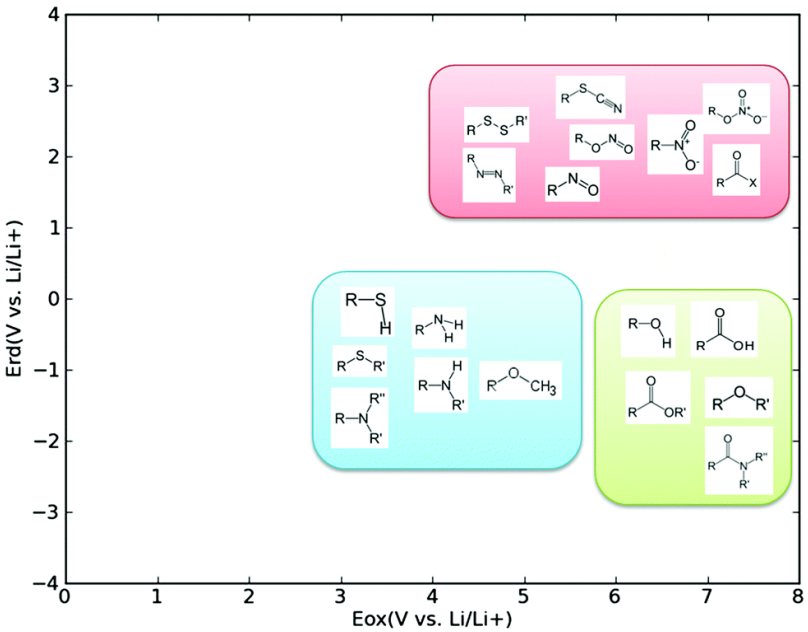

FIGURE 39: Various organic functional groups on the redox potential plane, highlighting the effective range of oxidation and reduction potentials for each group vs Li/Li^+. [Taken from Reference[270]]

Park and coworkers developed an understanding of various organic functional groups by determining their oxidation and reduction potentials versus Li/Li^+ (**Figure 39**).[270] While the molecules highlighted in **Figure 39** were developed as organic electrolyte additives for various battery applications, some of them are suitable for probing the surface chemistry of fragile oxide cathode materials. Molecules with an $E_{ox} > 4.5V$ vs Li/Li^+ are stable during cycling of the active material which typically has an upper cutoff voltage of 4.4V vs Li/Li^+. The molecules with an $E_{ox} < 4.5V$ vs Li/Li^+ will be similar to electrolyte solvents that are unstable during cycling. A range of molecules will provide insight about how the surface reacts to different probing molecules with varying redox potentials. Additionally, it is valuable to understand how electrolyte solvents can be modified for improved electrode-electrolyte interactions.

Modifications can be made to the probing experiment described in **Chapter 3**. In this dissertation, only NMC622 was employed as a platform for determining a mechanism for lattice

oxygen loss. To expand the surface chemistry probing study, a trend between Ni content and lattice oxygen loss and surface reconstruction can be determined. Analyzing materials with 60-100% Ni content will lead to different trends in electronic and structural changes with different small molecules for surface probing. Similar materials characterization techniques can be used to determine changes to the material post-probing. XPS can provide local bonding changes, especially in the O1s and the TM2p spectra. Bulk structural changes are mostly illustrated by XRD. HOMO-LUMO energy levels and its relative position to the oxide cathode sample would provide great insights into thermodynamically favorable electron transfer pathways.

In cases where the probing molecule is volatile, gas chromatography is a rapid, accurate testing method to determine oxidation products generated after lattice oxygen loss. The challenge with many of the small molecules with $E_{ox} > 4.5V$ vs Li/Li^+ is similar to that of electrolytic species – volatility and viscosity. In this case, nuclear magnetic resonance (NMR) studies may prove to be insightful. Isotope studies are useful to determine oxygen transfer between the oxide cathode and the small molecule, similarly to what has been completed in other studies[271–275] to determine electrolyte decomposition products, oxide cathode material degradation, and electrode – electrolyte interfacial components. By incorporating ^{18}O into the oxide cathode structure, if there is any oxygen transferred from the cathode to small molecule, NMR could detect the presence of ^{18}O in the reaction products after oxidation. A time-dependent probing study would be insightful upon integrating ^{1}H, ^{17}O, and ^{13}C NMR peaks to quantify the amount of small molecule oxidation over time. At the completion of the probing experiment, the material can be recovered for analysis. TEM is useful to determine the surface reconstruction thickness changes before and after the probing experiment. Additionally, STEM can illustrate the degree of metal cation mixing and XRD can corroborate the result by providing $I_{(003)}/I_{(104)}$ and Rietveld refinements, representing the

bulk structural changes. Probing experiments serve as an accelerated method to determine electrode degradation that is generated by lattice oxygen instability.

Chapter 4 in this dissertation describes the voltage oscillation experiment, a novel method, to determine the influence chemical and electrochemical reactions have on the structural degradation behaviors at the phase transitions of $LiNiO_2$, specifically M → H2 and H2 → H3. The voltage oscillation experiments can be used to rapidly examine oxide cathode-electrolyte compatibility. Significant focus has been geared toward the development of high energy density, structurally robust cathode materials. Nevertheless, the design of improved electrolyte systems is also underway.

Liquid-based electrolyte decomposition is largely the cause of thermal runaway and catastrophic safety concerns, such as battery fires and explosions. A detailed discussion on electrolyte decomposition products is summarized in ***Section 1.2***. Many researchers still debate the exact role electrolytic species and their decomposition products have on oxide cathode degradation and overall battery performance metrics.[164,276,277] The aforementioned voltage oscillation experiment in **Chapter 4** provides insights into understanding how electrochemical and chemical reactions that occur at the oxide cathode – electrolyte interphase lead to different degradation behaviors.

The benefit of the voltage oscillation experiment is that it suppresses the degree of Li intercalation/deintercalation in the material by oscillating around a 0.2V window. Electrochemical reactions are minimized. Nevertheless, the fading behaviors associated with the M → H2 and H2 → H3 phase transitions can be complex, as illustrated by the trends in the capacity recovery data. A major factor of specific capacity fading is internal resistance in the cell. To understand the role of internal resistance, electrochemical impedance spectroscopy (EIS) is an excellent tool to use.

At each of the voltage oscillation recovery points, an EIS test can be completed to illustrate the resistance of the cell. By plotting the resistance with respect to each of the capacity recovery points, there can be an improved understanding of the role surface reconstruction has on the cathode degradation behavior.

After performing the voltage oscillation experiments and EIS testing, soft-XAS can provide useful in understanding the surface electronic changes. By obtaining the oxidation state changes at each of the capacity recovery points, a decrease in oxidation state should be present. The degree of transition metal reduction should correlate to the amount of structural degradation in the material. These additional characterization methods can enhance the current conclusions provided in this dissertation, alleviating more of the debates surrounding the impact of electrolyte decomposition on oxide cathode degradation.

The National Renewable Energy Lab, the Department of Energy, as well as national labs and universities, have started to ponder methods to provide a second-life to rechargeable batteries.[278] While second-life options are still to be discovered, herein this dissertation we exploiting the electronic tunability of Ni-rich layered oxide materials to understand surface and interfacial chemistries of Au nanocatalyst and metal oxide supports. **Chapter 5** describes the experimental methods used to explore how $LiNiO_2$ is a tunable support for Au. Au/$LiNiO_2$ is used to convert *p*-nitrophenol to *p*-aminophenol via a reduction mechanism. The role of metal oxides on precious metal nanocatalyst remain under debate. Advancing the experimental methods designs in **Chapter 5**, more surface analytical techniques can be employed to understand the changes at the surface of the material. For example, XPS is suitable for understanding the local chemical bonding environment changes before and after the reaction. To expand the electronic study of the material, before and after the catalytic reaction is complete, soft-XAS can be used in AEY and

TEY modes to understand the transition metal oxidation state changes. The reaction occurs at the surface-most of the material. There are likely electronic changes at the surface that facilitate the electron transfer from the Au nanocatalyst to the tunable metal oxide support.

Many researchers highlight that the reducibility of the support material can greatly influence the induction period. To explore this concept further, a continuum of reducible to irreducible supports can be utilized to develop a reliable trend in induction period of surface reducibility. One way to perform this experiment is to explore a variety of Ni-containing layered oxide materials, such as NMC532, NMC622, NMC811, as well as irreducible supports such as SiO_2. Surface analysis, including XPS and soft-XAS are important in determining an understanding of how local chemical bonding and oxidation states influence the induction period and conversion rates. Strong metal – support interactions are continually under debate and the work provided in this dissertation only addresses a fraction of the ongoing questions.

The future directions provided in ***Section 7.1*** are not exhaustive, as consumer demand, niche markets, and the energy revolution continues to power a need for constant growth in understanding the chemistries that drive many oxide cathode synthesis and degradation processes. The complexities found within battery systems will continue to grow until fundamental concepts are well-understood amongst the battery research community and beyond. The following sections found in **Chapter 7** are written to provide a broader perspective on the future of lithium batteries and the role they have in catapulting a sustainable future and environmentally improved world.

7.2 The Future of Lithium Batteries

Since 1913 when Gilbert Newton Lewis discovered[279] that lithium had the ability to exist as a Li^+ solvated by an electron, the potential for the usages of Li-ions has continued to accelerate.

Pre-existing battery chemistries, such as lead-acid and Nickel Metal Hydride (NiMH), are inferior to Li-ion intercalation chemistry. In comparison to Ni-Cd batteries, voltages in Li-ion batteries are roughly three times more. While Li-ion batteries suffer from self-discharge, it is roughly 4 to 6 times less than Ni-Cd and Ni-MH batteries.[280] Because of the ongoing advantages of Li-ion batteries, research in industry and academia has continued to grow.

As Li-ion batteries are gaining momentum for high energy and power density requirements, Li metal anode usage has gained attention. Lithium has a potential of -3.04V vs SHE making it the most electropositive element. Metallic Li was first pioneered by Stanley Whittingham in the 1970s, and by the 1980s Moli Energy commercialized the first Li metal battery with a MoS_2 cathode.[281] Although Li metal anodes are on the horizon, there are safety challenges associated with the hindrance of it becoming viable technology for the progressive energy storage market. Dendrite formation in Li metal batteries leads to poor cyclability, low Coulombic efficiency, and an increase in the over-potential, leading to capacity fading during cycling. Li metal anodes are still underway; nevertheless, a significant amount of research is focused around furthering the innovation of cathode design.

Cathode chemistry is at the pinnacle of battery cycle life, enhanced capacity and Coulombic efficiency, and improved safety. Li-based cathode materials are continuing to grow in demand as the globe continues to transition towards clean, renewable energy sources. Additionally, there is a constant growth in portable electronic devices, such as laptops, smart watches, cellular devices, and even sharp rises in electric vehicle technologies.

Section 7.2 of this chapter will discuss the advancement of other battery materials, including the rise of interest in Li-rich layered oxides, Li/Mn-rich layered oxides, disordered rocksalt materials, as well as sodium- and magnesium-ion batteries. As we continue to drive clean

energy and sustainability for future generations, there is an ongoing need to discuss the environmental impact that the energy revolution is influencing. ***Section 7.3*** will greatly discuss the role of batteries in a sustainable future and how battery material design innovation should cultivate the global desire for negative carbon emissions.

7.2.1 Advancing Ni-rich Oxide Cathode Design

Creative innovation is required for advancing Ni-rich layered oxide cathode design for improved development of lithium batteries. In designing a cathode material, there are a few requirements necessary for superiority. The material needs to be 1) low cost and environmentally friendly, 2) possess high specific energy and power densities for the continually growing industry, 3) have high Li^+ and electronic conductivity, 4) be structurally robust and reversible during lithiation and delithiation, limiting the amount of volumetric change during charge and discharge cycles, 5) be chemically inert towards electrolytic species, minimizing the amount of undesirable CEI reactions, and 6) have high thermal stability.

As highlighted in the previous chapters of this dissertation, Ni-rich layered oxide materials have gained much attention because of its abilities as a high energy density material. There is a lot of structural instability found in Ni-rich layered oxide cathodes which is why high Ni content materials have ongoing struggles towards commercialization. One method to mitigate Ni-rich layered oxide materials is to develop coating strategies. Coating strategies are used to minimize undesirable interfacial reactions that lead to battery performance degradation. Detailed surface coating strategies are discussed in depth in ***Section 1.3.1***.

Nickel is a metal that is not found in substantial amounts in the earth's crust. One strategy towards developing high energy materials that highly structurally reversible is to coat the materials

with other Li-based oxides that contain structural robustness, do not hinder Li^+ transport kinetics, and lacks detrimental electron transfer pathways with electrolytic species. By stabilizing the interfacial chemistries that occur within lithium batteries, there will likely be more stability on the anode side as well. The crosstalk between the cathode and anode is extremely important in designing a superior battery.

7.2.2 Other Materials Used Toward Innovative Cathode Design

Oxygen redox in layered oxide material was first accepted in the early 2000s[282–284], before there was significant studies regarding the reversible oxygen redox in other fragile metal oxide materials.[32] The challenge to oxygen redox materials is the structural fragility, similar to that found in Ni-rich layered oxides. Li/Mn-rich layered oxides have gained attention due to their high energy density for Li-ion battery applications. Li/Mn-rich layered oxides have a reversible capacity of ~280-310 mAh g^{-1} which is exceeding most design strategies thus far.[285] It competes with layered oxide analogs due to high theoretical capacity and improved stability, although their structure is more complex. Li/Mn-rich materials have a typical formula of x $Li_2MnO_3 \cdot (1-x)$ $LiMO_2$, where M = Ni, Co, Mn, Al, and others.[286] Excess lithium populates the transition metal layer, with a notation similar to $Li[Li_{1/3}Mn_{2/3}]O_2$.[286] Experimental evidence shows that oxidation of O^{2-} ions to O_2 is a major source of electrons during the initial extraction of Li^+ ions (charging).[287,288] This is corroborated by the fact that Mn^{4+} cannot be oxidized further.[289] Similar chemistry is present for Li-rich layered oxide materials, although high temperature synthesis methods prove challenging due to concurrent oxidation of Mn^{3+} to Mn^{4+} while keeping O^{2-} preserved in the lattice.[289–291]

Manganese is currently used in NMC layered oxide cathodes in the inert Mn^{4+} state. $LiMn_2O_4$ spinel materials employ the $Mn^{3+/4+}$ redox couple.[292,293,294] Although Mn has shown promise in various oxide cathode types, it lacks high energy density like the $Ni^{2+/4+}$ redox couple in NMC and NLO cathodes. The redox couple overlaps with the oxygen redox at moderate states-of-charge, creating design challenges. In disordered rocksalt materials, $Mn^{2+/4+}$ couple has gained attention because it avoids overlap with the oxygen redox providing increased capacity at a high average voltage.[295] It is desirable due to its low cost and toxicity.[152] Some report mixing active Mn with redox-inactive elements and fluorine.[296] The double redox of $Mn^{2+/4+}$ allows for the exchange of two electrons, generating high capacity analogs to $Ni^{2+/4+}$. As the $Mn^{2+/4+}$ couple requires formation in its discharged state, there must be enough Mn^{2+} and Li^+ ions to provide high capacity. To achieve the theoretical high capacity, Li-excess is required.

Structurally, Li-rich layered oxides crystallize with space group C2/m, compared to common $LiMO_2$ layered materials which crystallize in a hexagonal structure, $R\bar{3}m$.[297] Researchers have categorized this class of materials using two different concepts – solid solution and layer composite – due to its mixture between Li_2MnO_3 and $LiMO_2$ models.[298,299] This discrepancy is facilitated by the findings of a superstructure of Li^+ in the transition metal sites are found within the hexagon symmetry of the layered structure. Li-rich layered oxides having a distinct charging plateau at ~ 4.5V vs Li^+/Li which is caused by irreversible structural rearrangement. The structure loses its honeycomb cation ordering, Li^+-sites are depleted, and surface oxygen is loss.

Lastly, oxygen redox materials include disordered rocksalt materials. These materials have gained attention due to their uniqueness in not requiring a stable layered structure. Because of this, many different transition metals can be incorporated in these materials to facilitate local strain and allow for facile disorder.[296,300] Although lattice oxygen redox proves challenging in

determining reaction pathways in disordered rocksalt materials, it has unique advantages that make it a worthy system to explore for enhanced battery performance.[301,302] Disordered rocksalt cathodes typically consist of one or more active redox centers, excess Li content, and an F/O ratio on the anion site to ensure oxidation states are stable.[296,303] Trivalent redox couples, including $Mn^{3+/4+}$, $Fe^{3+/4+}$, and $Co^{3+/4+}$, provide minimal capacity so anion redox is required for high energy density. At higher voltages, trivalent couples and their associated anion redox is coupled with irreversibility oxygen loss and surface instability.[304,305,306] There are limited amounts of oxygen redox due to the lowered Mn valence state. To obtain Mn^{2+}, high-valent cations such as Nb^{5+} and Ti^{4+} have often been substituted.[307,308] To minimize the amount of oxygen redox, O^{2-} is replaced by F^{-}.[309,310] The fluorine substitution is aided by Li excess and cation disorder.[311]

Li-rich and Li-stoichiometric oxides have gas evolution occurring at similar voltages. CO_2/CO is produced from ~3.8-4.2V vs Li^+/Li and can continue to evolve in the system at high voltages of ~4.3-4.6V vs Li^+/Li.[312] At the higher voltages, O_2 evolution is expected. Researchers have determined there are three main contributors to C and O in the outgassing, including the TMO, the carbonate electrolytes, and Li_2CO_3.[170,312] During the first charging cycle in both Ni-rich and Li-rich oxides, CO_2/CO evolution occurs as decomposition of Li_2CO_3, regardless of the voltage region.[312] Using a pioneer mass spectrometry technique, differential/operando electrochemical mass spectrometry (DEMS/OEMS) was used to quantify the amount of gas generated from the Li_2CO_3 surface versus the TMO lattice oxygen by using isotopically enriched Li-rich TMOs with ^{18}O.[313,314] Using this technique it was confirmed that the first cycle is mostly Li_2CO_3 decomposition.[64] While there are ongoing challenges and debates surrounding the commercialization of oxygen redox materials, they provide a perspective on the vastness that exists in creative design for battery cathode materials.

7.3 Catapulting a Sustainable Future with Batteries

Sustainable, renewable energy has stood at the pinnacle of the ongoing energy revolution. Wind and solar generation have been prominent in integrating clean energy without compromising reliability, while the usage of biomass and hydroelectric dams have a trade-off of hindering wildlife and climate change. Clean energy is required for a sustainable future.

Li-ion batteries and innovation towards energy storage has catapulted research in the design and development of high energy materials. Since the commercialization of rechargeable battery technology in the 1990s and the 2019 Nobel Prize in Chemistry, many economic world leaders began investing in improving ongoing clean energy sources and promoting net-zero or carbon neutral environments by 2030. The plan towards net-zero carbon emissions within the next decade drives the necessity for improved battery materials.

7.3.1 Recyclability of Cathode Materials

The electric-vehicle revolution is imperative to reduce carbon emissions and improve the air quality associated with negative environmental impact. In decarbonizing the air, electric vehicle manufacturing plays a significant role, as raw materials and harsh production methods result in endless amounts of waste. As the energy and mobility stocks have continued to increase over the past year or so, the waste management of energy technology lacks continuous growth. Recyclability of the raw materials and other metals incorporated into oxide cathodes is extremely important. Nickel is not earth abundant, meaning at the end-of-life for a battery cell it is best to recover, recycle, and potentially repurpose the materials for a second life.

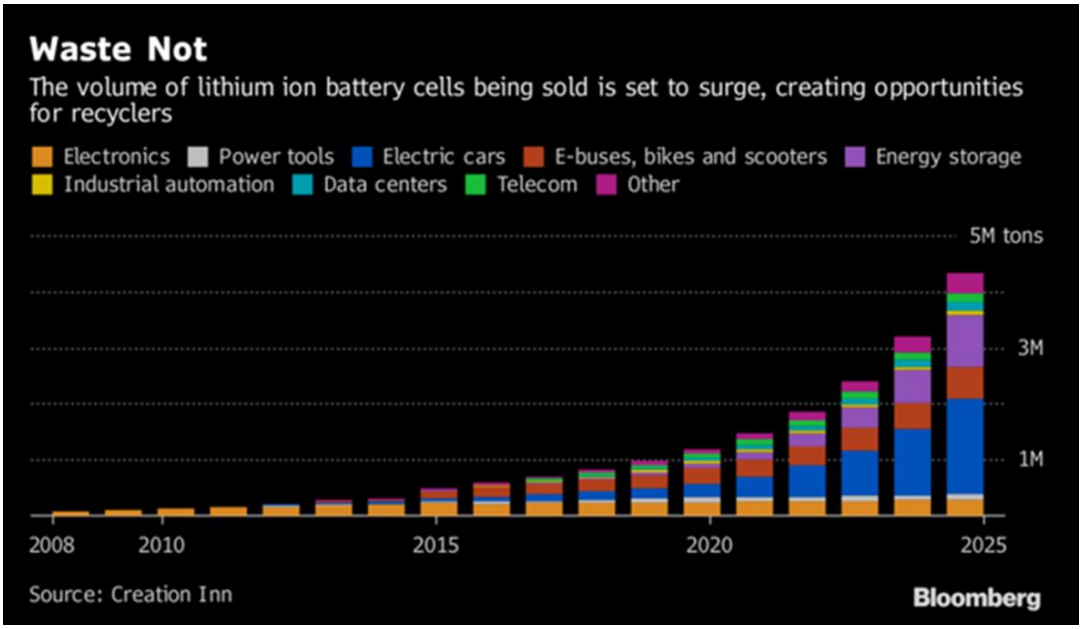

FIGURE 40: The volume of Li-ion battery cells that are being sold to consumers. By 2025, there will likely be a significant amount of opportunity for recycling and repurposing of battery materials. [Courtesy of Google Images]

By 2025, there will be roughly 5 million tons of battery material that can be recycled. Some researchers have taken the opportunity to develop green chemistry methods of recycling metals from battery cathode materials.

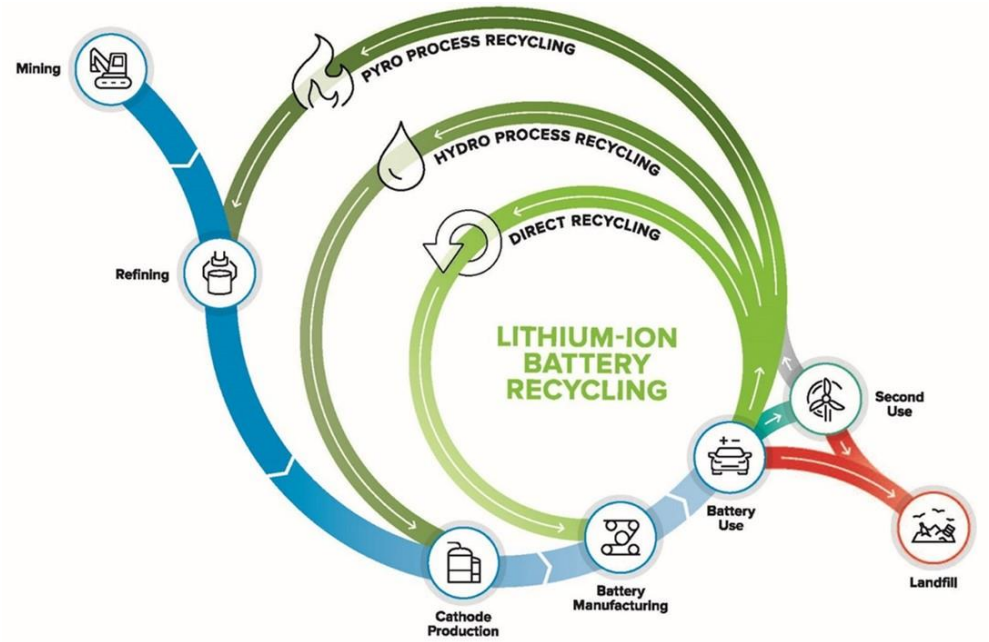

FIGURE 41: Cathode recycling pathways from direct recycling, hydro processing, and pyro processing. It is always best to determine a second use for battery materials so that the transition metals are not lost, especially ones that lack earth abundance. [Taken from Reference[315]]

Researchers at Argonne National Lab were able to discuss some of the pathways to improve cost effectiveness. The United States continues to try to reduce its dependence on foreign sources for battery innovation and diminish environmental impact. There are three major pathways to recycle battery materials (**Figure 41**) – direct, hydro process, and pyro process recycling. Hydrometallurgical process recycling typically requires very strong acids including H_2SO_4, HCl, and HNO_3, leading to many safety and health risks. Pyro process recycling requires extremely high temperatures which ends up not being cost effective. The direct recycling pathway is may be green or generate pathways to reuse or repurpose materials.

Wu et al. highlighted that orange peel waste could be used to extract transition metals.[316] In the study, the researchers showed that the citric acid found in orange peel could be used as a weak acid to leach out transition metals, such as Co, Ni, and Mn. At the completion transition metal leaching, the metals were reused to develop a working battery that had a comparable initial

capacity to the non-recycled battery material. Wu et al highlighted a "waste-for-waste" method that could be used to improve the circular economy of Li-ion batteries.

While this is only a start for recycling Li-ion battery materials, **Chapter 3** and **Chapter 5** in this dissertation highlight key strategies towards repurposing battery materials. To repurpose battery materials, one must know the surface and bulk chemistry associated with the materials. Additionally, using battery materials as nanocatalyst supports is another method in which they can obtain a second use. In the following *Section 7.3.2*, some of the competing chemistries associated with sustainability will be addressed.

7.3.2 Alternative Chemistries in Sustainability

Upon developing a sustainable future of energy storage devices, there are competing chemistries that provide different advantages depending on the application niche. Since the first rechargeable battery was developed in 1991, materials and their associated performance metrics have evolved, as shown in **Figure 42**.

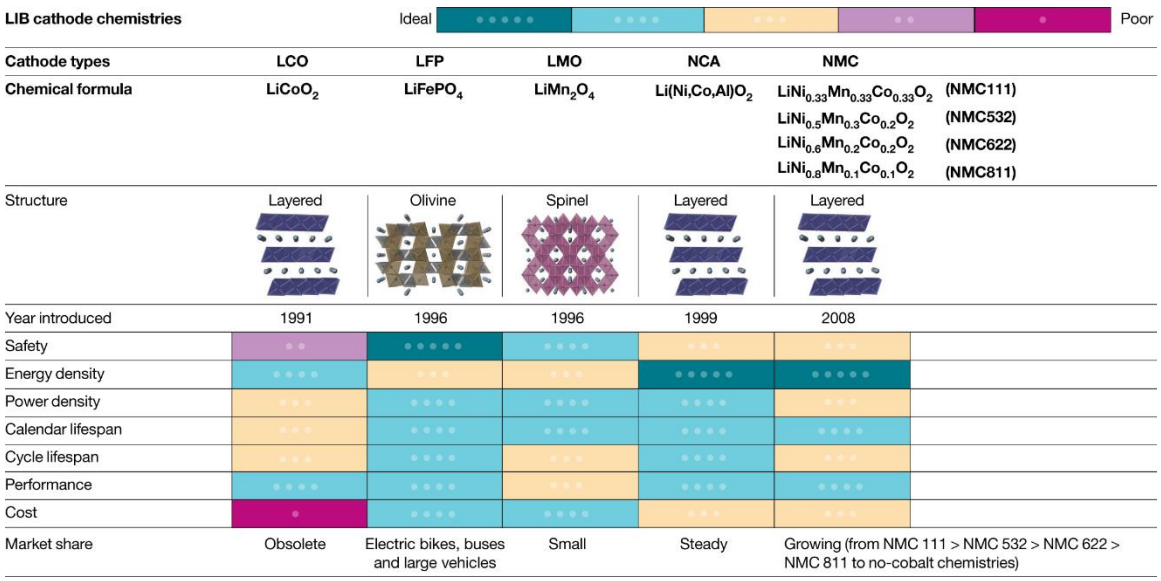

FIGURE 42: Commercialized Li-ion battery (LiB) cathode chemistries and their various performance attributes. In each of the materials, there are trade-off associated with the technology. The cathode chemistries largely impact the overall LiB performance. [Taken from Reference[317]]

Herein this dissertation, Li-ion chemistry was greatly discussed, but it is important to mention the rise of next-generation battery materials. As sustainability continues to become a global topic, using earth abundant metals is the next direction. Sodium[318–320] and magnesium ion[321,322] batteries are not well-developed yet, but much work has been started to develop the rechargeable battery chemistry associated with more earth abundant elements.[323] Sodium is very cheap, providing a cost effective alternative to Li-based materials. M. M. Rahman and coworkers was able to establish a composite layered oxide cathode with a long cycle life for Na^+ battery applications.[324]

7.3.3 Negative Carbon Emissions and a Greener World

Many technology giants around the globe are transitioning towards carbon neutrality or "net-zero" carbon emissions. This means that CO_2 that is emitted into the atmosphere via humans must be balanced by an equivalent amount being removed. Clean energy experts are using this energy

revolution to promote the role non-renewable resources have on impeding the carbon neutrality mission.

As a battery researcher, carbon emissions are important to consider when synthesizing new battery cathode and anode materials. Li_2CO_3 is a lithium source for Li-based cathode manufacturing, resulting in CO_2 generation. Moving forward, the use of carbonate-free reactants for energy storage materials will be advantageous. Additionally, to fully reach this goal the cost of electric vehicles and other environmentally friendly energy storage systems must be reasonable for all socioeconomic groups to afford being a part of the global energy transition. The goal of this dissertation is not only to provide a technical account of the novel methods highlighted in this work, but to motivate others to work towards positively impacting the goal of a sustainable future.

REFERENCES

(1) Muñoz-Páez, A. *J. Chem. Educ.* **1994**, *71* (5), 381–387.

(2) He, P.; Yu, H.; Li, D.; Zhou, H. *J. Mater. Chem.* **2012**, *22* (9), 3680.

(3) Kim, U.-H.; Jun, D.-W.; Park, K.-J.; Zhang, Q.; Kaghazchi, P.; Aurbach, D.; Major, D. T.; Goobes, G.; Dixit, M.; Leifer, N.; Wang, C. M.; Yan, P.; Ahn, D.; Kim, K.-H.; Yoon, C. S.; Sun, Y.-K. *Energy Environ. Sci* **2018**, *11*, 1271.

(4) Luo, K.; Roberts, M. R.; Hao, R.; Guerrini, N.; Pickup, D. M.; Liu, Y. S.; Edström, K.; Guo, J.; Chadwick, A. V.; Duda, L. C.; Bruce, P. G. *Nat. Chem.* **2016**, *8* (7), 684–691.

(5) Redel, K.; Kulka, A.; Plewa, A.; Molenda, J. *J. Electrochem. Soc.* **2019**, *166* (3), A5333–A5342.

(6) Liang, L.; Zhang, W.; Zhao, F.; Denis, D. K.; Zaman, F. uz; Hou, L.; Yuan, C. *Adv. Mater. Interfaces* **2020**, *7* (3), 1901749.

(7) de Biasi, L.; Schiele, A.; Roca-Ayats, M.; Garcia, G.; Brezesinski, T.; Hartmann, P.; Janek, J. *ChemSusChem* **2019**, *12* (10), 2240–2250.

(8) Jiang, M.; Key, B.; Meng, Y. S.; Grey, C. P. *Chem. Mater.* **2009**, *21* (13), 2733–2745.

(9) Hong, J.; Gwon, H.; Jung, S.-K.; Ku, K.; Kang, K. *J. Electrochem. Soc.* **2015**, *162* (14), A2447.

(10) Jiang, W.; Zhang, C.; Feng, Y.; Wei, B.; Chen, L.; Zhang, R.; Ivey, D. G.; Wang, P.; Wei, W. *Energy Storage Mater.* **2020**, *32*, 37–45.

(11) Yan, P.; Xiao, L.; Zheng, J.; Zhou, Y.; He, Y.; Zu, X.; Mao, S. X.; Xiao, J.; Gao, F.; Zhang, J.-G.; Wang, C.-M. **2015**.

(12) Liu, H.; Xiang, W.; Bai, C.; Qiu, L.; Wu, C.; Wang, G.; Liu, Y.; Song, Y.; Wu, Z.-G.; Guo, X. *Ind. Eng. Chem. Res.* **2020**, *59* (43), 19312–19321.

(13) Clé, R. J.; Lun, Z.; Ceder, G. *Energy Environ. Sci* **2020**, *13*, 345.

(14) Junji Akimoto, *; Yasuhiko Takahashi; Yoshito Gotoh, and; Kawaguchi, K.; and, K. D.; Uchida, I. *Chem. Mater.* **2003**, *15* (15), 2984–2990.

(15) Freire, M.; Lebedev, O. I.; Maignan, A.; Jordy, C.; Pralong, V. *This J. is Publ.* **2017**, *5* (5), 21898–21902.

(16) Yu, Z.; Qu, X.; Dou, A.; Su, M.; Liu, Y.; Wu, F. *ACS Appl. Mater. Interfaces* **2019**, *11*, 13.

(17) Mu, L.; Yang, Z.; Tao, L.; Waters, C. K.; Xu, Z.; Li, L.; Sainio, S.; Du, Y.; Xin, H. L.; Nordlund, D.; Lin, F. *J. Mater. Chem. A* **2020**, *8* (34), 17487–17497.

(18) Aishova, A.; Park, G.; Yoon, C. S.; Sun, Y. *Adv. Energy Mater.* **2020**, *10* (4), 1903179.

(19) Li, J.; Li, W.; Wang, S.; Jarvis, K.; Yang, J.; Manthiram, A. **2018**.

(20) Dyer, L. D.; Borie, B. S.; Smith, G. P. *J. Am. Chem. Soc.* **1954**, *76* (6), 1499–1503.

(21) Manthiram, A.; Knight, J. C.; Myung, S.-T.; Oh, S.-M.; Sun, Y.-K. *Adv. Energy Mater.* **2016**, *6* (1), 1501010.

(22) Widiyandari, H.; Sukmawati, A. N.; Sutanto, H.; Yudha, C.; Purwanto, A. In *Journal of Physics: Conference Series*; IOP Publishing, 2019; Vol. 1153, p 12074.

(23) Zhou, F.; Zhao, X.; Goodbrake, C.; Jiang, J.; Dahn, J. R. *J. Electrochem. Soc.* **2009**, *156* (10), A796.

(24) Bianchini, M.; Fauth, F.; Hartmann, P.; Brezesinski, T.; Janek, J. *J. Mater. Chem. A* **2020**, *8* (4), 1808–1820.

(25) Zhang, X.; Jiang, W. J.; Mauger, A.; Qilu; Gendron, F.; Julien, C. M. *J. Power Sources* **2010**, *195* (5), 1292–1301.

(26) Sun, G.; Yin, X.; Yang, W.; Song, A.; Jia, C.; Yang, W.; Du, Q.; Ma, Z.; Shao, G. *Phys. Chem. Chem. Phys.* **2017**, *19* (44), 29886–29894.

(27) Liu, W.; Oh, P.; Liu, X.; Lee, M.-J.; Cho, W.; Chae, S.; Kim, Y.; Cho, J. *Angew. Chemie Int. Ed.* **2015**, *54* (15), 4440–4457.

(28) Honglong Zhang; Bing Li; Jing Wang; Bihe Wu; Tao Fu; Jinbao Zhao. *RSC Adv.* **2016**, *6* (27), 22625–22632.

(29) Ronduda, H.; Zybert, M.; Szczęsna-Chrzan, A.; Trzeciak, T.; Ostrowski, A.; Szymański, D.; Wieczorek, W.; Raróg-Pilecka, W.; Marcinek, M. *Nanomaterials* **2020**, *10* (10), 1–21.

(30) Lin, F.; Markus, I. M.; Nordlund, D.; Weng, T.-C.; Asta, M. D.; Xin, H. L.; Doeff, M. M. *Nat. Commun.* **2014**, *5*, 3529.

(31) de Biasi, L.; Schiele, A.; Roca-Ayats, M.; Garcia, G.; Brezesinski, T.; Hartmann, P.; Janek, J. *ChemSusChem* **2019**, *12* (10), 2240–2250.

(32) Li, N.; Sallis, S.; Papp, J. K.; Wei, J.; McCloskey, B. D.; Yang, W.; Tong, W. *ACS Energy Lett.* **2019**, *4* (12), 2836–2842.

(33) Zhang, S. S. *Energy Storage Mater.* **2019**.

(34) Moses, A. W.; Flores, H. G. G.; Kim, J. G.; Langell, M. A. *Appl. Surf. Sci.* **2007**, *253* (10), 4782–4791.

(35) House, R. A.; Maitra, U.; Jin, L.; Lozano, J. G.; Somerville, J. W.; Rees, N. H.; Naylor, A. J.; Duda, L. C.; Massel, F.; Chadwick, A. V; Ramos, S.; Pickup, D. M.; Mcnally, D. E.; Lu, X.; Schmitt, T.; Roberts, M. R.; Bruce, P. G. **2019**.

(36) Mu, L.; Lin, R.; Xu, R.; Han, L.; Xia, S.; Sokaras, D.; Steiner, J. D.; Weng, T. C.; Nordlund, D.; Doeff, M. M.; Liu, Y.; Zhao, K.; Xin, H. L.; Lin, F. *Nano Lett.* **2018**, *18* (5), 3241–3249.

(37) Ryu, H. H.; Park, K. J.; Yoon, C. S.; Sun, Y. K. *Chem. Mater.* **2018**, *30* (3), 1155–1163.

(38) Sun, H.-H.; Manthiram, A. **2017**.

(39) Yang, Y.; Xu, R.; Zhang, K.; Lee, S.; Mu, L.; Liu, P.; Waters, C. K.; Spence, S.; Xu, Z.; Wei, C.; Kautz, D. J.; Yuan, Q.; Dong, Y.; Yu, Y.; Xiao, X.; Lee, H.; Pianetta, P.; Cloetens, P.; Lee, J.; Zhao, K.; Lin, F.; Liu, Y. *Adv. Energy Mater.* **2019**, *1900674*, 1900674.

(40) Takahashi, I.; Kiuchi, H.; Ohma, A.; Fukunaga, T.; Matsubara, E. *J. Phys. Chem. C* **2020**, *124* (17), 9243–9248.

(41) Wandt, J.; Freiberg, A. T. S.; Ogrodnik, A.; Gasteiger, H. A. *Mater. Today* **2018**, *21* (8), 825–833.

(42) Lu, Z.; Dahn, J. R. *J. Electrochem. Soc.* **2002**, *149* (7), A815.

(43) Thackeray, M. M.; Kang, S. H.; Johnson, C. S.; Vaughey, J. T.; Benedek, R.; Hackney, S. A. *J. Mater. Chem.* **2007**, *17* (30), 3112–3125.

(44) Zou, L.; Li, J.; Liu, Z.; Wang, G.; Manthiram, A.; Wang, C. *Nat. Commun.* **2019**, *10* (1), 1–11.

(45) Zhang, S. S. *J. Energy Chem.* **2020**, *41*, 135–141.

(46) Tian, C.; Nordlund, D.; Xin, H. L.; Xu, Y.; Liu, Y.; Sokaras, D.; Lin, F.; Doeff, M. M. *J. Electrochem. Soc.* **2018**, *165* (3), A696–A704.

(47) Jung, R.; Metzger, M.; Maglia, F.; Stinner, C.; Gasteiger, H. A. *J. Electrochem. Soc.* **2017**, *164* (7), A1361–A1377.

(48) Zhang, S. S. *Energy Storage Mater.* **2020**, *24*, 247–254.

(49) de Biasi, L.; Schiele, A.; Roca-Ayats, M.; Garcia, G.; Brezesinski, T.; Hartmann, P.; Janek, J. *ChemSusChem* **2019**, *12* (10), 2240–2250.

(50) Chien, P.-H.; Wu, X.; Song, B.; Yang, Z.; Waters, C. K.; Everett, M. S.; Lin, F.; Du, Z.; Liu, J. *Batter. Supercaps* **2021**, batt.202100135.

(51) Kim, U. H.; Park, J. H.; Aishova, A.; Ribas, R. M.; Monteiro, R. S.; Griffith, K. J.; Yoon, C. S.; Sun, Y. K. *Adv. Energy Mater.* **2021**.

(52) Yoon, C. S.; Jun, D. W.; Myung, S. T.; Sun, Y. K. *ACS Energy Lett.* **2017**, *2* (5), 1150–1155.

(53) Karki, K.; Huang, Y.; Whittingham, S.; Stach, E.; Zhou, G. *Microsc. Microanal* **2016**, *22*, 2016.

(54) Rong, X.; Parolin, J.; Kolpak, A. M. *ACS Catal.* **2016**, *6* (2), 1153–1158.

(55) Kong, F.; Liang, C.; Wang, L.; Zheng, Y.; Perananthan, S.; Longo, R. C.; Ferraris, J. P.; Kim, M.; Cho, K. *Adv. Energy Mater.* **2019**, *9* (2).

(56) Wandt, J.; Freiberg, A.; Thomas, R.; Gorlin, Y.; Siebel, A.; Jung, R.; Gasteiger, H. A.; Tromp, M. *J. Mater. Chem. A* **2016**, *4* (47), 18300–18305.

(57) Sahore, R.; O'Hanlon, D. C.; Tornheim, A.; Lee, C.-W.; Garcia, J. C.; Iddir, H.; Balasubramanian, M.; Bloom, I. *J. Electrochem. Soc.* **2020**, *167* (2), 020513.

(58) Hawley, W. B.; Parejiya, A.; Bai, Y.; Meyer, H. M.; Wood, D. L.; Li, J. *J. Power Sources* **2020**, *466*, 228315.

(59) Gilbert, J. A.; Shkrob, I. A.; Abraham, D. P. *J. Electrochem. Soc.* **2017**, *164* (2), A389.

(60) Li, Q.; Wang, Y.; Wang, X.; Sun, X.; Zhang, J. N.; Yu, X.; Li, H. *ACS Appl. Mater. Interfaces* **2020**, *12* (2), 2319–2326.

(61) Gao, H.; Cai, J.; Xu, G.-L.; Li, L.; Ren, Y.; Meng, X.; Amine, K.; Chen, Z. *Chem. Mater.* **2019**, *31* (8), 2723–2730.

(62) Yang, H.; Zhuang, G. V.; Ross, P. N. *J. Power Sources* **2006**, *161* (1), 573–579.

(63) Cabana, J.; Kwon, B. J.; Hu, L. *Cite This Acc. Chem. Res* **2018**, *51*, 299–308.

(64) Renfrew, S. E.; Mccloskey, B. D. *J. Am. Chem. Soc* **2017**, *139*, 17853–17860.

(65) Cho, J.; Jung, H.; Park, Y.; Kim, G.; Lim, H. S. **2000**, *147* (1), 15–20.

(66) He, P.; Yu, H.; Li, D.; Zhou, H. *J. Mater. Chem.* **2012**, *22* (9), 3680–3695.

(67) Wang, Q.; Ping, P.; Zhao, X.; Chu, G.; Sun, J.; Chen, C. *J. Power Sources* **2012**, *208*, 210–224.

(68) Teichert, P.; Eshetu, G. G.; Jahnke, H.; Figgemeier, E. *Batteries* **2020**, *6* (1), 1–26.

(69) Dahn, J. R.; Fuller, E. W.; Obrovac, M.; von Sacken, U. *Solid State Ionics* **1994**, *69* (3–4), 265–270.

(70) Jo, C.; Kim, Y. J.; Sun, Y.-K. *Artic. J. Electrochem. Soc.* **2014**.

(71) Jo, C. H.; Cho, D. H.; Noh, H. J.; Yashiro, H.; Sun, Y. K.; Myung, S. T. *Nano Res.* **2015**, *8* (5), 1464–1479.

(72) Xie, Y.; Gao, H.; Gim, J.; Ngo, A. T.; Chen, Z. *J. Phys. Chem. Lett.* **2019**, *10*, 589–594.

(73) Myung, S. T.; Maglia, F.; Park, K. J.; Yoon, C. S.; Lamp, P.; Kim, S. J.; Sun, Y. K. *ACS Energy Letters*. UTC 2017, pp 196–223.

(74) Liu, S.; Liu, D.; Wang, S.; Cai, X.; Qian, K.; Kang, F.; Li, B. *J. Mater. Chem. A* **2019**, *7* (21), 12993–12996.

(75) Wang, F.; Lin, Y.; Suo, L.; Fan, X.; Gao, T.; Yang, C.; Han, F.; Qi, Y.; Xu, K.; Wang, C. *This J. is Cite this Energy Environ. Sci* **2016**, *9*, 7.

(76) Liu, S.; Dongqing Liu, ab; Shuwei Wang, ac; Xingke Cai, ab; Qian, K.; Feiyu Kang abe, abe; Li, B. *J. Mater. Chem. A* **2019**, *7*, 12993–12996.

(77) Gauthier, M.; Carney, T. J.; Grimaud, A.; Giordano, L.; Pour, N.; Chang, H. H.; Fenning, D. P.; Lux, S. F.; Paschos, O.; Bauer, C.; Maglia, F.; Lupart, S.; Lamp, P.; Shao-Horn, Y. *Journal of Physical Chemistry Letters*. 2015, pp 4653–4672.

(78) Xu, K. *Chemical Reviews*. 2014, pp 11503–11618.

(79) Hekmatfar, M.; Kazzazi, A.; Eshetu, G. G.; Hasa, I.; Passerini, S. *ACS Appl. Mater.*

Interfaces **2019**, *11* (46), 43166–43179.

(80) Lebens-Higgins, Z. W.; Chung, H.; Zuba, M. J.; Rana, J.; Li, Y.; Faenza, N. V; Pereira, N.; Mccloskey, B. D.; Rodolakis, F.; Yang, W.; Whittingham, M. S.; Amatucci, G. G.; Meng, Y. S.; Lee, T.-L.; Piper, L. F. J. *J. Phys. Chem. Lett* **2020**, *11*.

(81) Zeng, X.; Xu, G. L.; Li, Y.; Luo, X.; Maglia, F.; Bauer, C.; Lux, S. F.; Paschos, O.; Kim, S. J.; Lamp, P.; Lu, J.; Amine, K.; Chen, Z. *ACS Appl. Mater. Interfaces* **2016**, *8* (5), 3446–3451.

(82) Zhang, Y.; Katayama, Y.; Tatara, R.; Giordano, L.; Yu, Y.; Fraggedakis, D.; Sun, J. G.; Maglia, F.; Jung, R.; Bazant, M. Z.; Shao-Horn, Y. *Energy Environ. Sci.* **2020**, *13* (1), 183–199.

(83) Mijung, N.; Lee, Y.; Cho, J. *J. Electrochem. Soc.* **2006**, *153* (5), A935.

(84) Al, C.; Matsumoto, K.; Kuzuo, R.; Takeya, K.; Yamanaka, A. *Effects of CO in air on Li deintercalation from LiNi*; Vol. 81.

(85) Li, Z.; Du, F.; Bie, X.; Zhang, D.; Cai, Y.; Cui, X.; Wang, C.; Chen, G.; Wei, Y. *J. Phys. Chem. C* **2010**, *114* (51), 22751–22757.

(86) Li, T.; Yuan, X.-Z.; Zhang, L.; Song, D.; Shi, K.; Bock, C. *Electrochem. Energy Rev.* **2020**, *3* (1), 43–80.

(87) Shaju, K. M.; Subba Rao, G. V.; Chowdari, B. V. R. *Electrochim. Acta* **2003**, *48* (18), 2691–2703.

(88) *Galvanostatic Intermittent Titration Technique*.

(89) Kim, K.; Ma, H.; Park, S.; Choi, N.-S. *ACS Energy Lett.* **2020**, 1537–1553.

(90) Tian, C.; Xu, Y.; Nordlund, D.; Lin, F.; Liu, J.; Sun, Z.; Liu, Y.; Doeff, M. *Joule* **2018**, 1–14.

(91) Li, M.; Lu, J. *Science*. 2020, pp 979–980.

(92) Eom, J.; Kim, M. G.; Cho, J. *J. Electrochem. Soc.* **2008**, *155* (3), A239.

(93) Jung, R.; Morasch, R.; Karayaylali, P.; Phillips, K.; Maglia, F.; Stinner, C.; Shao-Horn, Y.; Gasteiger, H. A. *J. Electrochem. Soc.* **2018**, *165* (2), A132–A141.

(94) Huang, B.; Qian, K.; Liu, Y.; Liu, D.; Zhou, K.; Kang, F.; Li, B. *ACS Sustain. Chem. Eng.* **2019**, *7* (7), 7378–7385.

(95) Ren, H.; Huang, Y.; Wang, Y.; Li, Z.; Cai, P.; Peng, Z.; Zhou, Y. *Mater. Chem. Phys.* **2009**, *117* (1), 41–45.

(96) Baggetto, L.; Dudney, N. J.; Veith, G. M. *Electrochim. Acta* **2013**, *90*, 135–147.

(97) Grenier, A.; Liu, H.; Wiaderek, K. M.; Lebens-Higgins, Z. W.; Borkiewicz, O. J.; J Piper, L. F.; Chupas, P. J.; Chapman, K. W. *Chem. Mater* **2017**, *29*, 7345–7352.

(98) Liu, H.; Yang, Y.; Zhang, J. *J. Power Sources* **2007**, *173* (1), 556–561.

(99) Liu, H. S.; Zhang, Z. R.; Gong, Z. L.; Yang, Y. *Electrochem. Solid-State Lett.* **2004**, *7* (7).

(100) Prado, G.; Fournès, L.; Delmas, C. *J. Solid State Chem.* **2001**, *159* (1), 103–112.

(101) Kalyani, P.; Kalaiselvi, N. *Sci. Technol. Adv. Mater.* **2005**, *6* (6), 689–703.

(102) Jia, G.; Li, F.; Wang, J.; Liu, S.; Yang, Y. *ACS Appl. Mater. Interfaces* **2021**, *13* (16), 18733–18742.

(103) Yang, Z.; Mu, L.; Hou, D.; Rahman, M. M.; Xu, Z.; Liu, J.; Nordlund, D.; Sun, C.; Xiao, X.; Lin, F. *Adv. Energy Mater.* **2021**, *11* (1), 2002719.

(104) Mu, L.; Kan, W. H.; Kuai, C.; Yang, Z.; Li, L.; Sun, C. J.; Sainio, S.; Avdeev, M.; Nordlund, D.; Lin, F. *ACS Appl. Mater. Interfaces* **2020**, *12* (11), 12874–12882.

(105) Xin, F.; Zhou, H.; Chen, X.; Zuba, M.; Chernova, N.; Zhou, G.; Whittingham, M. S. *ACS Appl. Mater. Interfaces* **2019**, *11* (38), 34889–34894.

(106) Dou, S. *Journal of Solid State Electrochemistry*. 2013, pp 911–926.

(107) Chen, Z.; Qin, Y.; Amine, K.; Sun, Y. K. *J. Mater. Chem.* **2010**, *20* (36), 7606–7612.

(108) David, L.; Dahlberg, K.; Mohanty, D.; Ruther, R. E.; Huq, A.; Chi, M.; An, S. J.; Mao, C.; King, D. M.; Stevenson, L.; Wood, D. L. *ACS Appl. Energy Mater.* **2019**, *2* (2), 1308–1313.

(109) Zhang, B.; Dong, P.; Tong, H.; Yao, Y.; Zheng, J.; Yu, W.; Zhang, J.; Chu, D. *J. Alloys Compd.* **2017**, *706*, 198–204.

(110) Yuan, H.; Song, W.; Wang, M.; Gu, Y.; Chen, Y. *J. Alloys Compd.* **2019**, *784*, 1311–1322.

(111) Kim, H.; Byun, D.; Chang, W.; Jung, H.-G.; Choi, W. *J. Mater. Chem. A* **2017**, *5* (47), 25077–25089.

(112) Park, J. S.; Meng, X.; Elam, J. W.; Hao, S.; Wolverton, C.; Kim, C.; Cabana, J. *Chem. Mater.* **2014**, *26* (10), 3128–3134.

(113) Shobana, M. K. *J. Alloys Compd.* **2019**, *802*, 477–487.

(114) Sun, Y.-K.; Lee, M.-J.; Yoon, C. S.; Hassoun, J.; Amine, K.; Scrosati, B. *Adv. Mater.* **2012**, *24* (9), 1192–1196.

(115) Appapillai, A. T.; Mansour, A. N.; Cho, J.; Shao-Horn, Y. *Chem. Mater.* **2007**, *19* (23), 5748–5757.

(116) Li, W.; Yang, L.; Li, Y.; Chen, Y.; Guo, J.; Zhu, J.; Pan, H.; Xi, X. *Front. Chem.* **2020**, *8*.

(117) Wise, A. M.; Ban, C.; Weker, J. N.; Misra, S.; Cavanagh, A. S.; Wu, Z.; Li, Z.; Whittingham, M. S.; Xu, K.; George, S. M.; Toney, M. F. *Chem. Mater.* **2015**, *27* (17), 6146–6154.

(118) Jaephil Cho, †; Yong Jeong Kim, ‡ and; Byungwoo Park*, ‡. *Chem. Mater.* **2000**, *12* (12), 3788–3791.

(119) Hwang, S.; Chang, W.; Min Kim, S.; Su, D.; Hyun Kim, D.; Yong Lee, J.; Yoon Chung, K.; Stach, E. A. *Chem. Mater* **2014**, *26*, 30.

(120) Mohanty, D.; Dahlberg, K.; King, D. M.; David, L. A.; Sefat, A. S.; Wood, D. L.; Daniel, C.; Dhar, S.; Mahajan, V.; Lee, M.; Albano, F. *Sci. Rep.* **2016**, *6*.

(121) Diaz, F.; Wang, Y.; Moorthy, T.; Friedrich, B. *Metals (Basel).* **2018**, *8* (8).

(122) McNair, H. M.; Miller, J. M. *Basic Gas Chromatography*; 2002.

(123) Gross, J. H. *Mass Spectrometry*; 2004.

(124) Holm, T. *J. Chromatogr. A* **1999**, *842*, 221–227.

(125) Poole, C. F. *J. Chromatogr. A* **2015**, *1421*, 137–153.

(126) Watts, J. F.; Wolstenholme, J. *An Introduction to Surface Analysis by XPS and AES*; Wiley, 2019.

(127) Holoubek, J.; Liu, H.; Wu, Z.; Yin, Y.; Xing, X.; Cai, G.; Yu, S.; Zhou, H.; Pascal, T. A.; Chen, Z.; Liu, P. *Nat. Energy* **2021**, *6* (3), 303–313.

(128) Mansour, A. N. *Surf. Sci. Spectra* **1994**, *3* (3), 279–286.

(129) Zou, Y.; Yang, X.; Lv, C.; Liu, T.; Xia, Y.; Shang, L.; Waterhouse, G. I. N.; Yang, D.; Zhang, T. *Adv. Sci.* **2017**, *4* (1), 1600262.

(130) Song, H. J.; Jang, S. H.; Choi, K.; Nam, S. C.; Mun, J.; Yim, T. *ACS Sustain. Chem. Eng.* **2020**, *8* (19), 7316–7323.

(131) Zaera, F. *Chemical Reviews*. Wiley February 10, 2012, pp 2920–2986.

(132) Kakavelakis, G.; Gedda, M.; Panagiotopoulos, A.; Kymakis, E.; Anthopoulos, T. D.; Petridis, K. *Adv. Sci.* **2020**, *7* (22), 1–33.

(133) Penner-Hahn, J. E. *Compr. Coord. Chem. II* **2003**, *2*, 159–186.

(134) Besli, M. M.; Shukla, A. K.; Wei, C.; Metzger, M.; Alvarado, J.; Boell, J.; Nordlund, D.; Schneider, G.; Hellstrom, S.; Johnston, C.; Christensen, J.; Doeff, M. M.; Liu, Y.; Kuppan, S. *J. Mater. Chem. A* **2019**, *7* (20), 12593–12603.

(135) Zhang, L. In *Methods in Molecular Biology*; Humana Press Inc., 2019; Vol. 1876, pp 179–195.

(136) Eckert, M. *Ann. Phys.* **2012**, *524* (5), 83–85.

(137) Eckert, M. *Acta Crystallogr. Sect. A Found. Crystallogr.* **2012**, *68* (1), 30–39.

(138) Warren, B. E. *J. Appl. Phys.* **1941**, *12* (5), 375–383.

(139) Nasir, S.; Zobir, M.; Zanial, Z.; Azah, N.; Afif, S.; Mustapha, I. *Bioresources* **2020**, *14* (2019), 2352–2388.

(140) McCalla, E.; Sougrati, M. T.; Rousse, G.; Berg, E. J.; Abakumov, A.; Recham, N.; Ramesha, K.; Sathiya, M.; Dominko, R.; Van Tendeloo, G.; Novák, P.; Tarascon, J. M. *J. Am. Chem. Soc.* **2015**, *137* (14), 4804–4814.

(141) Levartovsky, Y.; Chakraborty, A.; Kunnikuruvan, S.; Maiti, S.; Grinblat, J.; Talianker, M.;

Major, D. T.; Aurbach, D. *ACS Appl. Mater. Interfaces* **2021**, *13* (29), 34145–34156.

(142) Han, F.; Yue, J.; Chen, C.; Zhao, N.; Fan, X.; Ma, Z.; Gao, T.; Wang, F.; Guo, X.; Wang, C. *Joule* **2018**, *2* (3), 497–508.

(143) Hawkes, P.; Kasper, E. *Princ. Electron Opt.* **2018**, No. 1955, 1–12.

(144) Ul-Hamid, A. *A Beginners' Guide to Scanning Electron Microscopy*; 2018.

(145) Buseck, P. R. *Miner. React. At. Scale* **2018**, 1–36.

(146) Croy, J. R.; O'hanlon, D. C.; Sharifi-Asl, S.; Murphy, M.; Mane, A.; Lee, C.-W.; Trask, S. E.; Shahbazian-Yassar, R.; Balasubramanian, M. *Chem. Mater* **2019**, *31*, 35.

(147) Kim, Y.; Seong, W. M.; Manthiram, A. *Energy Storage Materials*. Elsevier B.V. January 1, 2021, pp 250–259.

(148) Yin, S.; Deng, W.; Chen, J.; Gao, X.; Zou, G.; Hou, H.; Ji, X. *Nano Energy* **2021**, *83* (February), 105854.

(149) Liu, T.; Yu, L.; Liu, J.; Lu, J.; Bi, X.; Dai, A.; Li, M.; Li, M.; Hu, Z.; Ma, L.; Luo, D.; Zheng, J.; Wu, T.; Ren, Y.; Wen, J.; Pan, F.; Amine, K. *Nat. Energy 2021 63* **2021**, *6* (3), 277–286.

(150) Mizushima, K.; Jones, P. C.; Wiseman, P. J.; Goodenough, J. B. *Mater. Res. Bull.* **1980**, *15* (6), 783–789.

(151) Antolini, E. *Solid State Ionics* **2004**, *170* (3–4), 159–171.

(152) Nitta, N.; Wu, F.; Lee, J. T.; Yushin, G. *Materials Today*. Elsevier B.V. June 1, 2015, pp 252–264.

(153) Sun, Y.-K.; Lee, D.-J.; Lee, Y. J.; Chen, Z.; Myung, S.-T. **2013**.

(154) Jo, J. H.; Jo, C. H.; Yashiro, H.; Kim, S. J.; Myung, S. T. *J. Power Sources* **2016**, *313*, 1–8.

(155) Deng, T.; Fan, X.; Cao, L.; Su, D.; Yang, X.-Q.; Wang, C.; Chen, J.; Hou, S.; Ji, X.; Chen, L.; Li, S.; Zhou, X.; Hu, E. *Joule* **2019**, *3*, 2550–2564.

(156) Li, T.; Yuan, X. Z.; Zhang, L.; Song, D.; Shi, K.; Bock, C. *Electrochemical Energy Reviews*. Springer October 21, 2020, pp 43–80.

(157) Zheng, J.; Kan, W. H.; Manthiram, A. *ACS Appl. Mater. Interfaces* **2015**, *7* (12), 6926–6934.

(158) Lipson, A. L.; Durham, J. L.; LeResche, M.; Abu-Baker, I.; Murphy, M. J.; Fister, T. T.; Wang, L.; Zhou, F.; Liu, L.; Kim, K.; Johnson, D. *ACS Appl. Mater. Interfaces* **2020**, *12* (16), 18512–18518.

(159) Sheu, S. P.; Shih, I. C.; Yao, C. Y.; Chen, J. M.; Hurng, W. M. *J. Power Sources* **1997**, *68* (2), 558–560.

(160) Yamada, S.; Fijiwara, M.; Kanda, M. *J. Power Sources* **1995**, *54*, 209–213.

(161) Kim, Y.; Lee, H.; Kang, S. *J. Mater. Chem.* **2012**, *22* (25), 12874–12881.

(162) Lin, F.; Nordlund, D.; Pan, T.; Markus, I. M.; Weng, T. C.; Xin, H. L.; Doeff, M. M. *J. Mater. Chem. A* **2014**, *2* (46), 19833–19840.

(163) Steiner, J. D.; Mu, L.; Walsh, J.; Rahman, M. M.; Zydlewski, B.; Michel, F. M.; Xin, H. L.; Nordlund, D.; Lin, F. *ACS Appl. Mater. Interfaces* **2018**, *10* (28), 23842–23850.

(164) Jung, R.; Linsenmann, F.; Thomas, R.; Wandt, J.; Solchenbach, S.; Maglia, F.; Stinner, C.; Tromp, M.; Gasteiger, H. A. *J. Electrochem. Soc.* **2019**, *166* (2), A378–A389.

(165) Aurbach, D.; Markovsky, B.; Salitra, G.; Markevich, E.; Talyossef, Y.; Koltypin, M.; Nazar, L.; Ellis, B.; Kovacheva, D. *J. Power Sources* **2007**, *165* (2), 491–499.

(166) Hausbrand, R.; Cherkashinin, G.; Ehrenberg, H.; Gröting, M.; Albe, K.; Hess, C.; Jaegermann, W. *Mater. Sci. Eng. B* **2015**, *192*, 3–25.

(167) Chen, G.; Hai, B.; Shukla, A. K.; Duncan, H. *J. Electrochem. Soc.* **2012**, *159* (9), A1543–A1550.

(168) Duan, Y.; Yang, L.; Zhang, M. J.; Chen, Z.; Bai, J.; Amine, K.; Pan, F.; Wang, F. *J. Mater. Chem. A* **2019**, *7* (2), 513–519.

(169) Zhang, M.-J.; Teng, G.; Chen-Wiegart, Y.-C. K.; Duan, Y.; Young, J.; Ko, P.; Zheng, J.; Thieme, J.; Dooryhee, E.; Chen, Z.; Bai, J.; Khalil Amine, ‖; Feng, #; Wang, F. *J. Am. Chem. Soc* **2018**, No. 140, 12484–12492.

(170) Jo, C. H.; Cho, D. H.; Noh, H. J.; Yashiro, H.; Sun, Y. K.; Myung, S. T. *Nano Res.* **2015**, *8* (5), 1464–1479.

(171) Park, J. H.; Choi, B.; Kang, Y. S.; Park, S. Y.; Yun, D. J.; Park, I.; Shim, J. H.; Park, J. H.; Han, H. N.; Park, K. *Energy Technol.* **2018**, *6* (7), 1361–1369.

(172) Liu, X.; Liu, T.; Wang, R.; Cai, Z.; Wang, W.; Yuan, Y.; Shahbazian-Yassar, R.; Li, X.; Wang, S.; Hu, E.; Yang, X.-Q.; Xiao, Y.; Amine, K.; Lu, J.; Sun, Y. *Cite This ACS Energy Lett* **2021**, *6*, 328.

(173) Yang, H. X.; Dong, Q. F.; Hu, X. H.; Ai, X. P.; Li, S. X. *J. Power Sources* **1999**, *79* (2), 256–261.

(174) Wang, V. C.-C.; Maji, S.; Chen, P. P.-Y.; Lee, H. K.; Yu, S. S.-F.; Chan, S. I. *Chem. Rev.* **2017**, acs.chemrev.6b00624.

(175) Tinberg, C. E.; Lippard, S. J. *Acc. Chem. Res.* **2011**, *44* (4), 280–288.

(176) Finocchio, E.; Busca, G.; Lorenzelli, V.; Willey, R. J. *J. Catal.* **1995**, *151* (1), 204–215.

(177) Latimer, A. A.; Kulkarni, A. R.; Aljama, H.; Montoya, J. H.; Yoo, J. S.; Tsai, C.; Abild-Pedersen, F.; Studt, F.; Nørskov, J. K. *Nat. Mater.* **2017**, *16* (2), 225–229.

(178) Kaneda, K.; Mitsudome, T.; Mizugaki, T.; Jitsukawa, K. *Molecules* **2010**, *15* (12), 8988–9007.

(179) Pina, C. Della; Falletta, E.; Rossi, M. **2015**, No. 28, 133–154.

(180) Velasquez Ochoa, J.; Cavani, F. *Transit. Met. Catal. Aerob. Alcohol Oxid.* **2014**, No. 28,

203–230.

(181) Permyakova, A. A.; Han, B.; Jensen, J. O.; Bjerrum, N. J.; Shao-Horn, Y. *J. Phys. Chem. C* **2015**, *119* (15), 8023–8031.

(182) Sugano, Y.; Shiraishi, Y.; Tsukamoto, D.; Ichikawa, S.; Tanaka, S.; Hirai, T. *Angew. Chemie - Int. Ed.* **2013**, *52* (20), 5295–5299.

(183) Della Pina, C.; Falletta, E.; Rossi, M. *J. Catal.* **2008**, *260* (2), 384–386.

(184) Enache, D. I.; Edwards, J. K.; Landon, P.; Solsona-espriu, B.; Carley, A. F.; Herzing, A. A.; Watanabe, M.; Kiely, C. J.; Knight, D. W.; Hutchings, G. J. *Science (80-.).* **2006**, *311* (January), 362–366.

(185) Article, E. *Chem. Sci.* **2016**, *00*, 1–13.

(186) Hao, Y.; Hao, G.-P.; Guo, D.-C.; Guo, C.-Z.; Li, W.-C.; Li, M.-R.; Lu, A.-H. *ChemCatChem* **2012**, *4* (10), 1595–1602.

(187) Besson, M.; Gallezot, P. *Catal. Today* **2000**, *57* (1), 127–141.

(188) Mannel, D. S.; Ahmed, M. S.; Root, T. W.; Stahl, S. S. .

(189) Reed, M.; Kimberger, O.; McGovern, P. D.; Albrecht, M. C. *AANA J.* **2013**, *81* (4), 275–281.

(190) Corma, A.; Garcia, H.; Velty, A.; Iglesias, M.; Sanchez, F.; Iwasawa, Y.; Pinna, F.; Pernicone, N.; Knight, D. W.; Hutchings, G. J.; Stitt, E. H.; Johnston, P.; Griffin, K.; Kiely, C. J. *Chem. Soc. Rev.* **2008**, *37* (9), 2096.

(191) Markó, I. E.; Gautier, A.; Chellé-Regnaut, I.; Giles, P. R.; Tsukazaki, M.; Urch, C. J.; Brown, S. M. *J. Org. Chem.* **1998**, *63* (22), 7576–7577.

(192) Zope, B. N.; Hibbitts, D. D.; Neurock, M.; Davis, R. J. *Science* **2010**, *330* (6000), 74–78.

(193) Abad, A.; Almela, C.; Corma, A.; García, H. *Tetrahedron* **2006**, *62* (28), 6666–6672.

(194) Abad, A.; Concepción, P.; Corma, A.; García, H. *Angew. Chemie Int. Ed.* **2005**, *44* (26), 4066–4069.

(195) Chen, J.; Zhang, Q.; Wang, Y.; Wan, H. *Adv. Synth. Catal.* **2008**, *350* (3), 453–464.

(196) Gao, D.; Zhou, H.; Wang, J.; Miao, S.; Yang, F.; Wang, G.; Wang, J.; Bao, X. *J. Am. Chem. Soc.* **2015**, *137* (13), 4288–4291.

(197) Zhang, N.; Li, J.; Li, H.; Liu, A.; Huang, Q.; Ma, L.; Li, Y.; Dahn, J. R. **2018**.

(198) Renfrew, S. E.; McCloskey, B. D. *J. Electrochem. Soc.* **2019**, *166* (13), A2762–A2768.

(199) Jung, R.; Strobl, P.; Maglia, F.; Stinner, C.; Gasteiger, H. A. *J. Electrochem. Soc.* **2018**, *165* (11), A2869–A2879.

(200) Arena, F.; Gumina, B.; Cannilla, C.; Spadaro, L.; Patti, A.; Spiccia, L. *Appl. Catal. B Environ.* **2015**, *170–171*, 233–240.

(201) Sun, N.; Hou, Y.; Wu, W.; Niu, M.; Wang, W. *Electrochem. commun.* **2013**, *28*, 34–36.

(202) Makwana, V. D.; Son, Y.; Howell, A. R.; Suib, S. L. **2002**, *52*, 46–52.

(203) Védrine, J. C. *ChemSusChem* **2019**, *12* (3), 577–588.

(204) Mallat, T.; Baiker, A. **2003**.

(205) Seki, T.; Nakajo, T.; Onaka, M. *Chem. Lett.* **2006**, *35* (8), 824–829.

(206) Waddell, D. C.; Mack, J. *Green Chem.* **2009**, *11* (1), 79–82.

(207) Ogata, Y.; Kawasaki, A. *Tetrahedron* **1969**, *25* (14), 2845–2851.

(208) Törmäkangas, O. P.; Koskinen, A. M. . *Tetrahedron Lett.* **2001**, *42* (14), 2743–2746.

(209) Mao, C.; Ruther, R. E.; Geng, L.; Li, Z.; Leonard, D. N.; Meyer, H. M.; Sacci, R. L.; Wood, D. L. *ACS Appl. Mater. Interfaces* **2019**, acsami.9b15916.

(210) Ryu, H. H.; Park, K. J.; Yoon, C. S.; Sun, Y. K. *Chem. Mater.* **2018**, *30* (3), 1155–1163.

(211) Benzoic acid | C6H5COOH - PubChem https://pubchem.ncbi.nlm.nih.gov/compound/Benzoic-acid (accessed Oct 24, 2019).

(212) Lin, F.; Nordlund, D.; Markus, I. M.; Weng, T.-C.; Xin, H. L.; Doeff, M. M. *Energy Environ. Sci.* **2014**, *7* (9), 3077.

(213) Leanza, D.; Mirolo, M.; Vaz, C. A. F.; Novák, P.; El Kazzi, M. *Batter. Supercaps* **2019**, *2* (5), 482–492.

(214) Zheng, J.; Yan, P.; Zhang, J.; Engelhard, M. H.; Zhu, Z.; Polzin, B. J.; Trask, S.; Xiao, J.; Wang, C.; Zhang, J. *Nano Res.* **2017**, *10* (12), 4221–4231.

(215) Renfrew, S. E.; McCloskey, B. D. *ACS Appl. Energy Mater.* **2019**, *2* (5), 3762–3772.

(216) Fu, Z.; Hu, J.; Hu, W.; Yang, S.; Luo, Y. *Appl. Surf. Sci.* **2018**, *441*, 1048–1056.

(217) Andreu, N.; Flahaut, D.; Dedryvère, R.; Minvielle, M.; Martinez, H.; Gonbeau, D. *ACS Appl. Mater. Interfaces* **2015**, *7* (12), 6629–6636.

(218) Xu, J.; Lin, F.; Nordlund, D.; Crumlin, E. J.; Wang, F.; Bai, J.; Doeff, M. M.; Tong, W. *Chem. Commun.* **2016**, *52* (22), 4239–4242.

(219) Zhao, Y.; Wang, S.; Ren, W.; Wu, R. *J. Electrochem. Soc.* **2013**, *160* (1).

(220) Xu, R.; de Vasconcelos, L. S.; Shi, J.; Li, J.; Zhao, K. *Exp. Mech.* **2018**, *58* (4), 549–559.

(221) Mu, L.; Zhang, R.; Kan, W. H.; Zhang, Y.; Li, L.; Kuai, C.; Zydlewski, B.; Rahman, M. M.; Sun, C. J.; Sainio, S.; Avdeev, M.; Nordlund, D.; Xin, H. L.; Lin, F. *Chem. Mater.* **2019**, *31* (23), 9769–9776.

(222) Aishova, A.; Park, G. T.; Yoon, C. S.; Sun, Y. K. *Adv. Energy Mater.* **2020**, *10* (4), 1–9.

(223) Sun, Y.-K.; Lee, D.-J.; Lee, Y. J.; Chen, Z.; Myung, S.-T. *ACS Appl. Mater. Interfaces* **2013**, *5* (21), 11434–11440.

(224) Edström, K.; Gustafsson, T.; Thomas, J. O. *Electrochim. Acta* **2004**, *50* (2-3 SPEC. ISS.), 397–403.

(225) Chen, Z.; Amine, R.; Ma, Z.; Amine, K. *J. Phys. D. Appl. Phys.* **2017**, *50* (30).

(226) Hausbrand, R.; Cherkashinin, G.; Ehrenberg, H.; Gröting, M.; Albe, K.; Hess, C.; Jaegermann, W. *Materials Science and Engineering B: Solid-State Materials for Advanced Technology*. Elsevier Ltd February 1, 2015, pp 3–25.

(227) Xu, J.; Hu, E.; Nordlund, D.; Mehta, A.; Ehrlich, S. N.; Yang, X. Q.; Tong, W. *ACS Appl. Mater. Interfaces* **2016**, *8* (46), 31677–31683.

(228) Xu, J.; Hu, E.; Nordlund, D.; Mehta, A.; Ehrlich, S. N.; Yang, X. Q.; Tong, W. *ACS Appl. Mater. Interfaces* **2016**, *8* (46), 31677–31683.

(229) Hsieh, B.-J.; Tsai, M.-C.; Pan, C.-J.; Su, W.-N.; Rick, J.; Chou, H.-L.; Lee, J.-F.; Hwang, B.-J. *Electrochim. Acta* **2017**, *224*, 452–459.

(230) Yang, Y.; Jiang, K.; Guo, J.; Li, J.; Peng, X.; Hong, B.; Wang, X.; Ge, H. *Chem. Eng. J.* **2020**, *381* (August 2019).

(231) Zhan, W.; He, Q.; Liu, X.; Guo, Y.; Wang, Y.; Wang, L.; Guo, Y.; Borisevich, A. Y.; Zhang, J.; Lu, G.; Dai, S. *J. Am. Chem. Soc.* **2016**, *138* (49), 16130–16139.

(232) Sankar, M.; He, Q.; Engel, R. V; Sainna, M. A.; Logsdail, A. J.; Roldan, A.; Willock, D. J.; Agarwal, N.; Kiely, C. J.; Hutchings, G. J. *Chemical Reviews*. 2020, pp 3890–3938.

(233) Albonetti, S.; Mazzoni, R.; Cavani, F. *Homogeneous , Heterogeneous and Nanocatalysis*; Chapter 1 In: Transition Metal Catalysis in Aerobic Alcohol Oxidation, 2015.

(234) Linic, S.; Christopher, P.; Xin, H.; Marimuthu, A. *Acc. Chem. Res.* **2013**, *46* (8), 1890–1899.

(235) Suchomel, P.; Kvitek, L.; Prucek, R.; Panacek, A.; Halder, A.; Vajda, S.; Zboril, R. *Sci. Rep.* **2018**, *8* (1), 4589.

(236) Alegria, E.; Ribeiro, A.; Mendes, M.; Ferraria, A.; do Rego, A.; Pombeiro, A. *Nanomaterials* **2018**, *8* (5), 320.

(237) Cho, H. R.; Kwon, Y. M.; Lee, Y. J.; Park, Y. A.; Ji, H. G.; Lee, J. H. *Appl. Clay Sci.* **2018**, *156*, 187–194.

(238) Boronat, M.; Corma, A. *Langmuir* **2010**, *26* (21), 16607–16614.

(239) Lin, X.; Wu, M.; Wu, D.; Kuga, S.; Endo, T.; Huang, Y. *Green Chem.* **2011**, *13* (2), 283–287.

(240) Imran, M.; Yousaf, A. B.; Zhou, X.; Jiang, Y.-F.; Yuan, C.-Z.; Zeb, A.; Jiang, N.; Xu, A.-W. *J. Phys. Chem. C* **2017**, *121* (2), 1162–1170.

(241) Ayad, A. I.; Luart, D.; Dris, A. O.; Guénin, E. *Nanomaterials* **2020**, *10* (6), 1–16.

(242) Mak, S. Y.; Liew, K. H.; Chua, C. C.; Yarmo, M. A.; Yahaya, B. H.; Samad, W. Z.; Jamil, M. S. M.; Yusop, R. M. *J. Chem. Sci.* **2019**, *131* (11).

(243) Yahagi, T.; Togashi, T.; Kurihara, M. *RSC Adv.* **2020**, *10* (8), 4545–4553.

(244) Verma, A.; Shukla, M.; Kumar, S.; Pal, S.; Sinha, I. *Spectrochim. Acta - Part A Mol. Biomol. Spectrosc.* **2020**, *240*.

(245) Neelam; Meyerstein, D.; Adhikary, J.; Burg, A.; Shamir, D.; Albo, Y. *Catal. Commun.* **2020**, *133*.

(246) Pradhan, N.; Pal, A.; Pal, T. *Colloids Surfaces A Physicochem. Eng. Asp.* **2002**, *196*, 247–257.

(247) Beswick, O.; Parastaev, A.; Yuranov, I.; LaGrange, T.; Dyson, P. J.; Kiwi-Minsker, L. *Catal. Today* **2017**, *279*, 29–35.

(248) Carrus, M.; Fantauzzi, M.; Riboni, F.; Makosch, M.; Rossi, A.; Selli, E.; Van Bokhoven, J. A. *Appl. Catal. A Gen.* **2016**, *519*, 130–138.

(249) Strachan, J.; Barnett, C.; Masters, A. F.; Maschmeyer, T. *ACS Catal.* **2020**, *10* (10), 5516–5521.

(250) Schlesinger, H. I.; Brown, H. C.; Finholt, A. E.; Gilbreath, J. R.; Hoekstra, H. R.; Hyde, E. K. *J. Am. Chem. Soc.* **1953**, *75* (1), 215–219.

(251) Liu, B. H.; Li, Z. P. *J. Power Sources* **2009**, *187* (2), 527–534.

(252) Ortiz-Quiñ Onez, J.-L.; Pal, U. **2019**.

(253) Liu, S.; Qileng, A.; Huang, J.; Gao, Q.; Liu, Y. *RSC Adv.* **2017**, *7* (72), 45545–45551.

(254) Suchomel, P.; Kvitek, L.; Prucek, R.; Panacek, A.; Halder, A.; Vajda, S.; Zboril, R. *Sci. Rep.* **2018**, *8* (1), 4589.

(255) Deraedt, C.; Salmon, L.; Gatard, S.; Ciganda, R.; Hernandez, R.; Ruiz, J.; Astruc, D. *Chem. Commun.* **2014**, *50* (91), 14194–14196.

(256) Grzeschik, R.; Schäfer, D.; Holtum, T.; Küpper, S.; Hoffmann, A.; Schlücker, S. *J. Phys. Chem. C* **2020**, *124* (5), 22.

(257) Suchomel, P.; Kvitek, L.; Prucek, R.; Panacek, A.; Halder, A.; Vajda, S.; Zboril, R. *Sci. Rep.* **2018**, *8* (1), 4589.

(258) Wunder, S.; Lu, Y.; Albrecht, M.; Ballauff, M. *ACS Catal* **2011**, *1*, 908–916.

(259) Neal, R. D.; Hughes, R. A.; Sapkota, P.; Ptasinska, S.; Neretina, S. *ACS Catal.* **2020**, *10* (17), 10040–10050.

(260) Karuppusamy, S.; Marken, F.; Kulandainathan, M. A. *New J. Chem.* **2020**, *44* (41), 17780–17790.

(261) Menumerov, E.; Hughes, R. A.; Neretina, S. *Nano Lett.* **2016**, *16* (12), 7791–7797.

(262) Wu, K.-L.; Wei, X.-W.; Zhou, X.-M.; Wu, D.-H.; Liu, X.-W.; Ye, Y.; Wang, Q. *J. Phys. Chem. C* **2011**, *115*, 16268–16274.

(263) Barai, P.; Feng, Z.; Kondo, H.; Srinivasan, V. *J. Phys. Chem. B* **2019**, *123* (15), 3291–3303.

(264) Zhang, Y.; Pluchery, O.; Caillard, L.; Lamic-Humblot, A. F.; Casale, S.; Chabal, Y. J.; Salmeron, M. *Nano Lett.* **2015**, *15* (1), 51–55.

(265) Waters, C. K.; Cojocaru, B.; Lin, F.; Woodard, L.; Richards, R. M.; Parvulescu, V. In *RSC Catalysis Series*; 2019; Vol. 2019-Janua, pp 309–328.

(266) Rougier, A.; Delmas, C.; Chadwick, A. V. *Solid State Commun.* **1995**, *94* (2), 123–127.

(267) Radin, M. D.; Van Der Ven, A. *Chem. Mater.* **2018**, *30* (3), 607–618.

(268) Faenza, N. V; Pereira, N.; Halat, D. M.; Vinckeviciute, J.; Bruce, L.; Radin, M. D.; Mukherjee, P.; Badway, F.; Halajko, A.; Cosandey, F.; Grey, C. P.; Van Der Ven, A.; Amatucci, G. G. *Chem. Mater.* **2018**, *30* (21), 7545–7574.

(269) Mehdi, B.; Xu, C.; Märker, K.; Lee, J.; Mahadevegowda, A.; Reeves, P.; Day, S.; Groh, M.; Emge, S.; Ducati, C.; Tang, C.; Grey, C. *Nat. Mater.* **2020**, No. 1.

(270) Park, M. S.; Park, I.; Kang, Y.-S.; Im, D.; Doo, S.-G. *Phys. Chem. Chem. Phys* **2016**, *18*, 26807.

(271) Onuki, M.; Kinoshita, S.; Sakata, Y.; Yanagidate, M.; Otake, Y.; Ue, M.; Deguchi, M. *J. Electrochem. Soc.* **2008**, *155* (11), A794.

(272) Leifer, N.; Sanchez, L. M.; Grey, C. P.; Greenbaum, S. G. *Artic. J. Electrochem. Soc.* **2011**.

(273) Tasaki*, K. *J. Phys. Chem. B* **2005**, *109* (7), 2920–2933.

(274) Lu, P.; Harris, S. J. *Electrochem. commun.* **2011**, *13* (10), 1035–1037.

(275) Mccloskey, B. D.; Bethune, D. S.; Shelby, R. M.; Girishkumar, G.; Luntz, A. C. *J. Phys. Chem. Lett* **2011**, *2*, 1161–1166.

(276) Gilbert, J. A.; Shkrob, I. A.; Abraham, D. P. *J. Electrochem. Soc.* **2017**, *164* (2), A389–A399.

(277) Thompson, L. M.; Stone, W.; Eldesoky, A.; Smith, N. K.; McFarlane, C. R. M.; Kim, J. S.; Johnson, M. B.; Petibon, R.; Dahn, J. R. *J. Electrochem. Soc.* **2018**, *165* (11), A2732–A2740.

(278) NREL. Battery Second Use for Plug-In Electric Vehicles | Transportation Research https://www.nrel.gov/transportation/battery-second-use.html (accessed Aug 15, 2021).

(279) Lewis, G. N.; Keyes, F. G. *J. Am. Chem. Soc.* **1913**, *35* (4), 340–344.

(280) Rao, K. S.; Mandal, B. P.; Achary, S. N.; Tyagi, A. K. .

(281) Lin, D.; Liu, Y.; Cui, Y. *Nat. Nanotechnol.* | **2017**, *12*.

(282) Yoon, W. S.; Kim, K. B.; Kim, M. G.; Lee, M. K.; Shin, H. J.; Lee, J. M.; Lee, J. S.; Yo, C. H. *J. Phys. Chem. B* **2002**, *106* (10), 2526–2532.

(283) Rosolen, J. M.; Abbate, M. *Solid State Ionics* **2001**, *139* (1–2), 83–88.

(284) Montoro, L. A.; Abbate, M.; Rosolen, J. M. *J. Electrochem. Soc.* **2000**, *147* (5), 1651–1657.

(285) Hu, E.; Yu, X.; Lin, R.; Bi, X.; Lu, J.; Bak, S.; Nam, K.-W.; Xin, H. L.; Jaye, C.; Fischer, D. A.; Amine, K.; Yang, X.-Q. *Nat. Energy* **2018**, *3* (8), 690–698.

(286) Xiao, P.; Deng, Z. Q.; Manthiram, A.; Henkelman, G. *J. Phys. Chem. C* **2012**, *116*, 23201–23204.

(287) Leifer, N.; Penki, T.; Nanda, R.; Grinblat, J.; Luski, S.; Aurbach, D.; Goobes, G. *Phys. Chem. Chem. Phys.* **2020**, *22* (16), 9098–9109.

(288) Rahman, M. M.; Lin, F. *Matter* **2021**, *4* (2), 490–527.

(289) Deng, Z. Q.; Manthiram, A. *J. Phys. Chem. C* **2011**, *115* (14), 7097–7103.

(290) Ohzuku, T.; Makimura, Y. *Chem. Lett.* **2001**, No. 7, 642–643.

(291) Yabuuchi, N.; Ohzuku, T. In *Journal of Power Sources*; 2003; Vol. 119–121, pp 171–174.

(292) Whittingham, M. S. *Chem. Rev.* **2004**, *104* (10), 4271–4301.

(293) Thackeray, M. M.; Johnson, P. J.; de Picciotto, L. A.; Bruce, P. G.; Goodenough, J. B. *Mater. Res. Bull.* **1984**, *19* (2), 179–187.

(294) Lu, Z.; MacNeil, D. D.; Dahn, J. R. *Electrochem. Solid-State Lett.* **2001**, *4* (12).

(295) Lee, J.; Kitchaev, D. A.; Kwon, D. H.; Lee, C. W.; Papp, J. K.; Liu, Y. S.; Lun, Z.; Clément, R. J.; Shi, T.; McCloskey, B. D.; Guo, J.; Balasubramanian, M.; Ceder, G. *Nature* **2018**, *556* (7700), 185–190.

(296) Kitchaev, D. A.; Lun, Z.; Richards, W. D.; Ji, H.; Clément, R. J.; Balasubramanian, M.; Kwon, D. H.; Dai, K.; Papp, J. K.; Lei, T.; McCloskey, B. D.; Yang, W.; Lee, J.; Ceder, G. *Energy Environ. Sci.* **2018**, *11* (8), 2159–2171.

(297) Strehle, B.; Kleiner, K.; Jung, R.; Chesneau, F.; Mendez, M.; Gasteiger, H. A.; Piana, M. *J. Electrochem. Soc.* **2017**.

(298) Sigel, F.; Schwarz, rn; Kleiner, K.; Dra, C.; Esmezjan, L.; Yavuz, M.; Indris, S.; Ehrenberg, H. *Cite This Chem. Mater* **2020**, *32*, 1210–1223.

(299) Jarvis, K. A.; Deng, Z.; Allard, L. F.; Manthiram, A.; Ferreira, P. J. *Chem. Mater* **2011**, *23*, 3614–3621.

(300) Urban, A.; Abdellahi, A.; Dacek, S.; Artrith, N.; Ceder, G. *Phys. Rev. Lett.* **2017**, *119* (17), 176402.

(301) Koga, H.; Croguennec, L.; Ménétrier, M.; Mannessiez, P.; Weill, F.; Delmas, C. *J. Power Sources* **2013**, *236* (January 2019), 250–258.

(302) Seo, D. H.; Lee, J.; Urban, A.; Malik, R.; Kang, S.; Ceder, G. *Nat. Chem.* **2016**, *8* (7), 692–697.

(303) Kalyani, P.; Chitra, S.; Mohan, T.; Gopukumar, S. *J. Power Sources* **1999**, *80* (1–2), 103–106.

(304) Armstrong, A. R.; Holzapfel, M.; Novk, P.; Christopher, S.; Kang, S.-H.; Thackeray, M.

M.; Bruce, P. G.; Ni, L.; Mn, L.; Nova, P.; Johnson, C. S. *JACS* **2006**, No. 11, 8694–8698.

(305) Glazier, S. L.; Li, J.; Zhou, J.; Bond, T.; Dahn, J. R. *Chem. Mater.* **2015**, *27* (22), 7751–7756.

(306) Diaz-Lopez, M.; Chater, P. A.; Joly, Y.; Proux, O.; Hazemann, J.-L.; Bordet, P.; Pralong, V. *J. Mater. Chem. A* **2020**.

(307) Wang, R.; Li, X.; Liu, L.; Lee, J.; Seo, D.-H.; Bo, S.-H.; Urban, A.; Ceder, G. *Electrochem. commun.* **2015**, *60*, 70–73.

(308) Perez, A. J.; Jacquet, Q.; Batuk, D.; Iadecola, A.; Saubanère, M.; Rousse, G.; Larcher, D.; Vezin, H.; Doublet, M.-L.; Tarascon, J.-M. *Nat. Energy* **2017**.

(309) Xie, Y.; Saubanère, M.; Doublet, M. L. *Energy Environ. Sci.* **2017**, *10* (1), 266–274.

(310) House, R.; Jin, L.; Maitra, U.; Tsuruta, K.; Somerville, J.; Forstermann, D.; Massel, F.; Duda, L.; Roberts, M. R.; Bruce, P. G. *J. Name Artic. This J. is J. Name* **2013**, *00*, 1–3.

(311) Richards, W. D.; Dacek, S. T.; Kitchaev, D. A.; Ceder, G. *Adv. Energy Mater.* **2018**, *8* (5).

(312) Renfrew, S. E.; McCloskey, B. D. *J. Am. Chem. Soc.* **2017**, *139* (49), 17853–17860.

(313) Teufl, T.; Strehle, B.; Müller, P.; Gasteiger, H. A.; Mendez, M. A. *J. Electrochem. Soc.* **2018**, *165* (11), A2718–A2731.

(314) Jung, R.; Metzger, M.; Maglia, F.; Stinner, C.; Gasteiger, H. A. *J. Phys. Chem. Lett.* **2017**, *8* (19), 4820–4825.

(315) Gaines, L. *Sustain. Mater. Technol.* **2018**, *17*.

(316) Wu, Z.; Soh, T.; Chan, J.; Meng, S.; Meyer, D.; Srinivasan, M.; Tay, Y. *Environ. Sci. Technol* **2021**, *54*, 36.

(317) Harper, G.; Sommerville, R.; Kendrick, E.; Driscoll, L.; Slater, P.; Stolkin, R.; Walton, A.; Christensen, P.; Heidrich, O.; Lambert, S.; Abbott, A.; Ryder, K.; Gaines, L.; Anderson, P. *Nature* **2019**, *575*, 75.

(318) Slater, M. D.; Kim, D.; Lee, E.; Johnson, C. S. *Adv. Funct. Mater.* **2013**, *23* (8), 947–958.

(319) He, K.; Lin, F.; Zhu, Y.; Yu, X.; Li, J.; Lin, R.; Nordlund, D.; Weng, T.-C.; Richards, R. M.; Yang, X.-Q.; Doeff, M. M.; Stach, E. A.; Mo, Y.; Xin, H. L.; Su, D. *Nano Lett.* **2015**, *15* (9), 5755–5763.

(320) Mu, L.; Feng, X.; Kou, R.; Zhang, Y.; Guo, H.; Tian, C.; Sun, C.-J.; Du, X.-W.; Nordlund, D.; Xin, H. L.; Lin, F. *Adv. Energy Mater.* **2018**, 1801975.

(321) Asif, M.; Kilian, S.; Rashad, M. *Energy Storage Mater.* **2021**, *42*, 129–144.

(322) Aurbach, D.; Gofer, Y.; Lu, Z.; Schechter, A.; Chusid, O.; Gizbar, H.; Cohen, Y.; Ashkenazi, V.; Moshkovich, M.; Turgeman, R.; Levi, E. In *Journal of Power Sources*; 2001; Vol. 97–98, pp 28–32.

(323) Massé, R. C.; Uchaker, E.; Cao, G. *Sci. China Mater. 2015 589* **2015**, *58* (9), 715–766.

(324) Rahman, M. M.; Mao, J.; Kan, W. H.; Sun, C.-J.; Li, L.; Zhang, Y.; Avdeev, M.; Du, X.-W.; Lin, F. *ACS Mater. Lett.* **2019**, *1* (5), 573–581.